AD-A216 111

An Investigation of Long Term Orbits
About the Planet Mars Using a Dynamic
Atmosphere Model

THESIS

Zoltan L. Farago, B.S., B.S.A.E.
Captain, USAF

AFIT/GA/ENY/89D-01

DEPARTMENT OF THE AIR FORCE

AIR UNIVERSITY

AIR FORCE INSTITUTE OF TECHNOLOGY

Wright-Patterson Air Force Base, Ohio

89 12 29 043

AFIT/GA/ENY/89D-01

An Investigation of Long Term Orbits
About the Planet Mars Using a Dynamic
Atmosphere Model

THESIS

Zoltan L. Farago, B.S., B.S.A.E.
Captain, USAF

AFIT/GA/ENY/89D-01

Preface

The purpose of this study was to examine the effects of atmospheric drag on the long term orbit of artificial satellites about the planet Mars using a dynamic atmosphere model in place of a static atmosphere model.

Existing literature on the Martian atmosphere and orbital equation models were examined and then incorporated into theoretical and computational models. However, the resulting models are only the starting point for the development of more sophistocated theoretical and computational models. This thesis establishes the fundamental differences, if any, in satellite motion due to the use of a dynamic atmosphere model instead of a static atmosphere model.

I am indebted to my thesis advisor, Capt Rodney Bain, for his suggestions and ready assistance. He has increased my understanding of both the mathematical and orbital theory, as well as providing a 'relief valve' for all the frustrations associated with the completion of this thesis. I would especially like to thank Richard P. Osedacz for his help and moral support.

Zoltan L. Farago

ii

Table of Contents

List of Figures

List of Tables

Notation

Roman:

A	Satellite cross-sectional area
a	Semi-major axis
a	mean solar distance
a	function of temperature
a_e	semi-major axis of Earth
a_p	semi-major axis of Mars
C_d	atmospheric drag coefficient
D	atmospheric drag
e	eccentricity
F_{lmp}	inclination function
$F_{10.7}$	solar radiation intensity
f	true anomaly
f_0	mixing ratio for monatomic oxygen
g	gravity
G_{lpq}	eccentricity function
H	scale height for density calculation
h	satellite altitude
h	Modified or equinoctial set orbital element
h_0	reference altitude for density calculation
h_p	periapsis altitude
i	inclination
k	Modified or equinoctial set orbital element
k	universal gas constant
L_s	areocentric solar longitude

L_1	function of areocentric solar longitude
L_2	function of areocentric solar longitude
M	mean anomaly
m	mass of satellite
m	mean molecular weight
n	mean motion
P	prime integer
P	atmospheric pressure
P_0	maximum amplitude of atmospheric pressure
PI	3.141592654...
Q	prime integer
R',R^*,R	perturbation
R	current solar distance
R_p	Mars' radius plus atmospheric blockage
$R_{6.1}$	correction to reference 6.1 mbar ellipsoid
r	radius vector of satellite relative to Mars
r_s	radius vector of sun relative to Mars
r_{sun}	distance of sun at 1 A.U.
S	angle between sun and satellite
SCLAT	areocentric latitude of spacecraft
SCLONG	areocentric longitude of spacecraft
SNLAT	areocentric latitude of sun
SNLONG	areocentric longitude of sun
S_0	ratio of P/Q
S_1,S_2,S_3	Mars centered coordinate system
T	atmospheric temperature

T'	dT/dz
TIME	time function for diurnal effect
T_{lmt}	coefficient of Associated Legendre Polynomial
t	time
T_∞	Exosphere temperature
V	gravitational potential energy
v	satellite velocity
x	geopotential altitude
z	altitude
Δz_{DS}	dust storm correction to turbopause altitude
z_f	turbopause altitude
Δz_f	seasonal correction to turbopause altitude
Δz_{SN}	seasonal and diurnal correction

Greek:

α	right ascension
β	inverse of scale height
β'	function of eccentricity
ϵ_S	amplitude of seasonal variation
ϵ_D	amplitude of diurnal variation
τ	black body radiation constant
δ	declination
θ	latitude
θ_g	prime meridian
ϱ	longitude

xi

L_N stroboscopic mean node

μ gravitational parameter

μ atmospheric density

μ_0 reference atmospheric density

Ω longitude of the ascending node

ω argument of periapsis

Miscellaneous:

ϕ function of density variables

∇ gradient

Abstract

This study examines the effects of atmospheric drag on
the long term orbital motion of an artificial satellite
about the planet Mars using a dynamic Martian atmosphere
model instead of a static atmosphere model.

Present studies of motion through the Martian
atmosphere use a non-rotating (static) atmosphere model
which has a simple exponential drop-off with altitude.
However, Mars, like other planets, is known to have a
turbulent, complex atmosphere. As a result, a new dynamic
model of the Martian atmosphere uses data from recent space
probes of Mars to simulate an atmosphere that is both
position dependent, through latitude and longitude effects,
and time dependent, through a variety of effects. These
include diurnal and seasonal effects, annual motion effects,
solar activity effects, and dust storm effects. Nine
constituent gases are included in the above model. The
model determines atmospheric mass density for the
calculation of atmospheric drag. The existing static model
is also used to calculate atmospheric drag to provide a
comparison in conjunction with other effects.

In addition to atmospheric drag, perturbations due to the attraction of the sun, the aspherical gravity field of Mars, and the effects of the solar wind are also modeled.

The resulting orbital data are then compared to determine the differences between the two models, thus showing the effects on long term motion of using a dynamic model of the Martian atmosphere.

.

AN INVESTIGATION OF LONG TERM ORBITS

ABOUT THE PLANET MARS USING A DYNAMIC

ATMOSPHERE MODEL

I. Introduction

Current studies of orbital motion about Mars use a simple non-rotating (static) exponential model for the Martian atmosphere. However, the Martian atmosphere is far from static; the entire surface of Mars has been obscured by dust storms (37:206). Recent data indicate the mass density of the Martian atmosphere is heavily time and position dependent (dynamic) due to a variety of perturbing effects. As a result, no accurate prediction of atmospheric mass density at a particular position and time in the future is possible (8:1). However, using a time and position dependent model of the atmosphere over a sufficiently long time, mass density can be predicted with acceptable accuracy since long time intervals average out short term fluctuations that cannot be modeled (9:1).

Current literature on the Martian atmosphere is examined and then a model for satellite motion through a

"realistic" dynamic Martian atmosphere is formulated. To assess the effect of using a dynamic atmosphere model, the resulting orbital data from the more realistic dynamic atmosphere model was compared to the orbital data from the current static atmosphere model. Two advantages of using a more realistic model would be a better guaranteed lifetime for the satellite, required for various NASA guidelines (9:1), and a more effective use of the limited spacecraft mass and internal space in the tradeoff between fuel and scientific payloads.

The trajectory propagation model includes perturbation models for the aspherical Martian gravity field, the gravitational attraction of the sun, solar radiation pressure, and atmospheric drag at altitudes below 1000 km.

II. The Martian Atmosphere

In order to develop the dynamic atmosphere model, literature on the Martian atmosphere was surveyed and then used to formulate the model. This section briefly reviews the literature.

Similarities of Mars to Earth

The key to understanding the development of models of the Martian atmosphere is to examine the similarities of Mars to Earth and the limitations of viewing Mars through the Earth's atmosphere. Table 1.1 presents Earth and Mars information.

Several similarities exist: 1) the rotation rates are nearly the same, 2) both have seasons although planetary tilt causes longer seasons on Mars, and 3) both planets have polar caps and clouds. On the other hand, 1) Mars receives less radiation from the Sun since it is farther away, 2) it has no oceans, 3) its atmosphere is only about 0.01 that of Earth, and 4) its polar caps are not made from water.

Table 1.1: Earth and Mars Data		
Planet:	Earth	Mars
Mean Distance from sun:	1.496E8 km	227,941,963 km
Eccentricity:	0.017	0.093387
Inclination to ecliptic:	0°	1.86641'
Sidereal Period:	365.256 days	686.9804 days
Equatorial Radius:	6378.2 km	3396.9 km
Polar Radius:	6356.2 km	3376.1 km
Mean Surface Gravity:	978 cm/s^2	372 cm/s^2
Mean Escape Velocity:	11.2 km/s	5.022 km/s
Sidereal Day:	23 h 56 m 4 s	24 h 37 m 22.663 s
Inclination of Equator to Orbit:23.5°		24.936°
Visual Albedo:	0.36	0.159
	(Various Sources)	(Various Sources)

Furthermore, due to the orientation and eccentricity of the orbit, the Martian seasons are not the same length. The southern summer is short and hot, while the northern summer is long and cool, thus strongly affecting the polar caps and the atmosphere.

Brief History of Observations/Theories

A wide variety of seasonal and meteorological data have been observed since Sir William Herschel first noted Mars' thin atmosphere . Until recently, most observations of Mars

were taken from the surface of the Earth (21). However, Earth's atmosphere affects the data. Similar molecules contaminate data, resolution is limited, and signal strength is weakened. Although various means have been used to reduce the amount of atmosphere the signal travels through, these also affected the data, leaving one solution: space probes. A stronger signal and no filtering atmosphere mean the space probes receive data too weak to reach Earth, such as ultraviolet, and have greater resolution and accuracy. They overturned many theories.

Early theories on the Martian atmosphere reveal some good deductions and some bad assumptions. For example, predictions of large diurnal temperature fluctuations were correct . However, the use of terrestrial assumptions and atmosphere-filtered data led to errors. For example, the atmosphere, thought to be mainly N_2 as on Earth, is actually composed almost entirely of CO_2 (5:148). Also, the mean surface pressure, which polarimetric data indicated to be about 85 mbars (21:23), is now accepted as about 6 mbars (15:4321). Further differences will be mentioned in later sections.

Most Recent Information/Beliefs about the Martian Atmosphere

Major seasonal changes occur and are closely associated with changes in the polar caps. In early spring the

5

southern polar cap has its greatest size. As spring proceeds, the cap sublimates and begins to recede at about 1 of latitude every five days. One-third of the Martian year later the cap has receded to its smallest extent, leaving small remnant ice caps behind (22:4249). The behavior of the northern cap is similar, but not all the details are the same due to the difference in season length and variation in distance from the sun; the planet is at a greater distance from the sun during the northern summer and so receives less heat. Both caps advance and retreat by about 35 latitude each season. Mariners 7 and 9 infrared radiometer and spectrometer measurements showed that the main polar caps are CO_2 (3:404). Viking 2 showed the north polar remnant to be water ice, probably the largest collection of water on the planet. The south polar remnant composition is still in some doubt. The polar caps affect atmospheric density by causing the carbon dioxide to "snow out" of the atmosphere or to sublime, causing a seasonal variation of about 25-30% (42:3969). At the cap edge there exist strong winds driven by mass outflow and large temperature gradients during sublimation as well as traveling waves (weather systems) generated equatorward (49:298). As a result, changes in polar temperature have profound effects on atmospheric dynamics (5:124). Dust storms affect the polar caps by filtering the sunlight and

by contributing dust particles to the polar deposits, lowering their albedo (38:270).

Dust is always being injected into the Martian atmosphere (38:259). However, it is greatest at times close to orbital perihelion and summer solstice in the southern hemisphere. There are about 100 local dust storms each year, mostly during the southern hemisphere spring (38:262). Once or twice a year these develop into global dust storms, usually starting in certain preferred locations. These storms are never quite the same, so a long term average must be used to quantify their effects (49:294). Viking showed that measured amplitudes of thermally driven, planetary-scale atmospheric tides were closely coupled to the dust content of the atmosphere, especially during great storms (49:293). The Mariner 9 IRIS (infrared spectroscopy) experiment showed the dust is about 60±10% SiO_2 (18:430). Mariner 9 pictures also showed dust thrown into the atmosphere as high as 40-60 km (49:302). Dust storms tend to reduce vertical temperature gradients but increase horizontal temperature gradients (17:334), to warm the upper atmosphere since solar radiation is absorbed by dust suspended in the atmosphere, to increase the depth and intensity of circulation (17:335), to affect the polar ice deposit albedo, and to vary temperature dependence on latitude (32:411). The following figure taken from (18:434) shows some of these effects:
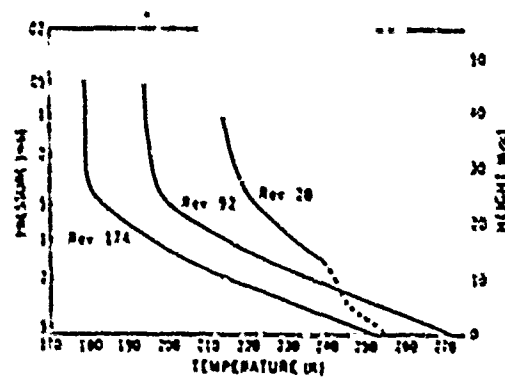
Temperature profiles obtained by inversion of measurements in the 667-cm⁻¹ CO₂ absorption band. The profiles were obtained at approximately -30° latitude and 1400hr Martian local time during the revolutions indicated. During revolution 20 the atmosphere was heavily dust laden. By revolution 92 the dust was dissipating; clearing was well advanced by revolution 174.

Figure 1.1: The Effect of Dust Storms on Atmospheric
Temperature and Pressure

During dust storms, temperature distribution is roughly constant (29:389). Furthermore, during the decay phase, the atmosphere is more isothermal and thus more stable (49:302).

The lack of oceans also affects the atmosphere in ways not originally foreseen. The absence of seasonal heat storage by oceans makes seasonal temperature change very large. Furthermore, outgoing infrared radiation is not constant with latitude but decreases from equator to poles. Finally, atmospheric wave character is changed, resulting in varying circulation regimes (21:130).

The atmosphere is very thin. Average surface pressure is less than 0.01 that of earth. However, because of large variations in surface topography altitude, some locations

8

have almost five times the surface pressure of others. This fact plus meteorological processes make the surface pressure highly variable. The total mass of the atmosphere, unlike Earth's, undergoes major seasonal variations of as much as 25-30% as CO_2 "snows out" at the winter pole and is released from the receding summer polar cap. Yet, in spite of its thinness, the atmosphere still supports three different kinds of clouds as well as dust storms (22:4280). Furthermore, the presence of dust plays an important role in establishing atmosphere structure.

The Martian atmosphere is usually divided into two layers, a lower neutral layer and an ionosphere (21:228). The lower atmosphere consists mainly of carbon dioxide. The characteristic temperature is about 200 K (21:28), which is generally colder than the average surface temperature which is about 250 K in the daytime (21:25). This difference is due to the presence of temperature gradients which have an average value of about 1.6 K per vertical kilometer (39:4363). Higher up in the atmosphere, large daily waves of temperature and density have been found, indicating a confused and variable structure (39:4364). Below 125 km in altitude, where the atmosphere is well mixed by turbulence, Viking mass spectrometers have discovered that 96.5% of the atmosphere by weight is CO_2 (34:4341). The composition of the lower Martian atmosphere is as follows (37:4637):

9

Table 1.2: Composition of the Martian Atmosphere	
(fraction by weight)	
Carbon Dioxide (CO_2):	96.5%
Molecular Nitrogen (N_2):	1.8%
Argon (Ar):	1.5%
Molecular Oxygen (O_2):	0.1%
Carbon Monoxide (CO):[*]	0.05%
Water Vapor (H_2O):[*]	0.02%
Neon (Ne):	0.0001%
Krypton (Kr):	0.00003%
Xenon (Xe):	0.00002%
[*] Uncertain, variable, or unevenly distributed.	

Trace amounts of other gases also appear due to photochemical reactions. The lower atmosphere supports the ionosphere.

The topmost layer, or ionosphere, is that part of the atmosphere where constituent densities are low enough for the components to separate diffusively according to mass. Unlike the Earth's ionosphere, its peak density of about 10^5 ions/cm^3 occurs near 130 km and is formed primarily of O_2^+ ions (approximately 90% O_2^+ and 10% CO_2^+) that have been produced in local chemical reactions (19:4351). Another important constituent of the outer limits of the atmosphere is atomic hydrogen, H, which is detectable over 10,000 km

above the surface (37:210). The following figures taken
from (4:161) provide data on the ionosphere:
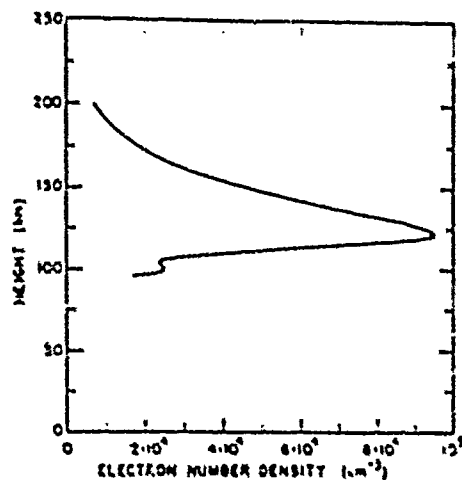
Figure 1.2: Ionosphere Density as a Function of Altitude
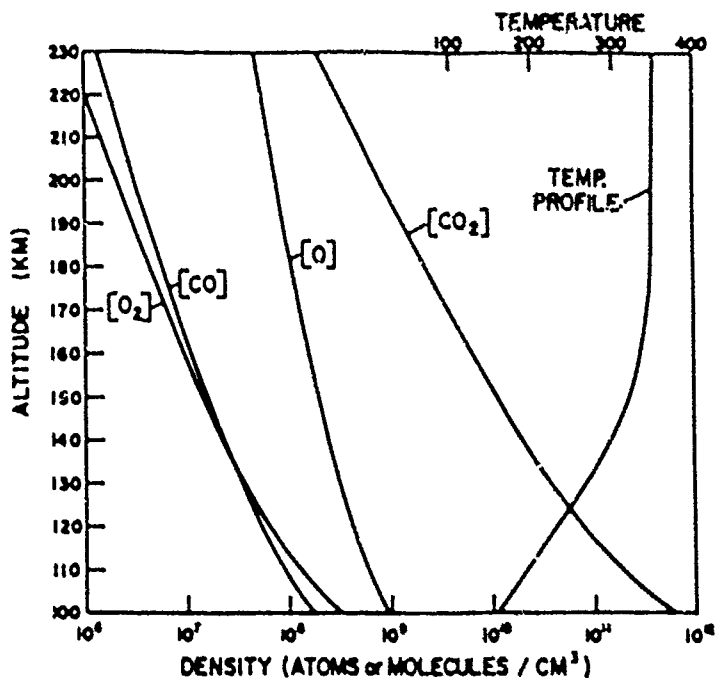
Mars model atmosphere. This model atmosphere is based on Mariner 6 and 7 ultraviolet
spectrometer and radio occultation results as well as ground-based telescope observations.

Figure 1.3: Ionosphere Constituent Density as a
Function of Altitude

11

Water is a minor constituent of the atmosphere due to low atmospheric pressure and low surface temperatures. Nevertheless, it seems to play an important role in atmospheric chemistry and meteorology. The atmosphere is effectively saturated with water vapor, yet water exists only in vapor or solid form. Viking also found water vapor is uniformly mixed up to altitudes of 10-15 km and shows strong latitudinal gradients that depend on season and location (13:4225). A strong diurnal variation was also detected (13:4242). The total amount of free water in the atmosphere is estimated to be equivalent to 1.3 km^3 of ice (13:4246).

The vertical structure of the Martian atmosphere, i.e. the relation of pressure and temperature to altitude, is determined by a complicated interplay among several processes: radiative, convective (natural and forced), and advective energy transport and the way energy from the sun is at first absorbed into the atmosphere and then lost by radiation into space (5:161). Because of the wide range of density in the atmosphere, different processes are dominant at different height ranges. Before 1965, essentially all knowledge of atmospheric structure was based on extrapolations of indirect data with the help of theoretical models (21:25). As mentioned previously, many of these models made assumptions that proved to be incorrect and so invalidated the extrapolated data. Space probe data has

given us the first real knowledge of the structure of the Martian atmosphere.

Two factors control the vertical structure of the lower atmosphere: its composition of almost pure carbon dioxide and its content of large quantities of suspended dust. Carbon dioxide, which has a strong infrared spectrum, radiates energy with great efficiency at Martian temperatures and causes the atmosphere to respond rapidly to changes in the amount of solar radiation received. The suspended dust is a strong absorber of heat directly from the Sun's radiation and provides a distibuted energy source throughout the lower atmosphere (29:386).

Surface temperatures depend on latitude, season, and time of day (39:4364). (See Fig. 1.4 Soviet Mars 3 photometer data (32:411)). Viking 1 observed a wide temperature fluctuation from day to night. The usual temperature variation was from about 150 K just before sunrise to a high of 240 K in the early afternoon (42:3969). This diurnal variation is greatest near the ground and occurs because of the surface's ability to radiate its heat to space quickly during the night. During dust storms, this ability is impaired and the daily temperature swing is reduced (26:484). The effect of dust storms on pressure and temperature is shown in the Mariner 9 infrared spectroscopy data of Fig. 1.5 (18:434).

13

λ
52° 41° 34° 29° 26° 24° 22° 0° 19° 18° 18° 18° 19° 21° 27° 48°

φ
43° -37° -21° -25° -18° -12° -6° 0° 6° 12° 19° 26° 33° 42° 52° 63°

MARS 3
Feb. 28, 1972

Mare
Erythraeum

Margaritifer
Sinus

A=0.25   A=0.15

(κρc)^{1/2} = 0.006

Mare
Acidalium
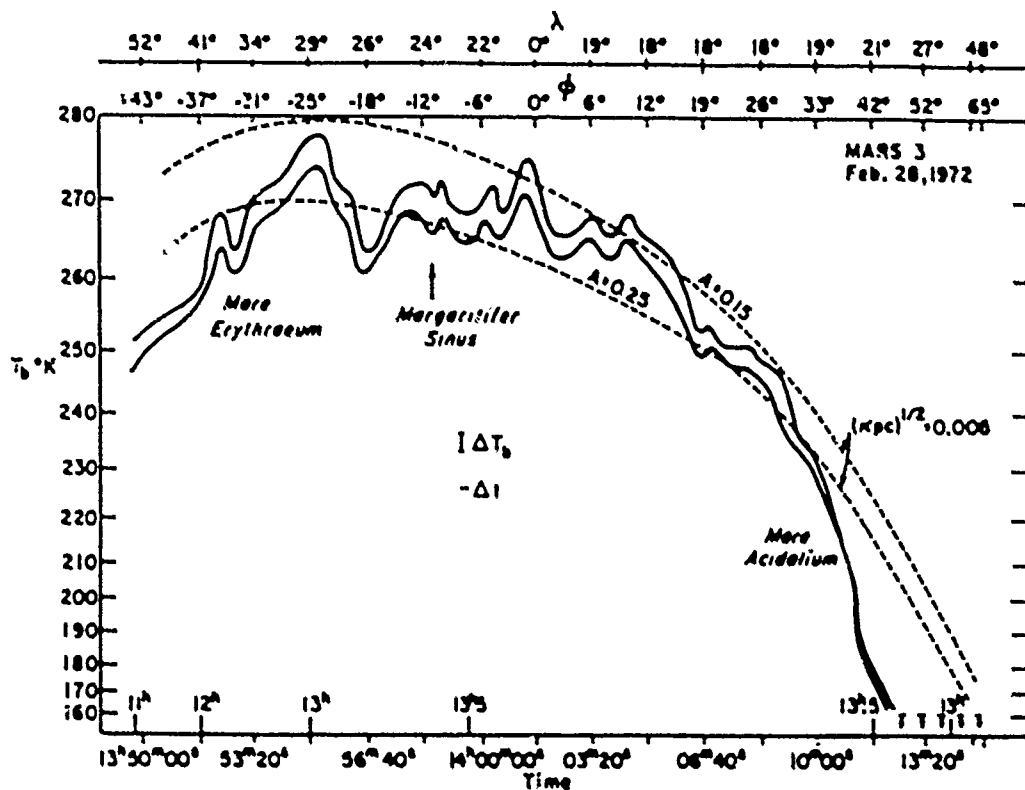
Brightness temperature according to measurements on Feb. 28, 1972.

Figure 1.4: Atmospheric Temperature as a Function
of Time and Latitude

Mariner 9 infrared spectroscopy data also showed large
diurnal variations (15-30 K) in atmospheric temperature up
to about 30 km and winds with a strong tidal component
(18:423).   However, other oscillations appear throughout
the atmosphere as a result of the direct input of energy
from the Sun.   These oscillations, which are wavelike in
nature and are akin to tides, have been measured as pressure
and temperature variations and lead to a very complex wave-

14

like rather than smooth, vertical structure (39:4375). The mean temperature in the lower atmosphere falls off with altitude at a lapse rate of about 1.4 K per vertical kilometer to a height of about 40 km and is roughly constant at 140 K above that level. This low lapse rate was unexpected and is due to the large amount of suspended dust.
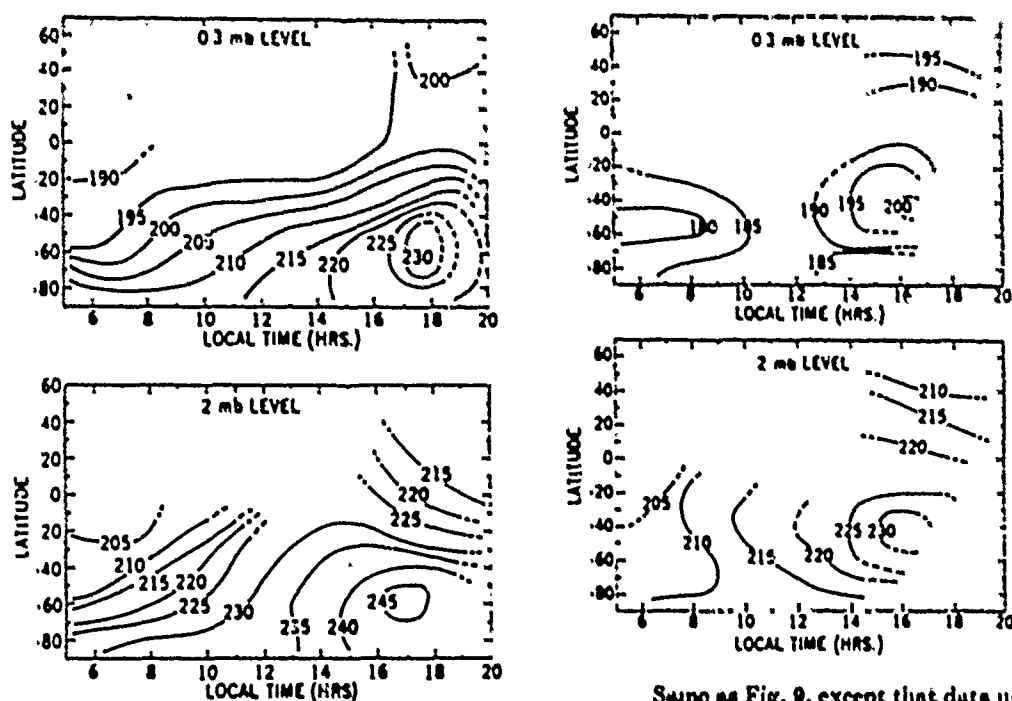
Dependence on latitude and Martian local time of atmospheric temperatures at the 2-mbar level (~10km) and at the 0.3-mbar level (~30km). The temperatures represent averages over data obtained on revolutions 1-85 during the dust storm.

Same as Fig. 9, except that data used were obtained as the atmospheric dust was dissipating on revolutions 85-120.

Figure 1.5: Atmospheric Temperature as a Function of Time, Latitude, and Dust Storm

Mariner 9 radio occultation data provided sample temperature gradients (26:504):

15

Average temperature gradients, odd revolutions.
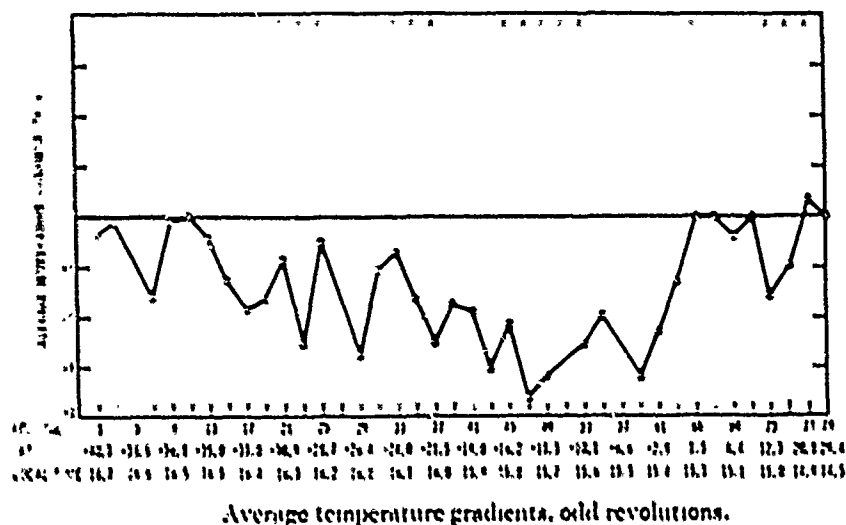
Figure 1.6: Average Atmospheric Temperature Gradients

Above about 100 km, the structure of the atmosphere is determined by the onset of diffusive separation of the various atmospheric molecules. The tendency of heavier molecules to lie below the lighter overcomes the tendency of turbulence to mix the atmospheric gases. Absorption of ultraviolet light from the sun then dissociates and ionizes the constituents and leads to complex sequences of chemical reactions (5:27). The net result is the embedding of an ionized layer near' 130 km and an increase in temperature, particularly of the ionic component, at higher altitudes (19:4351). The top of the atmosphere, or exosphere, is characterized by a temperature of about 325 K averaged over the Martian year (44:469). A good summary of the ion reactions is provided in the following tables (5:255 and 5:275):

16

Table 1.3: Some Ionosphere Reactions

SOME IMPORTANT CHARGE REARRANGEMENT REACTIONS

(1) $O^- + CO_2 \rightarrow CO + O_2^- + 1\cdot22$ eV
(2) $O^- + O_2 \rightarrow O + O_2^- + 1\cdot54$ eV
(3) $O^- + N_2 \rightarrow NO^+ + N + 1\cdot12$ eV
(4) $N_2^+ + CO_2 \rightarrow N_2 + CO_2^+ + 1\cdot79$ eV
(5) $N_2^+ + O_2 \rightarrow N_2 + O_2 + 3\cdot50$ eV
(6) $N_2^+ + O \rightarrow NO^+ + N + 3\cdot08$ eV
(7) $CO^+ + CO_2 \rightarrow CO + CO_2^+ + 0\cdot22$ eV
(8) $CO^+ + O_2 \rightarrow CO + O_2^+ + 1\cdot93$ eV
(9) $CO_2^+ + O_2 \rightarrow CO_2 + O_2^+ + 1\cdot71$ eV
(10) $A^- + CO_2 \rightarrow A + CO_2^- + 1\cdot97$ eV
(11) $A^- + CO \rightarrow A + CO^- + 1\cdot75$ eV
(12) $A^+ + N_2 \rightarrow A + N_2^+ + 0\cdot18$ eV
(13) $A^- + O_2 \rightarrow A + O_2^- + 3\cdot68$ eV
(14) $O_2^+ + e \rightarrow O + O + 6\cdot96$ eV
(15) $CO^+ + e \rightarrow C + O + 2\cdot90$ eV
(16) $N_2^+ + e \rightarrow N + N + 5\cdot82$ eV
(17) $NO^+ + e \rightarrow N + O + 2\cdot74$ eV
(18) $CO_2^+ + e \rightarrow CO + O + 8\cdot33$ eV

Table 1.4: Some Ionosphere Constituents

SOME ION STATES AND ASSOCIATED THRESHOLDS FOR PHOTOIONIZATION

Parent Neutral	Product Ion	Electron Removed	Threshold in eV
$O(^3P)$	$O^+(^4S)$	$2p$	13·6
	$O^+(^2D)$	$2p$	16·9
	$O^+(^2P)$	$2p$	18·6
	$O^+(^4P)$	$2s$	28·5
	$O^+(^2P)$	$2s$	40·0
$A(^1S)$	$A^+(^2P)$	$3p$	15·8
	$A^+(^2S)$	$3s$	29·2
$O_2(^3\Sigma_g^-)$	$O_2^+(^2\Pi_g)$	$\pi_g 2p$	12·1
	$O_2^+(^4\Pi_u)$	$\pi_u 2p$	16·1
	$O_2^+(^2\Pi_u)$	$\pi_u 2p$	17·0
	$O_2^+(^4\Sigma_g^-)$	$\sigma_g 2p$	18·2
	$O_2^+(^2\Pi_u)$	$\sigma_u 2s$	~28
	$O_2^+(^2\Pi_g)$	$\sigma_g 2s$	~40
$N_2(^1\Sigma_g^+)$	$N_2^+(^2\Sigma_g^+)$	$\sigma_g 2p$	15·6
	$N_2^+(^2\Pi_u)$	$\pi_u 2p$	16·7
	$N_2^+(^2\Sigma_u^+)$	$\sigma_u 2s$	18·8
	$N_2^+(^2\Sigma_g^+)$	$\sigma_g 2s$	~35
$CO(^1\Sigma^+)$	$CO^+(^2\Sigma^+)$	$\sigma 2p$	14·0
	$CO^+(^2\Pi_i)$	$\pi 2p$	16·6
	$CO^+(^2\Sigma^+)$	$\sigma 2s$	19·7
$CO_2(^1\Sigma_g^+)$	$CO_2^+(^2\Pi_g)$	$1\pi_g$	13·8
	$CO_2^+(^2\Pi_u)$	$1\pi_u$	17·3
	$CO_2^+(^2\Sigma_u^+)$	$3\sigma_u$	18·1

All atmospheric motions are ultimately driven by pressure forces induced by thermal gradients and supported by complex feedback mechanisms (5:110). Hence, atmospheric circulation is driven by heating due to absorption of solar and infrared radiation by dust and CO_2 as well as sensible heat exchange with the ground (17:322). Furthermore, the global pattern of the atmospheric circulation of Mars shows many superficial similarities to the Earth, although the causes of motion arise from different circumstances.

The most important of these are the ability of the Martian air to adjust rapidly to local conditions of solar heat input, the lack of oceans which have a large thermal inertia, the great range in altitude on the surface, the strong internal heating of the atmosphere due to suspended dust, and, finally, the seasonal deposition and release of a large fraction of the atmosphere by the polar caps (49:298). Knowledge of winds is based on inferences from a global series of measurements made by Mariner 9. These data can be related to the zonal wind field if we assume terrestrial conditions (18:423). The predicted wind fields show a strong dependence on the Martian season since large horizontal temperature gradients build up across the edge of the newly forming polar cap in autumn and winter (49:298). The result is the formation at high latitudes of strong jet streams with eastward velocities in excess of 100 m/s (37:234). On Mars, unlike the Earth, there is also a

relatively strong meridional circulation that transports the atmosphere to and from the winter and summer poles (5:121).

The general circulation pattern is occasionally unstable and exhibits large-scale wave motions and instabilities (5:121). A wave pattern such as this is called a Rossby regime and is characterized by baroclinic instability, which has been observed with Mariner 9 TV observations (29:373). The three dimensional wave pattern is shown in Fig. 1.7 (5:116). Smaller scale wave motions and tides, driven by the Sun and surface topography, include a strong diurnal component and are present everywhere in the atmosphere, resulting in the complex vertical structure (18:439). This turbulence is probably why the atmosphere maintains a uniform composition to extremely low pressure levels and is presumably also an important factor in maintaining the large quantity of dust supported in the atmosphere. Occasionally, for reasons not fully understood, the atmospheric dust develops into planet-wide global dust storms that obscure the planet and reduce atmospheric transmission (49:297).

In summary, the recent space probe data indicate that the atmosphere of Mars is both position dependent, through latitude and longitude effects, and time dependent through such effects as these: diurnal and seasonal, annual motion, solar activity, and dust storm effects.
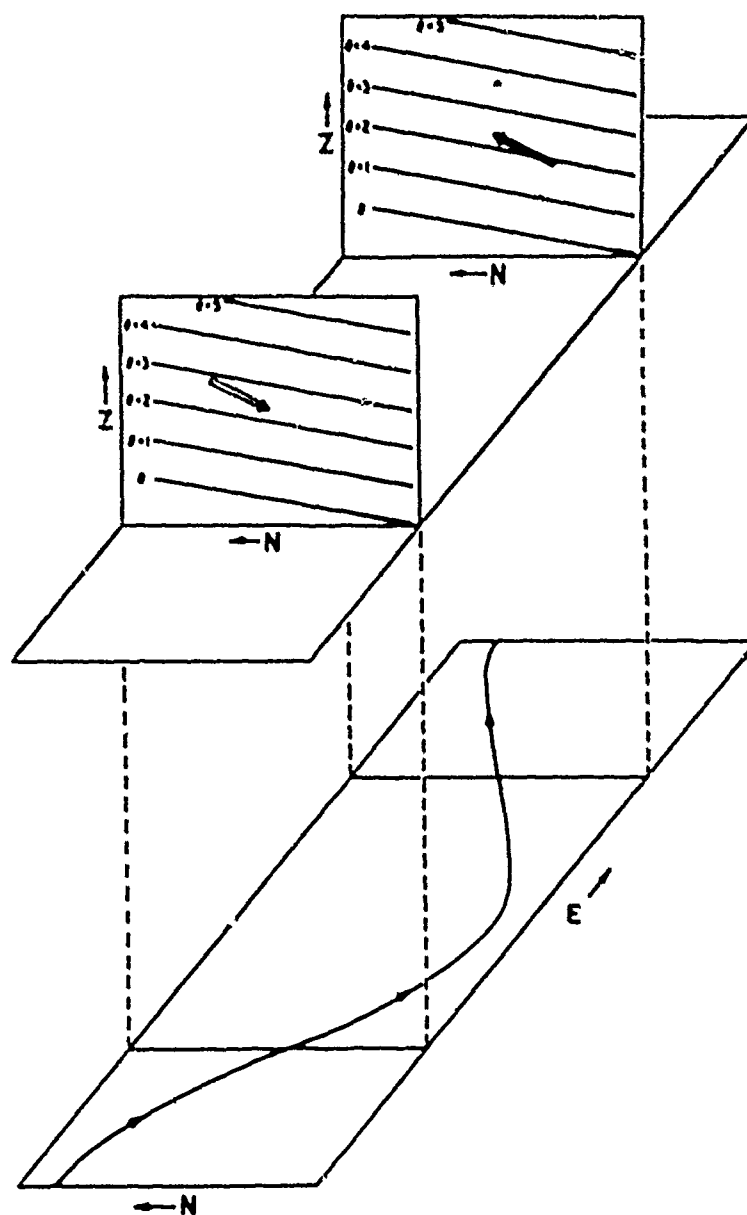
·Vertically exploded view of a wave of short length. The lower portion shows a single streamline of the wave while the upper portion shows (1) the distribution of potential temperature in two vertical, north-south cross sections through the inflection points of the wave and (2) the displacements of air produced by the wave (double arrows). In a short wave the slope of the displacements is greater than the slope of the potential isotherms.

Figure 1.7: Rossby Circulation Regime in Three Dimensions

III. Atmosphere Models

To study the effects of aerodynamic forces on trajectories at orbital speeds, it is necessary to model the planetary atmosphere in which the flights take place. The overriding feature of the atmosphere, as far as the spacecraft is concerned, is the density (47:1). Therefore, the concern in modeling the atmosphere is to conveniently and accurately represent the density.

This study will not model all the atmospheric effects present in the Martian atmosphere which contribute to its density. It is meant to be an initial attempt at modeling the Martian atmosphere dynamically. Only long term effects are kept; short term fluctuations are averaged out or an average value is assigned for the effect. There is some doubt in much of the work on Mars due to assumptions that are not proven to be completely accurate as yet (5:184). As a result, empirical data will be used to provide typical or reasonable values whenever possible. Both dynamic and static models use 1000 km for the limit of atmospheric drag effects; while the ionosphere has hydrogen ions as high above the surface as 10,000 km the first ions that cause significant loss of momentum upon impact are located at about 1000 km (37:210). Finally, both models contain some error in their calculation of pressure due to the fact that

pressure is supposed to be calculated with respect to altitude from the local Martian surface, not with respect to distance from the mass center. However, more detailed knowledge of topography would be necessary and the complexity is beyond the intended scope of this thesis. Instead, the dynamic model uses a reference pressure spheroid, and the static model essentially uses the Martian center of mass.

Dynamic Model

Because the mass density of the Martian atmosphere is heavily time dependent, an accurate calculation of the atmospheric forces on low altitude Martian satellites requires a time dependent atmospheric model. This highly variable nature of the Martian atmosphere means predictions of mass density at a specific time at a specific position are likely to be greatly in error (9:1). However, over a long term period, mass density can be predicted with acceptable accuracy.

This atmosphere model includes seasonal and diurnal variation, dust storm effects, solar activity effects, and the effect of the orbital position of Mars. The change in surface pressure due to polar cap sublimation/condensation is viewed as averaged out over the long term of these orbits. Furthermore, near surface variations and variations due to such effects as topography are viewed as short term

22

effects only. Finally, the complex wave perturbation motion in the atmosphere and related latitude and longitude gradient representations are left for follow-on work.

Reference Surface

All altitudes are measured with respect to a 6.1 millibar pressure spheroid (15:4321). Since Mars has no oceans it has no sea level to use as a reference. Instead, a reference pressure spheroid is determined by picking the spheroid which in a least squares sense best fits Mariner occultation data for a 6.1 mbar isobar surface. This spheroid nearly coincides with the average surface, ignoring topography, and is specified by these ellipsoidal semiaxes:

$$A = 3394.67 \text{ km}$$
$$B = 3393.21 \text{ km} \qquad\qquad (3.1)$$
$$C = 3376.78 \text{ km} ,$$

where A,B are in the equatorial plane, C is polar, and the A axis is oriented to the longitudinal angle 108.5° (19:324 and 6:4353). The areocentric coordinate system is the Mars-centered coordinate system; it is equivalent to the Earth-based longitude and latitude system. The fundamental plane is the Martian equatorial plane, and the principal axis is taken as pointing towards the Martian vernal equinox (14:148). The Prime Meridian for Mars is set at a small crater named Airey-0. The celestial longitude of the Sun,

L_s, in areocentric coordinates is an angular measure of the planet's orbital position.

Solar Activity Variation Effects

The Martian atmosphere is extremely sensitive to solar radiation and responds quickly to any changes in radiation intensity (32:420). Both temperature and density are affected (36:214). The two largest effects, the 11.04 year sunspot cycle and the 26.35 day period of the Sun's rotation (the synodic period with respect to Mars), can be modeled for an average intensity over a long term period (9:3 and 47:2).

A common measure of solar radiation intensity used in the literature is the solar $F_{10.7}$ centimeter radio flux, usually given in units of $10^{-22} W/m^2 Hz$ (19:4362). Following the method in reference (10), $F_{10.7}$ can be modeled using empirical data to create an average amplitude function:

$$F_{10.7} = \left[75 + 60 \left[1 - \cos \left[\frac{2Y*PI}{11.04} + \frac{PI}{6} \left[1 - \cos \left[\frac{2Y*PI}{11.04} \right] \right] \right] \right] \right]$$
$$\times \left[1 + B \sin \left[\frac{2d*PI}{26.35} \right] \right], \tag{3.2}$$

where PI=3.141592654, Y is the time interval in years from April 1, 1976, d is the time interval in days measured from a reference date chosen to match available Viking 1,2 Lander

24

data, and B is 0.0011 times the value of $F_{10.7}$ with the short-term variation averaged out, i.e., B is the first bracketed term times 0.0011. This equation is suitable for long term orbits and will be used in various other equations.

Effect on Temperature

The $F_{10.7}$ solar radiation intensity is used to calculate the exosphere temperature, T_∞. The exosphere begins where the mean free path of atmosphere constituents equals their scale height (21:28). This calculation is modeled using empirical data for amplitudes and modeling the distance of the planet from the sun (8:3). The equation representation is

$$T_\infty = 205 \text{ K} \left[\frac{a}{R} \right]^2 \left[\frac{F_{10.7} + 75}{150} \right], \quad (3.3)$$

where (a/R) is the ratio of the mean solar distance to the current solar distance, and the radiation intensity's decay with the square of the distance is included through $(a/R)^2$.

Effect on Density

Compared to the Earth, the ʼan atmosphere is transparent to energy radiation and without oceans does not store heat as readily. As a result, the local effect

25

differs from that on Earth (42:3969). The response of the Martian atmosphere to solar radiation is a function of time and can be broken down into two effects: seasonal variations and diurnal variations. Furthermore, time can be treated as a function of the local angle of the Sun.

Seasonal Variation

A simple way to relate this effect to time is to express it as a function of the difference in latitude of the Sun, SNLAT, and the latitude of the spacecraft, SCLAT. This can be modeled as a correction to the turbopause altitude, Z_f, where Z_f is defined as the upper limit of the thermosphere or lower atmosphere (8:3). The amplitude of this effect is very small (21:25 and 39:4367), and in the absence of better information has been set to $\epsilon_s = 0.1$ km. The empirical equation in terms of turbopause altitude is

$$\Delta Z_f = \epsilon_s \cos(SNLAT - SCLAT). \qquad (3.4)$$

Diurnal Variation

The diurnal effect is expressed as a function of local time in radians by relating time to the difference in longitude of the Sun, SNLONG, and the longitude of the spacecraft, SCLONG. In addition, (8:3) adds a two hour lag, set equal to PI=3.14..., similar to that seen in the Earth's atmosphere. Thus, the resulting equation for time is

26

$$TIME = (SCLONG - SNLONG) + PI. \qquad (3.5)$$

However, this effect falls off with latitude until it becomes negligible in the region of the poles since less sunlight reaches there, i.e., temperature is latitude dependent (21:25). As a result, the final equation will include a latitude effect, cos(SCLAT), chosen to make this effect vanish at the poles.

Viking lander data showed the diurnal effect decreasing with decreasing altitude, being only a minor variation at the surface (39:4367 and 47:2). As a result, this effect is deemed negligible in the lower atmosphere and is treated only as a variation in the upper atmosphere. There, the effect is separated into two components:

1) A correction to turbopause altitude, Z_f:

As with the seasonal effect, the amplitude of this correction is small (18:439) and, in the absence of better information, is set to $\epsilon_D = 0.1$ km. According to (10:331), the best empirical fit, including latitude drop off, is

$$\Delta Z_f = \epsilon_D \cos(TIME - 3.6651914)\cos(SCLAT). \qquad (3.6)$$

2) A variation in the mixing ratio of monatomic oxygen above the thermosphere:

From empirical data, monatomic oxygen is the dominant constituent at this altitude (34:4348). This variation is accepted in (10:331 and 31:4384) as being represented by the following equation for the mixing ratio at the turbopause:

$$f_0 = 0.02 \ (1 - (.5 \ \sin(TIME) \sqrt{\cos(SCLAT)}). \qquad (3.7)$$

Dust Storm Effects

While dust is always present in the Martian atmosphere, the primary turbidity effects are those of the global dust storms which occur annually as Mars passes perihelion (38:262). Global dust storms are those dust storms that grow out of local dust storms at certain preferred locations and seasons to obscure the entire planet and throw dust into the atmosphere as high as 60 km (49:302). They cause both density and temperature changes. However, observed variation from year to year has been great and can be expected to remain so (49:296). Therefore, the only way to model this effect is to choose a typical year global dust storm as the "average" effect. For this purpose, Viking data on the 1977 storms is chosen. These storms showed a double peak with maximum thicknesses of 7.5 km with onset at solar longitude of $L_s = 210°$ and 13.5 km at solar longitude of $L_s = 270°$ in the areocentric system (49:290). Note, the perihelion of Mars corresponds to an areocentric solar

longitude of about $L_S = 250'$. The onset of all global dust storms was within 60' of this longitude (49:299).

The dust storm effect appears as an isothermal layer inserted at the bottom of the Martian atmosphere, with the higher thermal layers pushed upward by this amount (26:493). Therefore, using Viking data the turbidity layer is modeled as (10:332)

$$\Delta Z_{Ds} = 1.2 \text{ km} + \sum_{i=1,2} \left[\frac{\Delta Z_i}{0.65} \right] \left[1 - e^{-(\Delta L_i/5)} \right] \left[e^{-(\Delta L_i/35)} \right] \quad (3.8)$$

where $\Delta Z_1 = 7.5$ km,   (3.9a)

      $\Delta Z_2 = 13.5$ km,   (3.9b)

      $\Delta L_1 = L_S - 210'$,   (3.9c)

      $\Delta L_2 = L_S - 270'$.   (3.9d)

The equation uses 1.2 km as an average impact on the turbopause, and the right term fits the empirical data for the additional overlapping effects of the two peaks at 210' and 270' (49:290).

Annual Motion Effects

The annual motion of Mars about the Sun changes the distance between the two bodies as well as the orientation of the planet to the Sun's radiation. These changes result in variation in the temperature profile of the atmosphere in addition to changes in the "size" (and so pressure) of the

atmosphere -- the atmosphere alternately swells and shrinks. However, the pressure variation is less important than the other effects. Annual motion is basically a time effect which can be expressed as a function of both the longitude of the Sun in areocentric coordinates, L_s, (measured from the Martian autumnal equinox, which corresponds to a heliocentric longitude for Mars of 85°), and the Mars-Sun distance R expressed nondimensionally as (a/R) (8:4). The dust storm effect in the last section is basically an annual motion effect.

Empirical data show a good approximation for the annual motion effect on pressure is (9:5)

$$P = P_0 (1 - 0.24 \sin(L_s - 59°)). \qquad (3.10)$$

This pressure effect can be included by correcting the 6.1 mbar ellipsoid used as the reference level in this model atmosphere by (10:332)

$$\Delta R_{6.1} = -11.3 \ln[1 - 0.24 \sin(L_s-59°)] \text{ km}. \qquad (3.11a)$$

In recognition of the uncertainty in this term, and to avoid repeated evaluation of the log term, this is approximated to the first order of the logarithmic series for $\ln(1-x) = -(x+x^2/2+...) = -(-11.3)(-0.24\sin())$ by

$$\Delta R_{6.1} = -2.8 \sin(L_s - 59°) \text{ km}. \qquad (3.11b)$$

This is based on an average temperature over the entire day at the reference ellipsoid of 220 K (21:25).

The two most important effects, the temperature profile variation and the change in size of the atmosphere are modeled using empirical data. Basically, accepted usage is to form a temperature function which is piecewise linear between specified data points. One such function is given in the following table (39:4364 and 9:5):

Table 3.1: Piecewise Linear Temperature Function	
of the Martian Thermosphere	
(Where the ratio (a/R) is the semimajor axis of Mars'	
orbit divided by the current Mars to Sun distance.)	
Altitude (km)	Temperature (K)
Reference, R61MB, Z=0	$220 \cdot (a/R)$
$ZL = \Delta Z_{DS}(2.75)$	$220 \cdot (a/R)$
$ZA = ZL + 32(a/R)$	$140 \cdot (a/R)$
$ZB = \Delta Z_{DS} + 100(a/R)$	$140 \cdot (a/R)$
$ZF = \Delta Z_{DS} + 125(a/R) + \Delta Z_{SN}$	$172.5 \cdot (a/R)$

where ΔZ_{DS} is the dust storm correction and ΔZ_{SN} is the seasonal and diurnal correction. The table represents two isothermal layers and two layers of constant temperature lapse rates (24). Furthermore, both the exosphere

31

temperature and the solar radiation flux, $F_{10.7}$, depend on the annual motion.

Density Calculations

For mass density calculations, the atmosphere can be divided into two regimes: a lower neutral atmosphere, called the thermosphere, and an upper layer, called the ionosphere (21:228). The dividing line between these two layers is called the turbopause and is stated as an altitude, Z_f. This altitude varies between approximately 115 km to 150 km, with an average value of about 130 km (34:4346). This average altitude also represents the region of maximum ion density, i.e., this is where a spacecraft would "enter" the atmosphere. Consequently, satellites are placed in orbit above this level and most of the satellite atmospheric drag is in the upper atmosphere regime. The two regions do not behave the same (18:435).

The lower atmosphere or thermosphere can be treated as a neutral gas with an ideal gas molecular weight of $m = 43.3$ gm/mole based on Viking 2 data (39:4368). The thermal layers of this lower atmosphere vary with annual motion and a temperature-altitude model is given in Table 3.1. Mass density is calculated using pressure and temperature information in the ideal gas law. The pressure in this regime is known to follow an exponential law (5:232), and

32

the pressure is found by solving the barometric law analytically. In the two isothermal layers, the pressure is calculated using the equation (21:27)

$$P = P_i \, e^{((-z-z_i)/H_i)} \tag{3.12}$$

where P_i is the pressure at the lower bound of the layer, z_i, and the scale height for the layer is given by

$$H_i = kT_i/mg_i, \tag{3.13}$$

where k = Universal gas constant,

T_i = temperature in the layer (K),

m_i = mean molecular weight

g_i = local gravity.

In the two layers of constant temperature lapse rate (linear temperature function), the pressure is calculated differently. The generalized equation for the molecular weight, m, of nonisothermal regimes changes equation (3.13) to (39:4368)

$$m = - \left[\frac{k \, T}{P \, g} \right] \left[\frac{dP}{dz} \right] , \tag{3.14}$$

where P is the pressure and z is the altitude. Rearranging this equation and multiplying by (dT/dT) yields:

33

$$\frac{dP}{P} = (mg/k)\ \frac{dz}{T}\ \frac{dT}{dT} = (mg/k)\ \frac{dz}{dT}\ \frac{dT}{T}$$

$$= (mg/kT')\ \frac{dT}{T}, \qquad (3.15a)$$

where T' is (dT/dz). Integration yields:

$$\ln(P_2/P_1) = (mg/kT')\ \ln(T_2/T_1)$$

$$= \ln(T_2/T_1)^{(mg/kT')}. \qquad (3.15b)$$

Taking the antilogarithm produces:

$$P = P_i(T/T_i)^{(mg_i/kT')}, \qquad (3.16)$$

where i refers to the lower bound of the layer Z_i as before, and T' is approximated as the temperature lapse rate $(\Delta T/\Delta Z)$. Once the pressure is known, the mass density can be calculated. The standard relation between pressure and the mass density, μ, is (34:4344):

$$dp/dz = -\mu g. \qquad (3.17)$$

Substituting this into equation (3.14) yields the equation:

$$\mu = \frac{mp}{kT}. \qquad (3.18)$$

34

The upper atmosphere or ionosphere does not follow a simple exponential, ideal law formulation. This regime is composed of dissociated ions and molecules which are not well mixed (19:4351). Therefore, the mass density must be calculated using properties of the constituents of this layer. The most straightforward way to calculate the mass density is to use the number densities of the constituents, modifying the process with a measure of the mixture ratio between them. There are nine constituents included in this model (see Table 3.2).

Table 3.2: Atmosphere Model Ionosphere Constituents	
Constituent	Molecular Weight (gm/mole)
Carbon Dioxide (CO_2)	44.01
Monatomic Oxygen (O)	16.0
Molecular Nitrogen (N_2)	28.012
Argon (Ar)	39.948
Carbon Monoxide (CO)	28.01
Molecular Oxygen (O_2)	32.0
Helium (He)	4.0
Monatomic Hydrogen (H)	1.0
Molecular Hydrogen (H_2)	2.0

The mass density is calculated in this region using the methods found in references (9) and (10). The number

densities are calculated as a function of the geopotential altitude, x. The geopotential altitude is defined as:

$$x = \left[\frac{(z-z_f)}{1 + \frac{(z-z_f)}{R_f}} \right] \qquad (3.19)$$

where z = altitude of spacecraft above pressure reference surface

z_f = altitude of turbopause

R_f = areocentric distance of turbopause.

The temperature is calculated using

$$T = T_\infty - (T_\infty - T_f) \, e^{-\frac{x}{a}} \qquad (3.20)$$

where $\quad a = (T_\infty - T_f) \, / \, (\Delta T/\Delta Z)_f = T_\infty/18, \qquad (3.21)$

T_f = temperature at turbopause,

$(\Delta T/\Delta Z)_f$ = approximation for T' at turbopause.

The partial pressure for a constituent i is calculated using

$$P_i = P_f \, f_i \, e^{-\frac{x}{H_i}} \, (T_f/T)^{\frac{a}{H_i}}, \qquad (3.22)$$

where f_i is the mixing ratio of the constituent at the turbopause, Z_f, (34:4345) and H_i is the constituent scale height defined by (34:4346)

$$H_i = \frac{k\,T}{m_i g_f}, \qquad\qquad (3.23)$$

with m_i being the molecular weight of the constituent and g_f being referenced to the turbopause. Now, use the partial pressure to calculate the number density in the rewritten gas law equation:

$$n_i = \frac{p_i\,N}{k\,T}. \qquad\qquad (3.24)$$

Finally, the mass density is found by summing the number densities and converting to mass units:

$$\mu = \frac{\sum_i n_i\,m_i}{N}, \qquad\qquad (3.25)$$

where $N = 6.023 \times 10^{26}$ /kg mole , $k = 8314.39$ J/kg mol K, and $i = 1,\dots,9$ for the nine constituents. The mass density, μ, can now be used in drag equations to determine atmospheric drag on a spacecraft in the orbital equations of motion.

Static Model

The static atmosphere model is a much simpler model of the atmosphere. It is not meant to be a highly accurate representation of the actual Martian atmosphere but rather a

quick means to obtain an upper bound approximation of the mass density. A number of fundamental assumptions are made following the methods introduced in reference [47]. These assumptions greatly streamline the necessary calculations, which saves valuable computer time if great precision to real Martian atmospheric conditions is not required.

The static atmosphere is modeled quite differently from the dynamic model. The effect of composition of the atmosphere is assumed to be negligible, although that composition is very important in understanding the ionosphere. Instead, the atmosphere is treated as a uniform gas of unvarying composition. This is a reasonable assumption if the atmosphere is modeled to provide an upper bound on density rather than match varying actual conditions. Also, a simple "spherical symmetry" modified by ellipticity is assumed, i.e., the atmospheric pressure is essentially a function only of radial distance from the center of the planet. As mentioned before, this should be a function of altitude, which is a function of topography. However, this model is meant to be a very convenient way to estimate density. Also, solar radiation effects on the atmosphere are regarded as being negligible. Again, this is acceptable within the framework of the intent of the model. Furthermore, the atmosphere is assumed to be nonrotating. This is a reasonable assumption since the aerodynamic forces generated by the rotation have larger effects only at low

altitudes. One measure of the effect is to examine maximum rotational speed of Mars at the equator. This can be represented as the ratio of the surface rotational speed divided by the circular orbital speed at the surface expressed as a percentage. For Mars, this measure is given as seven percent, which is a maximum (47:3). Therefore, this is a reasonable assumption. The net effect of the above assumptions is that there is r 'ime dependence built into the model. Another very important assumption is that the density decreases exponentially with altitude. Combining equations (3.17) and (3.18) and reorganizing after taking the resulting derivative yields

$$\frac{d\mu}{\mu} = -\left[\frac{gm}{kT} + \frac{1}{T}\frac{dT}{dr} \right] dr \qquad (3.26a)$$

$$= - \beta\, dr, \qquad (3.26b)$$

where β is defined as the bracketed term above and is the reciprocal of the scale height ($1/H$). If β is considered to be constant over some small altitude interval, the integrated density function is

$$\mu = \mu_0\, e^{-\beta(z-z_0)} \qquad (3.27)$$

or $\qquad \mu = \mu_0\, e^{-(z-z_0)/H}.$

39

As a result, the only elements of the model that must be determined under these assumptions are the input values for the reference density μ_0, the corresponding reference altitude, and the scale height H for the altitude interval. Unfortunately, there are many models and various data in the literature and they don't always agree closely. Therefore, a representative set must be chosen from empirical data.

The scale height has been observed to increase with altitude from about 10 km at the surface to a maximum average ionospheric scale height of 38.5 km (26:484). Since the spacecraft will be spending its atmospheric time in the ionosphere, the scale height should be somewhere near this upper number. Reference (5:156) uses Mariner data to give an upper bound value for scale height of about 35 km. Therefore, a reasonable scale height datum in this range is 36 km for the ionosphere. According to Viking 1 empirical data this corresponds to a reference height of about 361 km and reference density of approximately 6×10^{-13} kg/m^3 (39:4373). These values result in a density equation of

$$\mu = (6 \times 10^{-13} \text{ kg/m}^3) \, e^{(361 \text{ km} - z)/36 \text{ km}} \qquad (3.28)$$

This is the equation used in the static atmosphere model to calculate the mass density.

IV. Orbital Equation Model

A model for orbital motion about Mars is developed using Keplerian motion (Lagrange's Planetary Equations) subject to certain perturbations. The perturbations included are the aspherical gravity field of Mars (geopotential or central body disturbing potential), the gravitational attraction of the sun (third body disturbing potential), atmospheric drag (using two different models to generate atmospheric mass density for the calculation), and solar radiation pressure. This section addresses each part of the overall model in order to build the complete thesis model.

Lagrange's Planetary Equations

Lagrange's Planetary Equations are usually written in terms of the classic orbital elements a, e, i, Ω, w, and M. However, there are disadvantages to using these elements as the variables in the orbital differential equations. The typical Lagrange's Planetary Equations given in (20:29) are:

$$\frac{da}{dt} = \frac{2}{na} \frac{\partial R^*}{\partial M} \tag{4.1.1a}$$

$$\frac{de}{dt} = \frac{1-e^2}{na^2 e} \frac{\partial R^*}{\partial M} - \frac{\sqrt{1-e^2}}{na^2 e} \frac{\partial R^*}{\partial e} \tag{4.1.1b}$$

$$\frac{d\omega}{dt} = -\frac{\cos i}{na^2 \sin i \sqrt{1-e^2}}\frac{\partial R^*}{\partial i} + \frac{\sqrt{1-e^2}}{na^2 e}\frac{\partial R^*}{\partial e} \qquad (4.1.1c)$$

$$\frac{di}{dt} = \frac{\cos i}{na^2 \sin i \sqrt{1-e^2}}\frac{\partial R^*}{\partial \omega} - \frac{1}{na^2 \sin i \sqrt{1-e^2}}\frac{\partial R^*}{\partial \Omega} \qquad (4.1.1d)$$

$$\frac{d\Omega}{dt} = \frac{1}{na^2 \sin i \sqrt{1-e^2}}\frac{\partial R^*}{\partial i} \qquad (4.1.1e)$$

$$\frac{dM}{dt} = n - \frac{1-e^2}{na^2 e}\frac{\partial R^*}{\partial e} - \frac{2}{na}\frac{\partial R^*}{\partial a}, \qquad (4.1.1f)$$

where R^* is the disturbing potential, assumed a function of the classical elements, and n is the mean motion.

As can be seen above, i and e are in the denominators of some of these differential equations and will produce singularities if they become vanishingly small. To avoid this problem, two actions are taken. First, to avoid the singularity in inclination, the inclination is never set equal to zero. Second, new orbital elements, designated h and k, are introduced which will eliminate the singularity due to zero eccentricity (28:3-1):

$$h = e \sin\omega \qquad (4.1.2a)$$

$$k = e \cos\omega. \qquad (4.1.2b)$$

To facilitate the numerical integration, a singly averaged method is used. This method removes the fast

42

variable (terms involving the mean anomaly M) in the geopotential and third body potential before numerical integration. However, terms involving the mean anomaly but giving rise to resonant terms with the geopotential tesserals are retained. This is exactly what we want since only long term orbital behavior is of interest. To emphasize resonance, the mean anomaly will be replaced with another new orbital parameter called the stroboscopic mean node, L_N (16:167-189).

While affecting all Keplerian elements, the greatest effect of resonance shows up in the longitude dependent L_N (20:49-56). The stroboscopic mean node is defined as follows:

$$L_N = \left[\frac{M + \omega}{S_0} \right] + (\Omega - \theta_g), \qquad (4.1.3)$$

where S_0 is the ratio of two relatively prime integers, P/Q, approximating the number of nodal crossings per planet revolution, and θ_g is the Prime Meridian angle. Reference (20) provides a good description of the physical meaning of the stroboscopic mean node.

Numerical quadrature is used to average the potential due to solar radiation pressure and to drag. The resulting averaged equations of motion are integrated numerically using a multistep, variable order and variable step-size integrator (28). Due to the elimination of the fast

43

variable in the equations of motion, large step sizes of the order of days are possible. This suits the long term orbit studies desired, but eliminates short term information since that information has been averaged out (28:1-2).

The orbital equation model uses a planet equator of epoch coordinate system, which is a non-rotating coordinate system where the X-Y plane is the equator plane, defined at some epoch, of the planet being orbited by the spacecraft. Polar motion is ignored. Reference (28) provides a set of recommended orbital elements for the sun with respect to Mars' equator and equinox of epoch and the location of the Prime Meridian for three epochs. The closest epoch to the mission is chosen; the positional error introduced is less than 0.1° if the solar ephemeris reference date is very close to the mission date (28:2-1,2-11).

Lagrange's Planetary Equations must be transformed from the classical Keplerian orbital element set to the new orbital parameter set of a, h, i, k, Ω, L_N. Substituting derivatives of the disturbing potential into Equs. (4.1.1) and using the chain rule to introduce the new orbital elements yields (30:3-2):

$$\frac{da}{dt} = \frac{2}{na} \cdot \frac{1}{S_0} \frac{\partial R}{\partial L_N} \tag{4.1.4a}$$

$$\frac{dh}{dt} = \frac{\sqrt{1-e^2}}{na^2} \frac{\partial R}{\partial k} - \frac{k \cot i}{na^2\sqrt{1-e^2}} \frac{\partial R}{\partial i} - \frac{h\beta'\sqrt{1-e^2}}{na^2 S_0} \frac{\partial R}{\partial L_N} \tag{4.1.4b}$$

44

$$\frac{di}{dt} = \frac{\cot i}{na^2\sqrt{1-e^2}}\left[k\,\frac{\partial R}{\partial h} - h\,\frac{\partial R}{\partial k} + \frac{1}{S_0}\frac{\partial R}{\partial L_N}\right]$$

$$- \frac{1}{na^2\sin i\,\sqrt{1-e^2}}\left[\frac{\partial R}{\partial \Omega} + \frac{\partial R}{\partial L_N}\right] \qquad (4.1.4c)$$

$$\frac{dk}{dt} = -\frac{\sqrt{1-e^2}}{na^2}\frac{\partial R}{\partial h} + \frac{h\cot i}{na^2\sqrt{1-e^2}}\frac{\partial R}{\partial i} - \frac{k\,\beta'\sqrt{1-e^2}}{naS_0}\frac{\partial R}{\partial L_N} \qquad (4.1.4d)$$

$$\frac{d\Omega}{dt} = \frac{1}{na^2\sin i\,\sqrt{1-e^2}}\frac{\partial R}{\partial i} \qquad (4.1.4e)$$

$$\frac{dL_N}{dt} = \frac{n}{S_0} - \frac{d\theta_g}{dt} + \frac{1}{na^2S_0}\left[\beta'\sqrt{1-e^2}\left[h\,\frac{\partial R}{\partial h} + k\,\frac{\partial R}{\partial k}\right]\right.$$

$$\left. - 2a\,\frac{\partial R}{\partial a} + \frac{S_0 - \cos i}{\sin i\,\sqrt{1-e^2}}\frac{\partial R}{\partial i}\right], \qquad (4.1.4f)$$

where $e = \sqrt{h^2 + k^2}$, $n = \sqrt{\mu/a^3}$, and $\beta' = \dfrac{1}{1 + \sqrt{1-e^2}}$.

Central Body Disturbing Potential (Martian Gravity)

This model for the aspherical gravity field perturbation (geopotential) is developed in detail in references (11),(20), and (48). The geopotential is expressed by the following relationship where the equation is made

45

dimensionless using the gravitational parameter μ and planetary radius R_e:

$$V(r,\theta,o)= \frac{-\mu}{r} \sum_{l=0}^{\infty} \sum_{m=0}^{l} \left[\frac{r}{R_e}\right]^{-l} P_{lm}(\sin\theta)(C_{lm}\cos mo + S_{lm}\sin mo).$$

$$(4.2.1)$$

This equation is transformed into a Keplerian variable form using two new functions that depend on Keplerian elements: the inclination function $F_{lmp}(i)$ and the eccentricity function $G_{lpq}(e)$. The complete derivation may be found in (11) or (20).

The inclination function is defined as follows:

$$F_{lmp}(i)=\sum_{t=0}^{tmax} \left[\frac{(2l-2t)!}{t!(l-t)!(l-m-2t)!2^{2l-2t}}\right] \sin^{l-m-2t}(i)$$

$$\times \sum_{s=0}^{m} \begin{bmatrix} m \\ s \end{bmatrix} \cos^s(i) \sum_{c} \begin{bmatrix} l-m-2t+s \\ c \end{bmatrix} \begin{bmatrix} m-s \\ p-t-c \end{bmatrix}(-1)^{c-k}, \quad (4.2.2)$$

where c = all integers where binomial coefficients are nonzero. The restrictions on binomial coefficients result in a lower limit on index c of $c_l=\max(0,p-t-m-s)$, and an upper limit of $c_u=\min(l-m-2t+s,p-t)$, $c_u \geq c_l$.

The eccentricity function is defined as follows:

$$G_{lp(2p-l)}=$$

$$\frac{1}{a^{l+1}(1-e^2)^{l-\frac{1}{2}}}\sum_{d=0}^{p'-1} \begin{bmatrix} l-1 \\ 2d+l-2p' \end{bmatrix}\begin{bmatrix} 2d+l-2p' \\ d \end{bmatrix}\begin{bmatrix} e \\ \frac{e}{2} \end{bmatrix}^{2d+l-2p'} \quad (4.2.3)$$

where $p' = \begin{cases} p & \text{for } p \leq l/2 \\ l-p & \text{for } p \geq l/2. \end{cases}$

Now the disturbing function may be expressed as

$$R = \sum_{l=2}^{\infty} \sum_{m=0}^{l} V_{lm}, \qquad (4.2.4)$$

where

$$V_{lm} = \frac{\mu R_e^l}{a^{l+1}} \sum_{p=0}^{l} F_{lmp}(i) \sum_{q=-\infty}^{\infty} \left[G_{lpq}(e) S_{lmpq}(w,M,\Omega,\theta) \right] \qquad (4.2.5)$$

and $S_{lmpq} = \begin{cases} C_{lm}\cos m\sigma + S_{lm}\sin m\sigma, & l-m \text{ even} \\ -S_{lm}\cos m\sigma + C_{lm}\sin m\sigma, & l-m \text{ odd} \end{cases} \qquad (4.2.6)$

with $\sigma = (l-2p)w + (l-2p+q)M + m(\Omega-\theta)$. $\qquad (4.2.7)$

Alternately, converting to the modified elements using the equations and definitions in (28:3-4,7), V_{lm} becomes

$$V_{lm} = \frac{\mu R_e^l}{a^{l+1}} J_{lm} \sum_{p=0}^{l} F_{lmp}(i) \sum_{q=-\infty}^{\infty} \left[G'_{lpq}(e) S_{lmq}(h,k,L_N) \right]. \qquad (4.2.8)$$

Now substitute the derivatives of V_{lm} with respect to the modified orbital element set into Lagrange's Planetary Equations (4.1.4) to yield:

$$\frac{da}{dt} = \begin{cases} \dfrac{2}{naS_0} \dfrac{\mu R_e^l}{a^{l+1}} J_{lm} \sum_{m \, p=0}^{l} \left[F_{lmp} \; G'_{lpq} \; \dfrac{1}{m} \; \dfrac{\partial S_{lmq}}{\partial L_N} \right], & m \text{ not } 0 \\ 0, & m = 0. \end{cases} \qquad (4.2.9a)$$

$$\frac{dh}{dt} = \frac{\sqrt{1-e^2}}{na^2}\left[\frac{\mu R_e^l}{a^{l+1}} J_{lm} \sum_{p=0}^{l} F_{lmp}\left[G'_{lpq}\frac{\partial S_{lmq}}{\partial k} + S_{lmq}\frac{k}{e}\frac{dG'}{de}\right]\right]$$

$$-\frac{k \cot i}{na^2\sqrt{1-e^2}}\left[\frac{\mu R_e^l}{a^{l+1}} J_{lm}\sum_{p=0}^{l}\left[\frac{\partial F_{lmp}}{\partial i} G'_{lpq}(e)S_{lmq}\right]\right]$$

$$-\frac{h\beta'\sqrt{1-e^2}}{na^2 S_0}\left[\frac{\mu R_e^l}{a^{l+1}} J_{lm}\sum_{mp=0}^{l}\left[F_{lmp}\quad G'_{lpq}\frac{1}{m}\frac{\partial S_{lmq}}{\partial L_N}\right], \; m \text{ not } 0\right.$$

$$\left. 0 \text{ for } m = 0 \right. \tag{4.2.9b}$$

$$\frac{di}{dt} = \frac{\cot i \; k}{na^2\sqrt{1-e^2}}\frac{\mu R_e^l}{a^{l+1}}\frac{J_{lm}}{\sin i}\sum_{p=0}^{l}\left[F_{lmp}\quad G'_{lpq}\frac{\partial S_{lmq}}{\partial h} + S_{lmq}\frac{h}{e}\frac{dG'}{de}\right]$$

$$-\frac{\cot i \; h}{na^2\sqrt{1-e^2}}\frac{\mu R_e^l}{a^{l+1}}\frac{J_{lm}}{\sin i}\sum_{p=0}^{l}\left[F_{lmp}\; G'_{lpq}\frac{\partial S_{lmq}}{\partial k} + S_{lmq}\frac{k}{e}\frac{dG'}{de}\right]$$

$$+\frac{\cot i}{S_0 na^2\sin i\sqrt{1-e^2}} - \frac{1}{na^2 \sin i \sqrt{1-e^2}}$$

$$\times\quad \frac{\mu R_e^l}{a^{l+1}} J_{lm}\sum_{mp=0}^{l}\left[F_{lmp}\; G'_{lpq}\frac{1}{m}\frac{\partial S_{lmq}}{\partial L_N}, \; m \text{ not } 0\right.$$

$$\left. 0, \; m = 0. \right. \tag{4.2.9c}$$

$$\frac{dk}{dt} = -\frac{\sqrt{1-e^2}}{na^2}\frac{\mu R_e^l}{a^{l+1}} J_{lm}\sum_{p=0}^{l}\left[F_{lmp}\left[G'_{lpq}\frac{\partial S_{lmq}}{\partial h} + S_{lmq}\frac{h}{e}\frac{dG'}{de}\right]\right]$$

$$+\frac{h \cot i}{na^2\sqrt{1-e^2}}\frac{\mu R_e^l}{a^{l+1}} J_{lm}\sum_{p=0}^{l}\left[\frac{\partial F_{lmp}}{\partial i} G'_{lpq}(e)S_{lmq}\right]$$

43

$$- \frac{k \, \beta' \sqrt{1-e^2}}{n a S_0} \, \frac{\mu R_e^l}{a^{l+1}} \, J_{lm} \, m \sum_{p \equiv 0}^{l} \left[\begin{array}{l} F_{lmp} \, G'_{lpq} \, \frac{1}{m} \frac{\partial S_{lmq}}{\partial L_N}, \quad m \text{ not } 0 \\[1.5em] 0, \quad m = 0. \end{array} \right. \tag{4.2.9d}$$

$$\frac{d\Omega}{dt} = \frac{1}{n a^2 \sin i \sqrt{1-e^2}} \, \frac{\mu R_e^l}{a^{l+1}} \, J_{lm} \sum_{p \equiv 0}^{l} \left[\frac{\partial F_{lmp}}{\partial i} \, G'_{lpq}(e) S_{lmq} \right] \tag{4.2.9e}$$

$$\frac{dL_N}{dt} = \frac{n}{S_0} - \frac{d\theta_g}{dt} + \frac{1}{n a^2 S_0} \left[\beta' \sqrt{1-e^2} \right.$$

$$\times \left[h \left[\frac{\mu R_e^l}{a^{l+1}} \, J_{lm} \sum_{p \equiv 0}^{l} \left[F_{lmp} \, G'_{lpq} \frac{\partial S_{lmq}}{\partial h} + S_{lmq} \frac{h}{e} \frac{dG'}{de} \right] \right] \right.$$

$$\left. + k \left[\frac{\mu R_e^l}{a^{l+1}} \, J_{lm} \sum_{p \equiv 0}^{l} \left[F_{lmp} \, G'_{lpq} \frac{\partial S_{lmq}}{\partial k} + S_{lmq} \frac{k}{e} \frac{dG'}{de} \right] \right] \right]$$

$$+ 2a \left[(l+1) \frac{\mu R_e^l}{a^{l+2}} J_{lm} \sum_{p \equiv 0}^{l} \left[F_{lmp}(i) G'_{lpq}(e) S_{lmq} \right] \right]$$

$$+ \frac{S_0 - \cos i}{\sin i \sqrt{1-e^2}} \, \frac{\mu R_e^l}{a^{l+1}} \, J_{lm} \sum_{p \equiv 0}^{l} \left[\frac{\partial F_{lmp}}{\partial i} \, G'_{lpq}(e) S_{lmq} \right]. \tag{4.2.9f}$$

49

Solar Radiation Pressure Model

The acceleration of a satellite due to direct solar radiation pressure is given by (28:3-29):

$$\ddot{r} = \tau \, p_s \, \frac{A'}{m} \left[\frac{r_{sun}}{r_v} \right]^2 \hat{r}_v , \qquad (4.3.1)$$

where r = satellite position vector relative to planet center

r_{sun} = distance of the sun at 1 A.U.

r_s = position vector of the sun relative to planet center

$r_v = r - r_s$

p_s = radiation pressure

τ = dimensionless black body radiation constant

A' = effective spacecraft area for radiation pressure

m = mass of the satellite

$\hat{r}$ = unit vector

For an orbiting spacecraft, a standard approximation is to take $r_v \approx - r_s$. Also, since the orbital eccentricity of Mars is small, 0.093387, assume $r_s = a_p$, where a_p is the semimajor axis of Mars' orbit. Further assume $r_{sun} = a_e$, where a_e is the semimajor axis of the Earth's orbit, since its eccentricity is 0.0167. The effect of these assumptions is to change equation (4.3.1) to

$$\ddot{r} = - \frac{C_s \, A'}{m} \hat{r}_s , \qquad (4.3.2)$$

50

where
$$C_s = \tau \, p_s \, (a_e/a_p)^2. \qquad (4.3.3)$$

Equation (4.3.2) may be expressed as a gradient of a potential R^*:

$$\ddot{r} = \nabla R^*, \qquad (4.3.4)$$

where
$$R^* = -\frac{C_s \, A'}{m}\left[\underline{r} \cdot \hat{r}_s \right] \qquad \text{(vector form)} \qquad (4.3.5a)$$

or
$$R^* = -\frac{C_s \, A'}{m} \, r \cos S \qquad \text{(scalar form)} \qquad (4.3.5b)$$

where S = the planet centered angle between the Sun and the satellite. This angle (see occultation subsection) is

$$\begin{aligned}
\cos S = \; & C(\cos\Omega \, \cos u - \cos i \, \sin\Omega \, \sin u) \\
& + A(\sin\Omega \, \cos u + \cos i \, \cos\Omega \, \sin u) \\
& + B(\sin i \, \sin u),
\end{aligned}$$

where $A = \cos\delta \, \sin\alpha$
$B = \sin\delta$
$C = \cos\delta \, \cos\alpha$
δ = declination of the sun
α = right ascension of the sun
u = argument of latitude $(f+w)$.

For the potential above, R^*, in the classical orbital element set, the following partial derivatives are needed:

$$\frac{\partial R^*}{\partial a} = -\frac{C_s \, A'}{m} \, \frac{r}{a} \, \cos S \qquad (4.3.6a)$$

$$\frac{\partial R^*}{\partial e} = -\frac{C_s \, A'}{m}\left[\cos S \, \frac{\partial r}{\partial e} + r \, \frac{\partial(\cos S)}{\partial u} \, \frac{\partial u}{\partial e} \right] \qquad (4.3.6b)$$

$$\frac{\partial R^*}{\partial i} = - \frac{C_S A'}{m} r \frac{\partial(\cos S)}{\partial i} \tag{4.3.6c}$$

$$\frac{\partial R^*}{\partial \Omega} = - \frac{C_S A'}{m} r \frac{\partial(\cos S)}{\partial \Omega} \tag{4.3.6d}$$

$$\frac{\partial R^*}{\partial w} = - \frac{C_S A'}{m} r \frac{\partial(\cos S)}{\partial w} \tag{4.3.6e}$$

$$\frac{\partial R^*}{\partial M} = \frac{\partial R^*}{\partial f} \frac{\partial f}{\partial M} = - \frac{C_S A'}{m} \left[\frac{a}{r} \right]^2 \sqrt{1-e^2}$$

$$x \left[\cos S \frac{\partial r}{\partial u} + r \frac{\partial(\cos S)}{\partial u} \right] \tag{4.3.6f}$$

These further partial derivatives are needed to form the solar radiation equations of motion:

$$\frac{\partial r}{\partial u} = \frac{r^2 e\sin f}{a(1-e^2)} \tag{4.4.7a}$$

$$\frac{\partial r}{\partial e} = - a\cos f \tag{4.4.7b}$$

$$\frac{\partial f}{\partial e} = \frac{\partial u}{\partial e} = \left[\frac{a}{r} + \frac{1}{1-e^2} \right] \sin f \tag{4.4.7c}$$

$$\frac{\partial \cos S}{\partial i} = C(\sin i \, \sin\Omega \, \sin u)$$

$$A(-\sin i \, \cos\Omega \, \sin u) + B(\cos i \, \sin u) \tag{4.4.7d}$$

$$\frac{\partial \cos S}{\partial \Omega} = C(-\cos\Omega \cos u - \cos i \cos\Omega \sin u)$$

$$+ A(-\cos\Omega \cos u - \cos i \sin\Omega \sin u) \qquad (4.4.7e)$$

$$\frac{\partial \cos S}{\partial u} = C(-\cos\Omega \cos u - \cos i \sin\Omega \cos u)$$

$$+ A(-\sin\Omega \sin u + \cos i \cos\Omega \cos u) + B(\sin i \cos u), \qquad (4.1.7f)$$

where the partial derivatives below have been used
interchangeably. (See the atmospheric drag section.)

$$\frac{\partial}{\partial f} = \frac{\partial}{\partial w} = \frac{\partial}{\partial u}$$

The new orbital equations from Equs. (4.1.6) are

$$\frac{da}{dt} = \frac{\pi 2}{na} \left[\frac{a}{r} \right]^2 (1-e^2) \cos S \left[\frac{\partial r}{\partial u} + r \frac{\partial(\cos S)}{\partial u} \right] \qquad (4.4.8a)$$

$$\frac{dh}{dt} = \frac{\pi}{na^2\sqrt{1-e^2}} (\sin u(2+k\cos u+h\sin u)+h)r \frac{\partial(\cos S)}{\partial u}$$

$$- \frac{\pi\sqrt{1-e^2}}{na} \cos u \cos S - \frac{\pi k \cot i}{na^2\sqrt{1-e^2}} r \frac{\partial(\cos S)}{\partial i} \qquad (4.4.8b)$$

$$\frac{di}{dt} = \frac{\pi\cot i}{na^2\sqrt{1-e^2}} r \frac{\partial(\cos S)}{\partial u} - \frac{\pi}{na^2 \sin i \sqrt{1-e^2}} \frac{\partial(\cos S)}{\partial \Omega} \qquad (4.4.8c)$$

$$\frac{dk}{dt} = \frac{\pi}{na^2\sqrt{1-e^2}} (\cos u(2+k\cos u+h\sin u)+k)r \frac{\partial(\cos S)}{\partial u}$$

53

$$+ \frac{\pi_Y \sqrt{1-e^2}}{na} \cos u \cos S - \frac{\pi h \cot i}{na^2 \sqrt{1-e^2}} \; r \; \frac{\partial(\cos S)}{\partial i} \qquad (4.4.8d)$$

$$\frac{d\Omega}{dt} = \frac{\pi}{na^2 \sqrt{1-e^2}} \; r \; \sin i \; \frac{\partial(\cos S)}{\partial i} \qquad (4.4.8e)$$

$$\frac{d\mathcal{L}_N}{dt} = \frac{\pi \beta'}{S_0 na^2 \sqrt{1-e^2}} \, (2+k\cos u+h\sin u)(k\sin u - h\cos u) r \; \frac{\partial(\cos S)}{\partial u}$$

$$- \frac{\pi}{S_0 na^2}\left[a\beta'\sqrt{1-e^2} \; (k\cos u+h\sin u)+2r \right] \cos S$$

$$+ \frac{\pi}{S_0 na^2 \sqrt{1-e^2}}\left[\frac{S_0 - \cos i}{\sin i} \right] r \; \frac{\partial(\cos S)}{\partial i} + \frac{n}{S_0} - \frac{d\theta_g}{dt} \qquad (4.4.8f)$$

where $\pi = \dfrac{-C_s A'}{m}$.

Occultation

As the satellite orbits Mars, it will periodically swing behind the planet such that the Sun, and thus its radiation, is blocked or occulted. As a result, we must calculate this region of solar occultation, called g(u).

Consider the right handed coordinate system (S_1, S_2, S_3) whose origin is the center of Mars. The axis S_1 will point

at the sun, axis S_3 will be normal to the plane of the equator, and S_2 will be placed so as to complete the right handed system as in Figure 4.1 below.

Under this system, the conditions for occultation are:

$$S_1 < 0 \quad \text{and} \quad S_2{}^2 + S_3{}^2 \le R_p{}^2, \qquad (4.4.9)$$

where R_p= radius of Mars plus atmospheric altitude blockage. Equation (4.4.9) may be rewritten using

$$r^2 = S_1{}^2 + S_2{}^2 + S_3{}^2$$

to become

$$r^2 - S_1{}^2 \le R_p{}^2 \quad \text{or} \quad S_1 \le - \sqrt{r^2 - R_p{}^2}. \qquad (4.4.10)$$

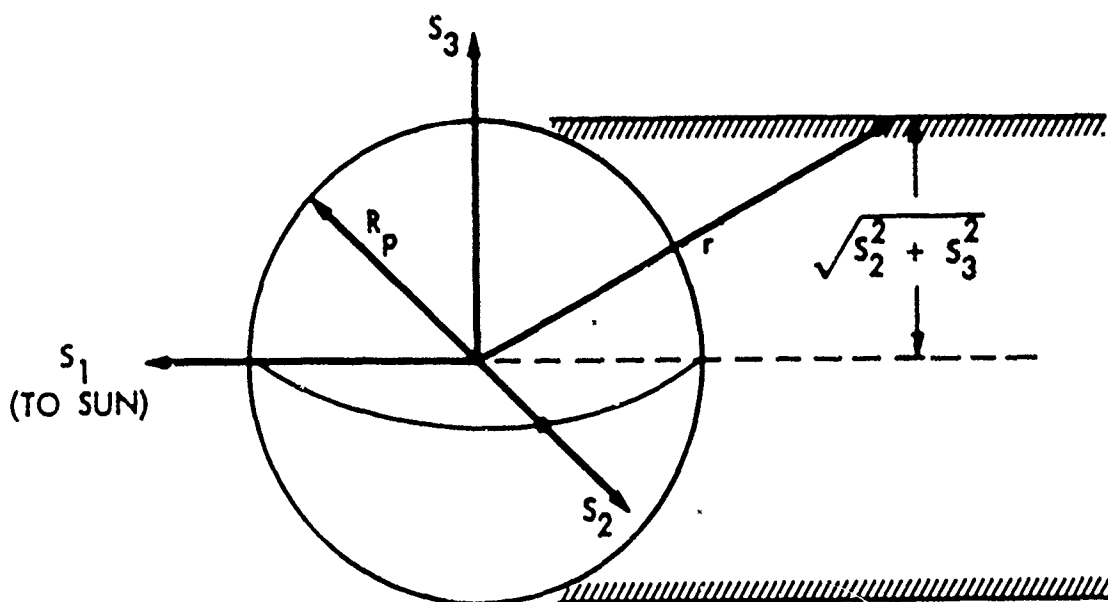This equation requires that S_1 always remain more negative as the condition for occultation.

Figure 4.1: Occultation Geometry

Assume the orbital elements of the spacecraft are known and the right ascension (α) and the declination (δ) of the viewed object are known in the same coordinate system. The cartesian position of the spacecraft in standard notation is given by

$$x_1 = r(\cos\Omega\, \cos u - \cos i\, \sin\Omega\, \sin u) \qquad (4.4.11a)$$

$$x_2 = r(\sin\Omega\, \cos u + \cos i\, \cos\Omega\, \sin u) \qquad (4.4.11b)$$

$$x_3 = r\, \sin i\, \sin u, \qquad (4.4.11c)$$

where $u = w + f$. In order to express the cartesian coordinates relative to the S_i - coordinate system, two rotations are performed:

$$
\begin{bmatrix} S_1 \\ S_2 \\ S_3 \end{bmatrix} =
\begin{bmatrix} \cos(-\delta) & 0 & -\sin(-\delta) \\ 0 & 1 & 0 \\ \sin(-\delta) & 0 & \cos(-\delta) \end{bmatrix}
\begin{bmatrix} \cos\alpha & \sin\alpha & 0 \\ -\sin\alpha & \cos\alpha & 0 \\ 0 & 0 & 1 \end{bmatrix}
\begin{bmatrix} x_1 \\ x_2 \\ x_3 \end{bmatrix}
$$

$$
\begin{bmatrix} S_1 \\ S_2 \\ S_3 \end{bmatrix} =
\begin{bmatrix} \cos(\delta)\cos\alpha & \cos(\delta)\sin\alpha & \sin\alpha \\ -\sin\alpha & \cos\alpha & 0 \\ -\sin(\delta)\cos\alpha & -\sin(\delta)\sin\alpha & \cos(\delta) \end{bmatrix}
\begin{bmatrix} x_1 \\ x_2 \\ x_3 \end{bmatrix} \qquad (4.4.12)
$$

This is now used in equation (4.4.11) to obtain

$$S_1 = (\cos\delta\cos\alpha)x_1 + (\cos\delta\sin\alpha)x_2 + (\sin\delta)x_3 \leq -\sqrt{r^2 - R_p^2} \qquad (4.4.13)$$

$$= A\, x_1 + B\, x_2 + C\, x_3 \leq -\sqrt{r^2 - R_p^2},$$

where the variables A, B, C were used earlier. Substituting for the cartesian coordinates changes the equation to

56

$$S_1 = rC(\cos\Omega \cos u - \cos i \sin\Omega \sin u)$$

$$+ rA(\sin\Omega \cos u + \cos i \cos\Omega \sin u)$$

$$+ rB(\sin i \sin u) \le - \sqrt{r^2 - R_p^2} \, . \qquad (4.4.14)$$

Redefine the coefficients as follows:

$$F = C\cos\Omega + A\sin\Omega \qquad\qquad (4.4.15a)$$

$$G = \cos i(A\cos\Omega - C\sin\Omega) + B\sin i \qquad (4.4.15b)$$

$$H = \sqrt{1 - (R_p/r)^2} \qquad\qquad (4.4.15c)$$

Finally, substitution makes the occultation condition

$$g(u) = F\cos u + G\sin u + H(u) \le 0. \qquad (4.4.16)$$

The occultation condition has three restrictions. First, $g(u)$ depends on $\cos u$ and $\sin u$, causing it to be periodic with period $2PI = 2 \times 3.14159\ldots$. Next, $g(u)$ also depends on $H(u)$, implying the minimum of $g(u)$ may not be zero. Finally, when $g(u)$ is at a minimum with $u = u_{min}$ and is negative the satellite's orbit is occulted at least part of the time from the Sun. Therefore, to check occultation, one must find the minimum of $g(u)$, which could be accomplished by solving for the roots of the derivative of $g(u)$.

Atmospheric Drag Model

The following model applies to both models of the Martian atmosphere developed earlier. Those models calculate the atmospheric mass density, μ, to be used in conjunction with this drag model.

The force, D, per unit mass due to atmospheric drag is given by (48:81):

$$D = \frac{C_d \mu A v^2}{2m} , \qquad\qquad (4.5.1)$$

where D = drag

     m = mass

     C_d = drag coefficient

     μ = atmospheric density

     A = effective spacecraft area for drag

     v = satellite velocity.

Using the notation of (30:81), the drag acts opposite to the velocity of the satellite and may be written in vector notation as

$$\mathbf{D} = - D \, \hat{u}_\Gamma, \qquad\qquad (4.5.2)$$

where $\hat{u}_\Gamma$ is the unit vector along the tangent in the direction of satellite motion.

The drag force is broken down into two components: radial and transverse components of the satellite's

velocity. These are defined by a radial unit vector, $\hat{u}_r$, along the position vector $\underline{r}$ of the satellite, and the transverse unit vector, $\hat{u}_\theta$, perpendicular to $\underline{r}$ and forming an acute angle with the velocity vector $\underline{v}$ in the orbital plane. Writing the drag using these unit vectors yields

$$\underline{D} = F_r\,\hat{u}_r + F_\theta\,\hat{u}_\theta. \qquad (4.5.3)$$

To determine these drag components, F_r and F_θ, first define the velocity vector as

$$\underline{v} = v\,\hat{u}_r = \dot{r}\,\hat{u}_r + r\dot{f}\,\hat{u}_\theta. \qquad (4.5.4)$$

This makes the drag components

$$F_r = \underline{D} \cdot \hat{u}_r = -D(\hat{u}_r \cdot \hat{u}_r) = -\frac{\dot{r}}{v}D \qquad (4.5.5)$$

$$F_\theta = \underline{D} \cdot \hat{u}_\theta = -D(\hat{u}_r \cdot \hat{u}_\theta) = -\frac{r\dot{f}}{v}D \qquad (4.5.6)$$

Making use of these standard orbital relationships (12):

$$r = \frac{a(1-e^2)}{1+e\cos f} \qquad (4.5.7a)$$

$$\dot{r} = \frac{k\,e\sin f\,\sqrt{M}}{\sqrt{a(1-e^2)}} \qquad (4.5.7b)$$

$$r^2\dot{f} = h = \sqrt{k^2 M a(1-e^2)} \qquad (4.5.7c)$$

$$r\dot{f} = \frac{k(1+e\cos f)\sqrt{M}}{\sqrt{a(1-e^2)}} \qquad (4.5.7d)$$

$$v = \frac{k_r M \, \dot{r}(1+e^2+2e\cos f)}{\dot{r}\,a(1-e^2)}, \qquad (4.5.7e)$$

by substitution into equations (4.5.5) and (4.1.6) yields

$$F_r = \frac{-e\sin f \; D}{\dot{r}(1+e^2+2e\cos f)} \qquad (4.5.8)$$

$$F_\theta = \frac{-(1+e\cos f) \; D}{\dot{r}(1+e^2+2e\cos f)}. \qquad (4.5.9)$$

Now place these magnitudes, F_r and F_θ, into the perifocal orbital reference frame specified by a unit vector in the direction of perihelion, $\hat{P}$, and a unit vector $f=90°$ in the direction of motion from P, called $\hat{Q}$, making the drag

$$\underline{D} = F_r \hat{u}_r + F_\theta \hat{u}_\theta = (F_r\cos f - F_\theta\sin f)\hat{P} + (F_r\sin f + F_\theta\cos f)\hat{Q} \qquad (4.5.10)$$

and making the position vector

$$\underline{r} = (r\cos f)\hat{P} + (r\sin f)\hat{Q}$$

$$= \frac{a(1-e^2)\cos f}{1+e\cos f}\,\hat{P} + \frac{a(1-e^2)}{(1+e\cos f)\sin f}\,\hat{Q}. \qquad (4.5.11)$$

The last step is to calculate the partial derivatives of the perturbation due to atmospheric drag using the following equation:

$$\frac{\partial R}{\partial z_i} = \frac{\partial R}{\partial r}\frac{\partial r}{\partial z_i} = E \cdot \frac{\partial r}{\partial z_i}, \qquad (4.5.12)$$

where the z_i represents the six classical orbital elements. The resulting partial derivatives are:

$$\frac{\partial R}{\partial a} = F_r \frac{r}{a} \qquad\qquad (1.5.13a)$$

$$\frac{\partial R}{\partial e} = - F_r\, a\cos f + F_\theta\, a\sin f \left[1 + \frac{r}{a(1-e^2)} \right] \qquad\qquad (4.5.13b)$$

$$\frac{\partial R}{\partial M} = F_r \frac{ea \sin f}{\sqrt{(1-e^2)}} + F_\theta\, a^2 \frac{\sqrt{1-e^2}}{r} \qquad\qquad (4.5.13c)$$

$$\frac{\partial R}{\partial \Omega} = F_\theta\, r \cos i \qquad\qquad (4.5.13d)$$

$$\frac{\partial R}{\partial w} = F_\theta\, r \qquad\qquad (4.5.13e)$$

$$\frac{\partial R}{\partial i} = 0 \qquad\qquad (4.5.13f)$$

Now insert these into Lagrange's Planetary Equations in order to find the orbital equations of motion in the classical orbital element set that are due to drag:

$$\frac{da}{dt} = - \frac{C_d A}{m} \mu n a^2 \left[\frac{1+e^2 + 2e\cos f}{1-e^2} \right]^{3/2} \qquad\qquad (4.5.14a)$$

$$\frac{de}{dt} = - \frac{C_d A}{m} \mu n a\,(e+\cos f) \left[\frac{1+e^2 + 2e\cos f}{1-e^2} \right]^{1/2} \qquad\qquad (4.5.14b)$$

$$\frac{dw}{dt} = - \frac{C_d A}{m} \mu n a\, \frac{\sin f}{e} \left[\frac{1+e^2 + 2e\cos f}{1-e^2} \right]^{1/2} \qquad\qquad (4.5.14c)$$

61

$$\frac{di}{dt} = 0 \qquad\qquad (4.5.14d)$$

$$\frac{d\Omega}{dt} = 0 \qquad\qquad (4.5.14e)$$

$$\frac{dM}{dt} = -\frac{C_dA}{m}\,\mu na\,\frac{\sin f}{e}\,\frac{(1+e^2+e\cos f)}{(1+e\cos f)}\,\sqrt{1+e^2 2e\cos f} \qquad (4.5.14f)$$

Convert these equations into the modified orbital element set and substitute to get:

$$\frac{dh}{dt} = \frac{h}{e}\left[-\frac{C_dA}{m}\,\mu na\,(e+\cos f)\left[\frac{1+e^2+2e\cos f}{1-e^2}\right]^{1/2}\right]$$

$$+\, k\left[-\frac{C_dA}{m}\,\mu na\,\frac{\sin f}{e}\left[\frac{1+e^2+2e\cos f}{1-e^2}\right]^{1/2}\right]$$

$$= -\frac{C_dA}{m}\,\mu na\,(h+\sin u)\left[\frac{1+e^2+2e\cos f}{1-e^2}\right]^{1/2} \qquad (4.5.15a)$$

$$\frac{dk}{dt} = \frac{k}{e}\left[-\frac{C_dA}{m}\,\mu na\,(e+\cos f)\left[\frac{1+e^2+2e\cos f}{1-e^2}\right]^{1/2}\right]$$

$$-\, h\left[-\frac{C_dA}{m}\,\mu na\,\frac{\sin f}{e}\left[\frac{1+e^2+2e\cos f}{1-e^2}\right]^{1/2}\right]$$

$$= -\frac{C_dA}{m}\,\mu na\,(k+\cos u)\left[\frac{1+e^2+2e\cos f}{1-e^2}\right]^{1/2} \qquad (4.5.15b)$$

$$\frac{dL_N}{dt} = \frac{1}{S_0}\left[-\frac{C_d A}{m}\,\mu n a\,\frac{\sin f}{e}\,\frac{(1+e^2+e\cos f)\sqrt{1+e^2 2\cos f}}{(1+e\cos f)} \right.$$

$$\left. -\frac{C_d A}{m}\,\mu n a\,\frac{\sin f}{e}\left[\frac{1+e^2+2e\cos f}{1-e^2}\right]^{1/2} \right]$$

$$= -\frac{1}{S_0}\frac{C_d A}{m}\,\mu n a\,e\sin f\left[\beta' - \frac{r}{a\sqrt{1-e^2}}\right]\sqrt{1+e^2 2\cos f}, \quad (4.5.15c)$$

where $e\cos f = k\cos u + h\sin u$, $e\sin f = k\sin u - h\cos u$, $u = w + f$.

Now that we have the drag equations of motion, we need to apply the Method of Averaging to eliminate fast variables as shown in reference (28:3-26). Retain only the averaged effects of atmospheric drag over one period in order to approximate long term orbits. The averaged rate is given in (28:3-26) as

$$\overline{\frac{d\Gamma}{dt}} = \frac{1}{p}\int^p \frac{d\Gamma}{dt}\,dt, \quad (4.5.16)$$

where $\Gamma = a, h, k, L_N$.

Time is related to the true anomaly, f, by

$$dt = \frac{r^2\,df}{na^2\sqrt{(1-e^2)}}. \quad (4.5.17)$$

Substitution into (4.5.16) with a period of 2PI yields

$$\overline{\frac{d\Gamma}{dt}} = \frac{n}{2PI}\int_0^{2PI}\frac{d\Gamma}{dt}\frac{r^2 df}{na^2\sqrt{(1-e^2)}}. \quad (4.5.18)$$

63

Over one period, the Argument of Periapsis, w, will have only a small change. As a result, we can write

$$df = dw + du \approx du \quad \text{or} \quad df = du \qquad (4.5.19)$$

Substituting the orbital equations derived above into the integral averaging equation yields:

$$\overline{\frac{da}{dt}} = \frac{\Phi}{1-e^2} \int_0^{2PI} \mu\left[\frac{r}{a}\right]^2 [1+e^2+2(k\cos u + h\sin u)]^{3/2} du \qquad (4.5.20a)$$

$$\overline{\frac{dh}{dt}} = \Phi \int_0^{2PI} \mu\left[\frac{r}{a}\right]^2 (h+\sin u)$$

$$\times [1+e^2+2(k\cos u + h\sin u)]^{1/2} du \qquad (4.5.20b)$$

$$\overline{\frac{di}{dt}} = 0 \qquad (4.5.20c)$$

$$\overline{\frac{dk}{dt}} = \Phi \int_0^{2PI} \mu\left[\frac{r}{a}\right]^2 (k+\cos u)$$

$$\times [1+e^2+2(k\cos u + h\sin u)]^{1/2} du \qquad (4.5.20d)$$

$$\overline{\frac{d\Omega}{dt}} = 0 \qquad (4.5.20e)$$

$$\overline{\frac{dL_N}{dt}} = \Phi \int_0^{2PI} \mu\left[\frac{r}{a}\right]^2 (k\sin u - h\cos u)[1+e^2+2(k\cos u + h\sin u)]^{1/2}$$

$$\times \left[\beta' - \frac{r}{a\sqrt{(1-e^2)}} \right] du, \qquad (4.5.20f)$$

64

where $\Phi = \dfrac{-C_d A}{m} \dfrac{na^2}{1-e^2} \dfrac{1}{2PI}$,

and μ is calculated using one of the two Martian atmosphere models that were explained in section III.

Third Body Disturbing Potential (Solar Gravity)

The derivation of these equations is quite extensive. Further information may be found in reference (28) and other works. The following equations are those necessary for this model.

The averaged third body disturbing potential R' is given as follows:

$$R' = \frac{\mu'}{a'} \sum_{n=2}^{\infty} \left[\frac{a}{a'} \right]^n \sum_{m=0}^{n} K_{nm} \sum_{p=0}^{n} \left[F_{nmp}(i) \, H_{npq}(e) \right]$$

$$\times \sum_{h=0}^{n} F_{nmh}(i') \sum_{j=-\infty}^{\infty} \left[G_{nhj}(e') \cos(\phi) \right] , \qquad (4.6.1)$$

where $\quad \phi = -qw - (n-2h)w' - (n-2h+j)M' + m(\Omega-\Omega')$, (4.6.2)

$$K_{nm} = \frac{2(n-m)!}{(n+m)!}, \; K_{n0} = 1, \; q = 2p - n,$$

H is defined later, and the variables with the superscript ' refer to those of the disturbing body.

Rewriting the disturbing potential R' using definitions from (28:3-21) obtains:

$$R' = \frac{\mu'}{a'} \sum_{n=2}^{\infty} \left[\frac{a}{a'} \right]^n \sum_{m=0}^{n} K_{nm} \sum_{p=0}^{n} \left[F_{nmp}(i) \; H'_{npq}(e) \right]$$

$$\times \sum_{h=0}^{n} F_{nmh}(i') \sum_{j=-\infty}^{\infty} \left[G_{nhj}(e') \; S_{nmqhj} \right] . \qquad (4.6.3)$$

The function $H_{np(2p-n)}$ is defined as

$$H_{np(2p-n)} =$$

$$\frac{(-\beta)^{n-2p'}}{(1+\beta^2)^{n+1}} \left[\begin{matrix} 2n+1-2p' \\ n-2p' \end{matrix} \right] \sum_{k} \left[\begin{matrix} n+1 \\ k \end{matrix} \right] \left[\begin{matrix} 2p'+1 \\ k \end{matrix} \right] \frac{\beta^{2k}}{\left[\begin{matrix} n-2p'+k \\ k \end{matrix} \right]}, \qquad (4.6.4)$$

where $\begin{cases} p' = p, & p \leq n/2 \\ p' = n-p, & p \geq n/2 \end{cases}$

k = all integers where binomial coefficients are nonzero.

Therefore, the partial derivatives of R' in the modified orbital element set are:

$$\frac{\partial R'}{\partial a} = \mu' \frac{1}{a'} \frac{1}{a} \sum_{n=2}^{\infty} n \left[\frac{a}{a'} \right]^n \sum_{m=0}^{n} K_{nm} \sum_{p=0}^{n} F_{nmp}(i) \; H'_{npq}(e)$$

$$\times \sum_{h=0}^{n} F_{nmh}(i') \sum_{j=-\infty}^{\infty} G_{nhj}(e') \; S_{nmqhj} \qquad (4.6.5a)$$

.

$$\frac{\partial R'}{\partial h} = \mu' \sum_{n=2}^{\infty} \left[\frac{a}{a'}\right]^n \sum_{m=0}^{n} K_{nm} \sum_{p=0}^{n} F_{nmp}(i) \left[\frac{h}{e} \frac{dH'_{npq}(e)}{de} \right.$$

$$\times \sum_{h=0}^{n} F_{nmh}(i') \sum_{j=-\infty}^{\infty} G_{nhj}(e') S_{nmqhj}$$

$$\left. + H'_{npq}(e) \sum_{h=0}^{n} F_{nmh}(i') \sum_{j=-\infty}^{\infty} G_{nhj}(e') \frac{\partial S_{nmqhj}}{\partial h} \right] \qquad (4.6.5b)$$

$$\frac{\partial R'}{\partial i} = \mu' \sum_{n=2}^{\infty} \left[\frac{a}{a'}\right]^n \sum_{m=0}^{n} K_{nm} \sum_{p=0}^{n} \frac{dF_{nmp}(i)}{di} H'_{npq}(e)$$

$$\times \sum_{h=0}^{n} F_{nmh}(i') \sum_{j=-\infty}^{\infty} G_{nhj}(e') S_{nmqhj} \qquad (4.6.5c)$$

$$\frac{\partial R'}{\partial k} = \mu' \sum_{n=2}^{\infty} \left[\frac{a}{a'}\right]^n \sum_{m=0}^{n} K_{nm} \sum_{p=0}^{n} F_{nmp}(i) \left[\frac{k}{e} \frac{dH'_{npq}(e)}{de} \right.$$

$$\times \sum_{h=0}^{n} F_{nmh}(i') \sum_{j=-\infty}^{\infty} G_{nhj}(e') S_{nmqhj}$$

$$\left. + H'_{npq}(e) \sum_{h=0}^{n} F_{nmh}(i') \sum_{j=-\infty}^{\infty} G_{nhj}(e') \frac{\partial S_{nmqhj}}{\partial k} \right] \qquad (4.6.5d)$$

$$\frac{\partial R'}{\partial \Omega} = \mu' \sum_{n=2}^{\infty} \left[\frac{a}{a'}\right]^n \sum_{m=0}^{n} K_{nm} \sum_{p=0}^{n} F_{nmp}(i) H'_{npq}(e)$$

$$\times \sum_{h=0}^{n} F_{nmh}(i') \sum_{j=-\infty}^{\infty} \left[G_{nhj}(e') \frac{\partial S_{nmqhj}}{\partial \Omega} \right] \qquad (4.6.5e)$$

67

$$\frac{\partial R'}{\partial L_N} = 0. \qquad\qquad (4.6.5f)$$

All that remains to be done is to substitute into the Lagrange's Planetary Equations (4.1.4) as we have done with the other disturbing potential functions, replacing R with R' to form the differential equations for the third body, the Sun. These substitutions will not be done here.

V. Approach and Results

Approach

A variety of assumptions are made in constructing the dynamic and static atmosphere models. Most of these have already been explained in the theory sections. This section will review the inputs to the computational models based on the theoretical models of the previous sections.

The Martian geopotential was modeled using only J_2 and J_3, the dominant terms representing the strong, first-order equatorial oblateness effect and significant first-order asymmetry of Mars (28:2-35) and (8:1). (See Table 5.1.) In addition, the orbital missions were chosen close to a known solar epoch and Prime Meridian (28:2-10) in order to minimize error due to the coordinate system used, namely the planet equator of epoch coordinate system for Mars. Finally, empirical data was used to choose limits for the atmosphere, both the "outer" limit and the "inner" limit.

The "outer" limit is set to 1000 km since this is where the first "heavy" ions, atomic oxygen, exist in significant concentrations (37:210). Although atomic hydrogen has been observed as high as 10,000 km, these are much "lighter" atoms and so exert far less drag. Hence, the 1000 km limit. The "inner" limit is set to 130 km based on the fact the ionosphere constituent concentration is greatest at this

altitude (21:27). In addition, the turbopause altitude (the dividing line between the denser lower atmosphere and the less dense ionosphere) is very close to this region. It may be expected that any satellite which reaches this altitude is actually beginning to enter the atmosphere proper and will shortly impact Mars due to the much thicker atmosphere.

The mean anomaly M, which is a fast variable (short term effects) is averaged out in the theoretical models. As a result, it can assume any value. For convenience, it has been chosen to be zero and kept constant. The other orbital parameters (a,e,i,Ω,w) could be varied at will. The initial values were based on data from the Viking missions (41:3979-3982), Mariner 9 (26:484), and from scientific missions to Mars (45) and (28). A representative sampling of data for possible real life missions was obtained, covering both close and far orbits as well as both near equatorial and near polar orbits.

The effects on orbital motion of using a dynamic Martian atmosphere model are demonstrated by comparing the resulting orbital element data from the dynamic model to those from the static model. The orbital parameters examined were a, e, w, and the periapsis altitude, h_p. The periapsis altitude is calculated as follows:

$$h_p = a(1-e^2)-r_m, \qquad (5.1)$$

where r_m is the reference altitude of the surface of Mars, which is calculated differently by the two atmosphere models. Both sets of data are graphed as a function of time. The Argument of Periapsis is only graphed for the first four cases in order to check for consistency with the other orbital elements and for any trends.

The satellite model requires input values for the satellite mass, the satellite drag coefficient, and the effective satellite area, which is needed for both drag and solar radiation calculations. Typical values were chosen for these variables from references (23),(28),(41),and (45). Table 5.2 lists these values.

The theoretical models were programmed using the FORTRAN programming language and combined programs both self-written and imported from (28) and (8). Each computer integration run used a step size of 5 days, unless otherwise noted, and were typically set for a two year run as that was deemed sufficient to show the desired effects on the orbit. Special attention was paid to low orbits to verify the 130 km altitude limit of the "real" Martian atmosphere.

Table 5.1:Martian Geopotential Coefficients for J_2 and J_3				
n	m	C_{nm}		S_{nm}
2	0	-0.1960387250000000E-02		0.0000000000000000E+00
3	0	-0.3063419400000000E-04		0.0000000000000000E+00

71

Table 5.2: Spacecraft Data Input Values		
Mass (kg)	:	1000
Drag Coefficient	:	2.0
Area for Drag (km^2)	:	10.0E-6
Area for Solar Radiation Pressure (km^2)	:	20.0E-6
Solar Radiation Pressure Constant($kg/kmsec^2$):		1.95E-3

Table 5.3: Other Necessary Input Data	
Prime Meridion (')	333.55971
Solar Epoch	19910524 = 24 May 1991
Initial Propagation Time:	19911007 = 7 October 1991
GM_{mars} (km^3/sec^2)	4.2828287E4
Radius of Mars (km)	3397.2
Rotation of Mars ('/sec)	4.061249803E-3
Radius + Atmospheric Blockage:	Radius + 90 = 3487.2 (km)
GM_{sun} (km^3/sec^2)	0.13271244E12

Each data run involved 73 points for each parameter for each year of the data run. Hence, it was not practical to show every point in tabular form. The following data tables show the initial parameters at the time equals zero row and then a data point for each 120 days of the run for as long as the run lasted. The first two cases are shown in this

chapter in both tabular and graphical form; the other
fifteen cases are presented in Appendices A and B.

Results

The data indicate there is a difference in the orbital
motion of a satellite due to a dynamic Martian atmosphere as
compared to motion resulting from a static Martian
atmosphere. The dynamic atmosphere provides lesser drag on
the spacecraft, implying a lesser atmospheric mass density,
i.e., motion through the static atmosphere tends to spiral
the satellite into the surface of the planet more quickly
than the dynamic atmosphere.

This effect is most evident for low orbits-- orbits
only a few hundred kilometers above the surface of Mars. As
the orbital ellipse increases in size (as measured by the
length of the semimajor axis), the amount of differentiation
between the two models decreases in magnitude. For large
orbits, those on the order of tens of thousands of
kilometers in the length of the semimajor axis, the
differences are negligible. (See cases 8,10,11,3, for
example.) Furthermore, the data indicate the variation
between the two models increases with time. (See cases
1,4,14.) The larger the size of the orbit the longer the
two models remain essentially the same before beginning to
differentiate. (See cases 6,9,10,8.) Nonetheless, once the

73

differentiation begins, it increases as time goes on. In other words, the amount of variation between the two models depends on both orbital size, as measured by length of the semimajor axis, and on time. This is logical since the larger the orbit the less time the spacecraft spends in the atmosphere, resulting in less change in the orbit due to either model, and hence the lesser degree of variation between the two. Once the two trajectories have begun to vary, the orbit with the greater atmospheric drag, always the static case, will cause the spacecraft to spend a marginally longer amount of time in the atmosphere, thereby increasing the amount of variation.

Varying the inclination produces no apparent effect on the orbits. (See cases 9,14,17.) Furthermore, changing the eccentricity while keeping the other orbital elements as they were only has an impact in that higher eccentricities reduce the periapsis altitude and hence the satellite spends a greater amount of time in the atmosphere. (See cases 7,8.) As has already been mentioned, the amount of time spent in the atmosphere is the crucial determinant in variation between the two models. In addition, the various orbital parameters agree internally with each other. For example, the eccentricity for the static model will become more circular faster than the eccentricity of the dynamic case, thus indicating the greater amount of drag affecting the

74

satellite in the static case and agreeing with the decrease in periapsis altitude and semimajor axis length.

The expected beginning of the "real" atmosphere, called the lower limit previously, was at about 130 km. This has been verified. For those trajectories that "blow up," the data show that once the periapsis altitude falls below 200 km the slope of the curve increases to nearly vertical. The trajectory then continues until about 130 km ± 15 km where the numerical calculation "blows up," thus indicating that the satellite impacted the surface. (See cases 2,4.) Both models fall within this range. However, the static model reaches the "blow up" or impact point first. (See case 5, for example.)

In summary, the dynamic model exerts less drag on the spacecraft than the static model. The variation between the two models increases with both time and decreasing orbit size. Also, the orbital parameters agree with each other. Finally, the limit of the "real" atmosphere or lower limit is shown to be in the expected region, about 130 km.

However, a closer look should be taken at the difference in the atmospheric density between the two models. This difference is plotted in Fig. B.48 for a two year Case 1 input. As can be seen, the dynamic density varies in an oscillatory manner, which is expected from the confused and variable state of the Martian atmosphere. The static density varies smoothly, which is expected due to the

exponential function. However, while the dynamic density is sometimes greater than the static density, more often it is less, particularly in the latter half of the run. The static case was modeled using a reference density that was an upper bound, 6×10^{-13} kg/m^3. For comparison purposes, choose another typical value from the empirical data for the height region of the orbits; keeping the same order of magnitude but reducing the multiplying factor from 6 to 3.1 modifies the relationship between the two models (Figures B.49 to B.52). As can be seen, the two models are now much closer to each other. Nonetheless, over a long term period, for this case exceeding one year's run, the basic difference persists: the static case will impact Mars first since the static density is still higher over the longer time period (see Fig. B.52). However, if the static reference density is further decreased, the lifetime of the static satellite will continue to improve relative to the dynamic satellite. But, until empirical data provides a better agreed-upon value for the reference density, the best that can be said is that the dynamic model exerts less drag over long term orbits.

Table 5.4: Case 1 Data				
Dynamic Data		(5 year run)		
t	a(km)	e	w(°)	h_p(km)
0	3758.31700	.00704800	270.00000	334.62838
120	3757.92726	.00704882	269.90415	334.23831
240	3756.89135	.00706625	269.85892	333.14423
360	3755.90921	.00707127	269.93376	332.15018
480	3755.63841	.00705635	269.99388	331.93731
600	3755.52698	.00704709	269.92522	331.86143
720	3755.42520	.00705840	269.85957	331.71790
840	3755.16883	.00707317	269.93145	331.40790
960	3754.60034	.00706864	270.00108	330.86043
1080	3754.20377	.00705504	269.93150	330.51773
1200	3754.12023	.00705701	269.85583	330.42736
1380	3754.06216	.00706860	269.96377	330.32618
1500	3753.96388	.00706271	270.01380	330.25074
1620	3753.66256	.00706013	269.92361	329.96123
1740	3753.39308	.00706717	269.84392	329.66720
1800	3753.35281	.00707068	269.86774	329.61405
Case 1 Continued (Static Data)				
0	3758.31700	.00704800	270.00000	334.62838
120	3756.87252	.00706130	269.98956	333.14409
240	3755.36809	.00707024	270.03615	331.61674
360	3753.79840	.00706500	270.04730	330.07780
480	3752.15764	.00706019	270.01820	328.46670
600	3750.43952	.00706589	270.00703	326.73934

77

840	3746.73809	.00708106	270.08833	323.00720
960	3744.73504	.00708230	270.06910	321.01371
1080	3742.61448	.00708324	270.02668	318.90464
1200	3740.36238	.00708801	270.04725	316.55067
1320	3737.96176	.00709282	270.10459	314.24908
1440	3735.39101	.00709669	270.13623	311.68210
1560	3732.62321	.00710448	270.12866	308.90486
1680	3729.62608	.00711197	270.09812	305.90169
1800	3726.35802	.00711701	270.11560	302.63749

Table 5.5: Case 2 Data

Dynamic Data

t	a(km)	e	$w(°)$	$h_p(km)$
0	3697.20000	.00250000	270.00000	290.75700
120	3695.72641	.00528445	229.39501	278.99653
240	3690.66345	.00876479	237.82332	261.11556
360	3684.48252	.01097531	252.23568	246.84420
480	3682.96559	.01184056	267.35057	242.15722
600	3682.27339	.01142396	282.36780	243.00723
720	3681.66228	.00982776	296.37131	248.27977

Case 2 Continued (Static Data)

0	3697.20000	.00250000	270.00000	290.75700
120	3687.99932	.00518093	236.25771	271.69205
240	3675.91680	.00763305	243.72583	250.65834
360	3658.04837	.00862316	254.07183	229.30444
480	3622.10189	.00824591	263.24949	195.03439

Fig. 5.1: Periapsis Altitude vs. Time (Case 1)

Dynamic Model
Static Model
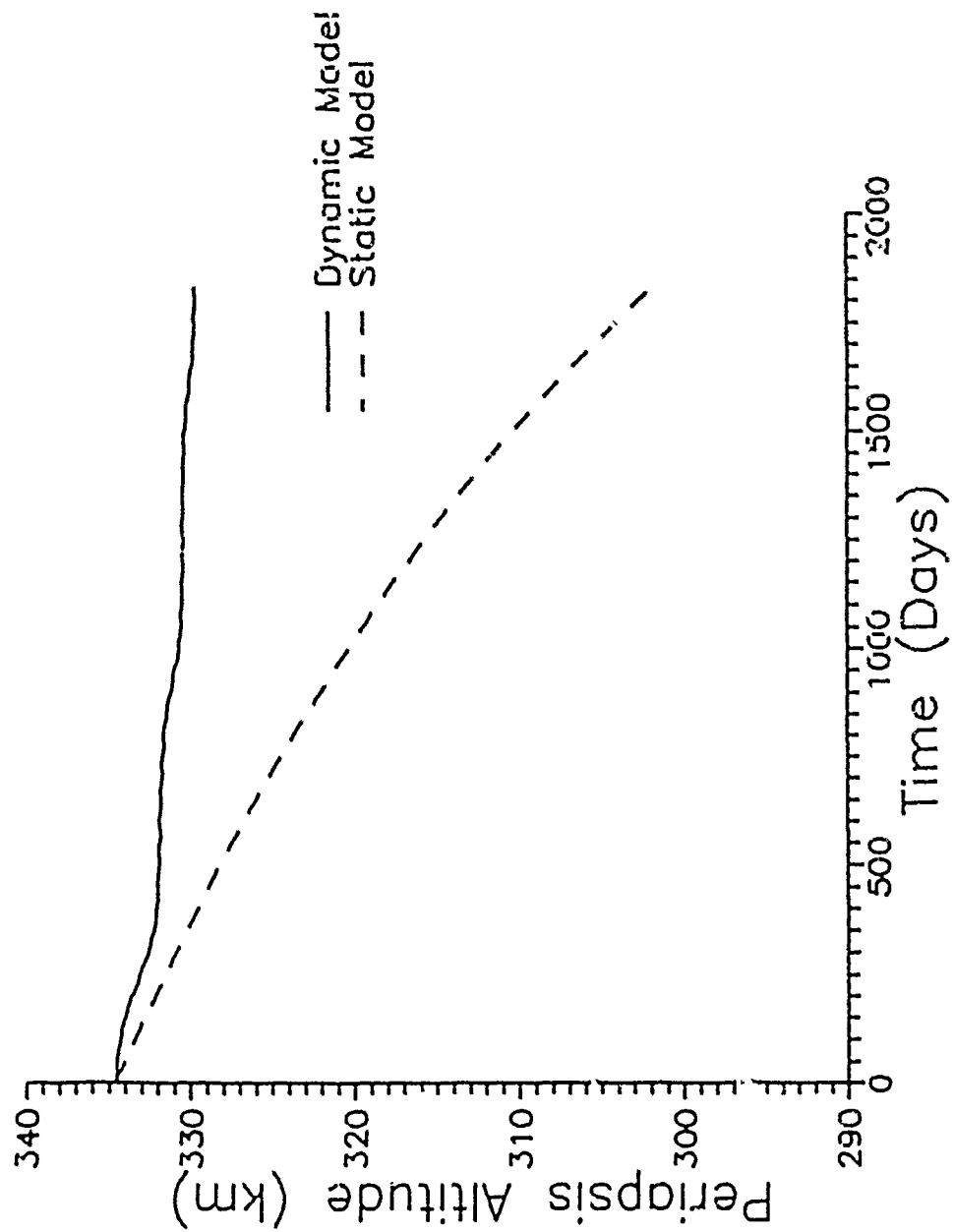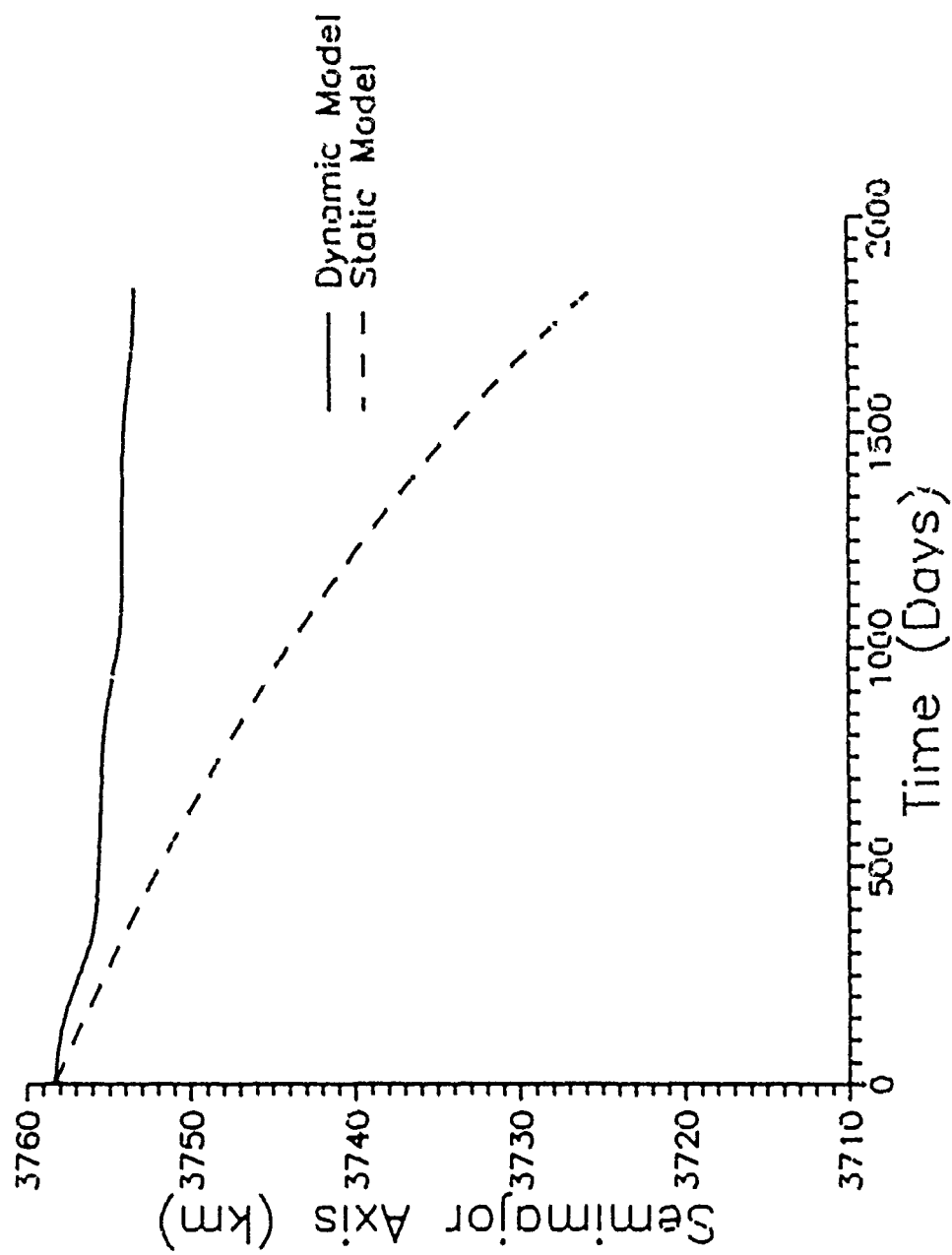
Fig. 5.2: Semimajor Axis vs. Time (Case 1)

80
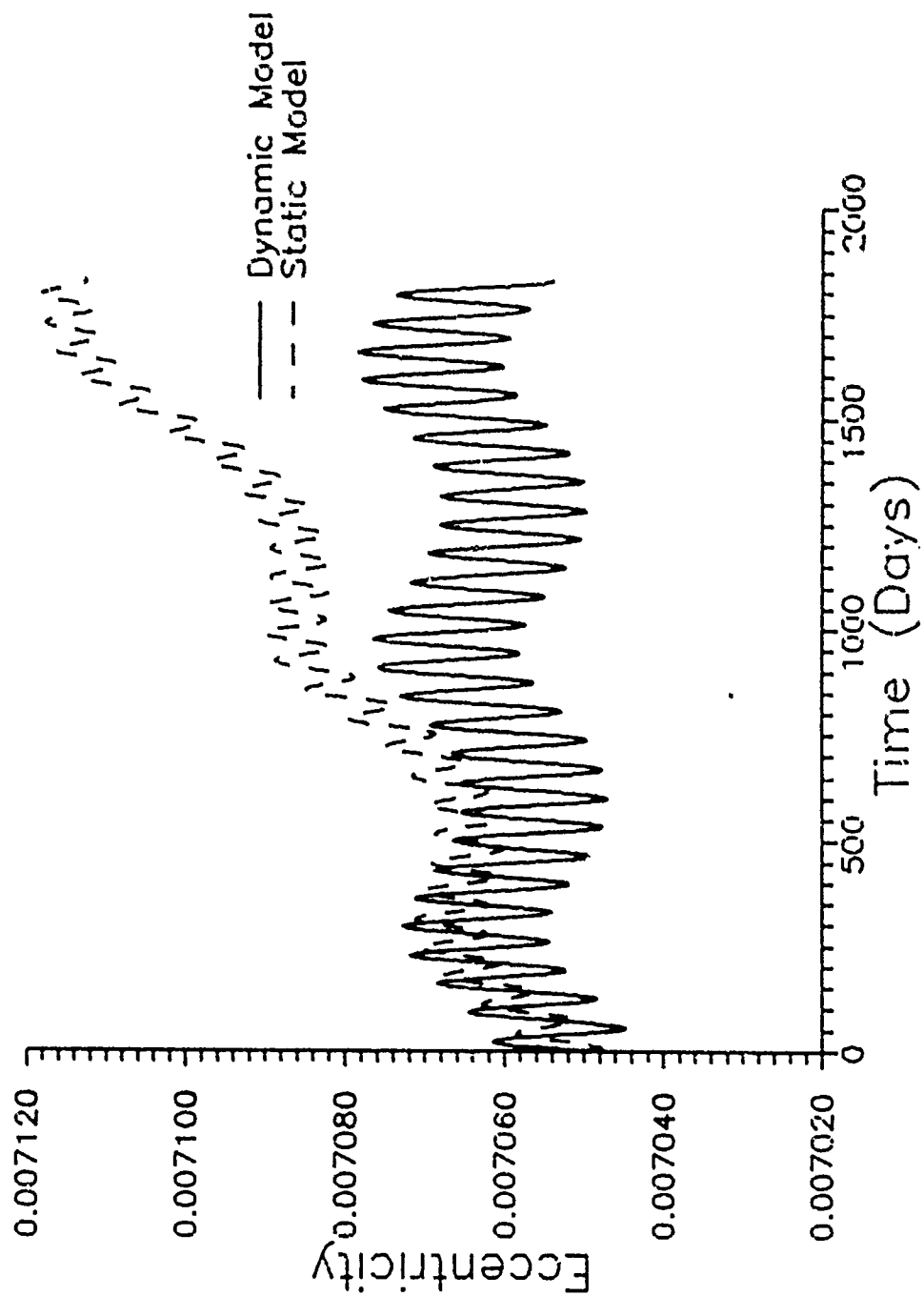
Fig. 5.3: Eccentricity vs. Time (Case 1)

81

Fig. 5.4: Argument of Periapsis vs. Time (Case 1)

Dynamic Model
Static Model

Time (Days)

Argument of Periapsis (Deg)

270.200
270.100
270.000
269.900
269.800
269.700

0
500
1000
1500
2000
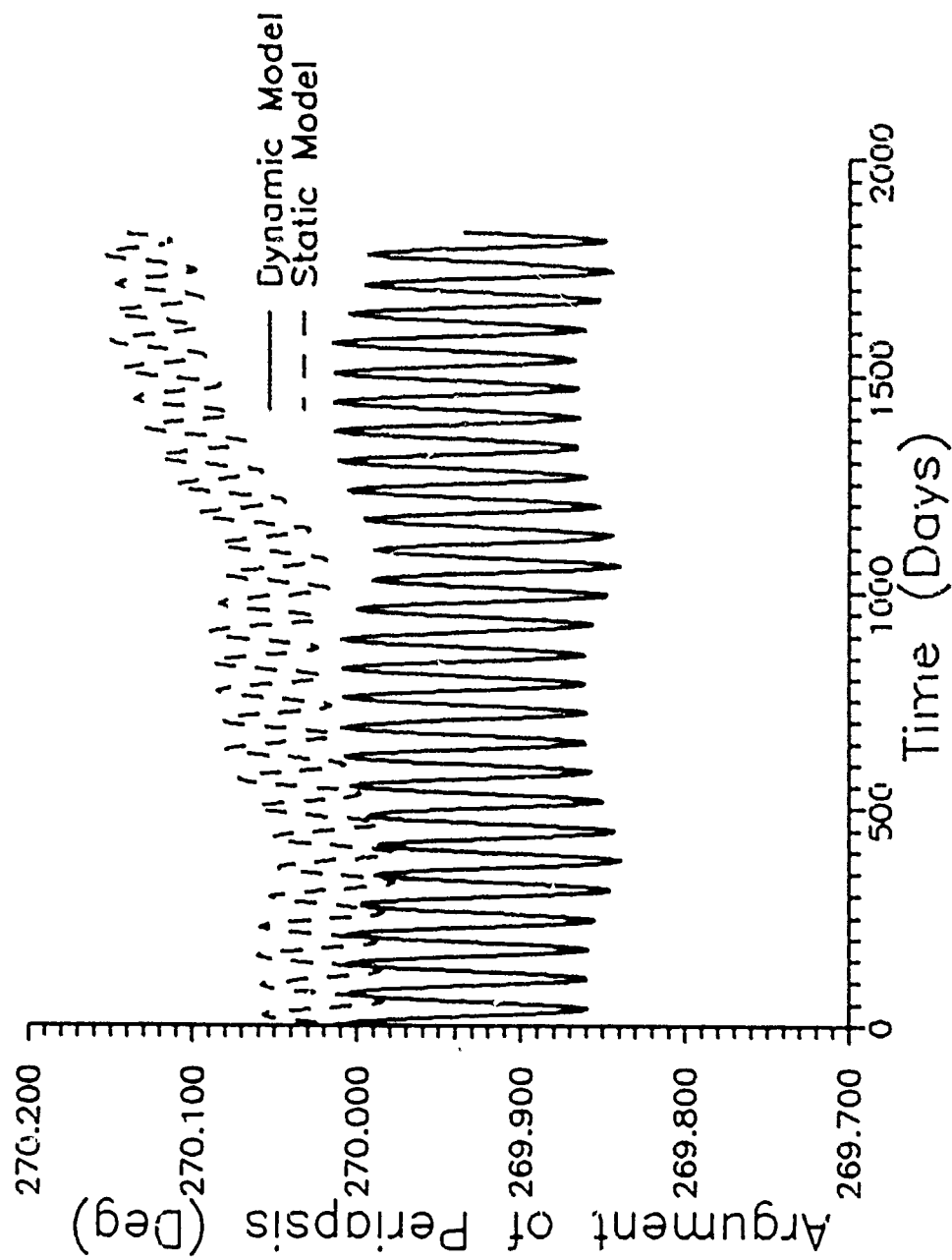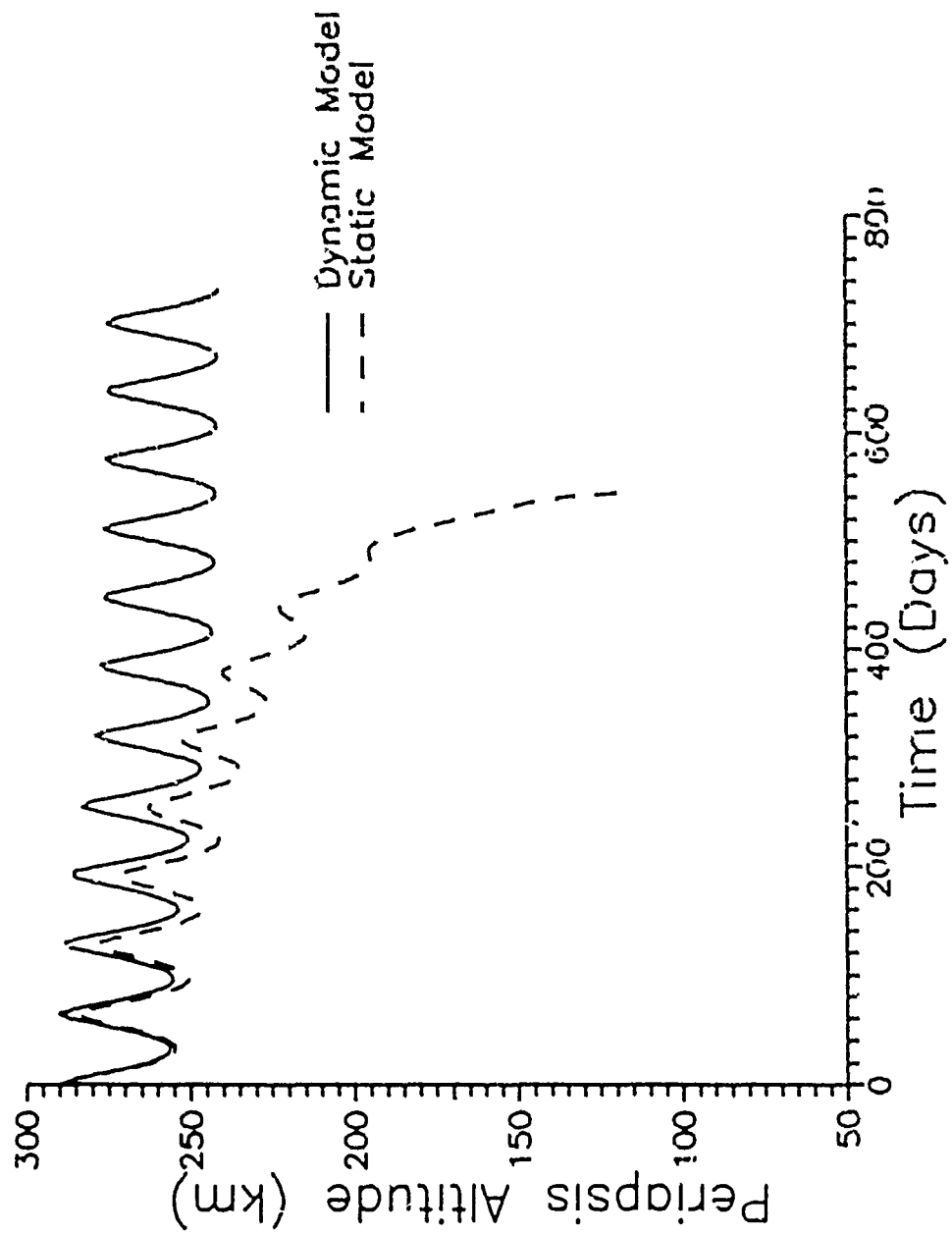
Fig. 5.5: Periapsis Altitude vs. Time (Case 2)

83
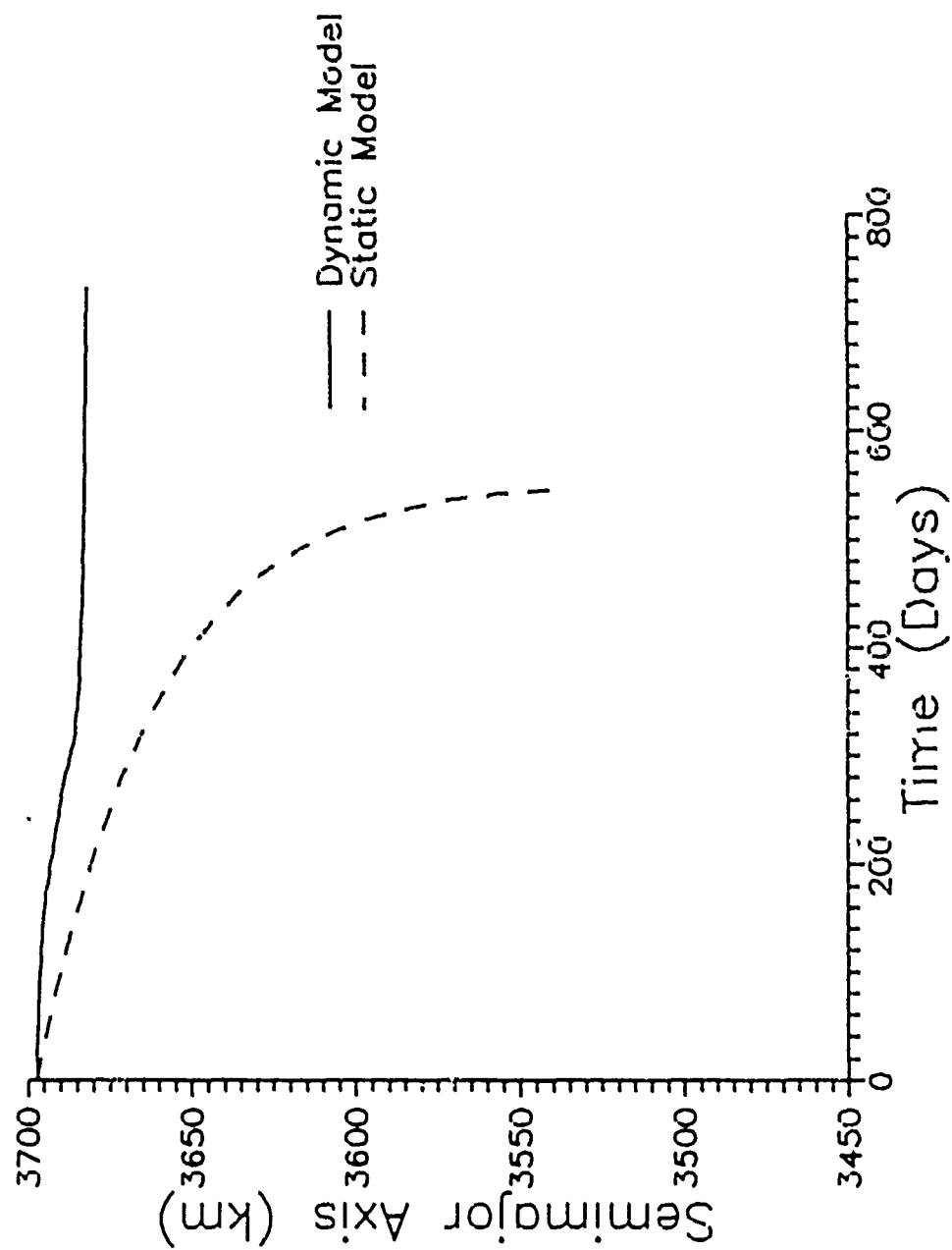
Fig. 5.6: Semimajor Axis vs. Time (Case 2)
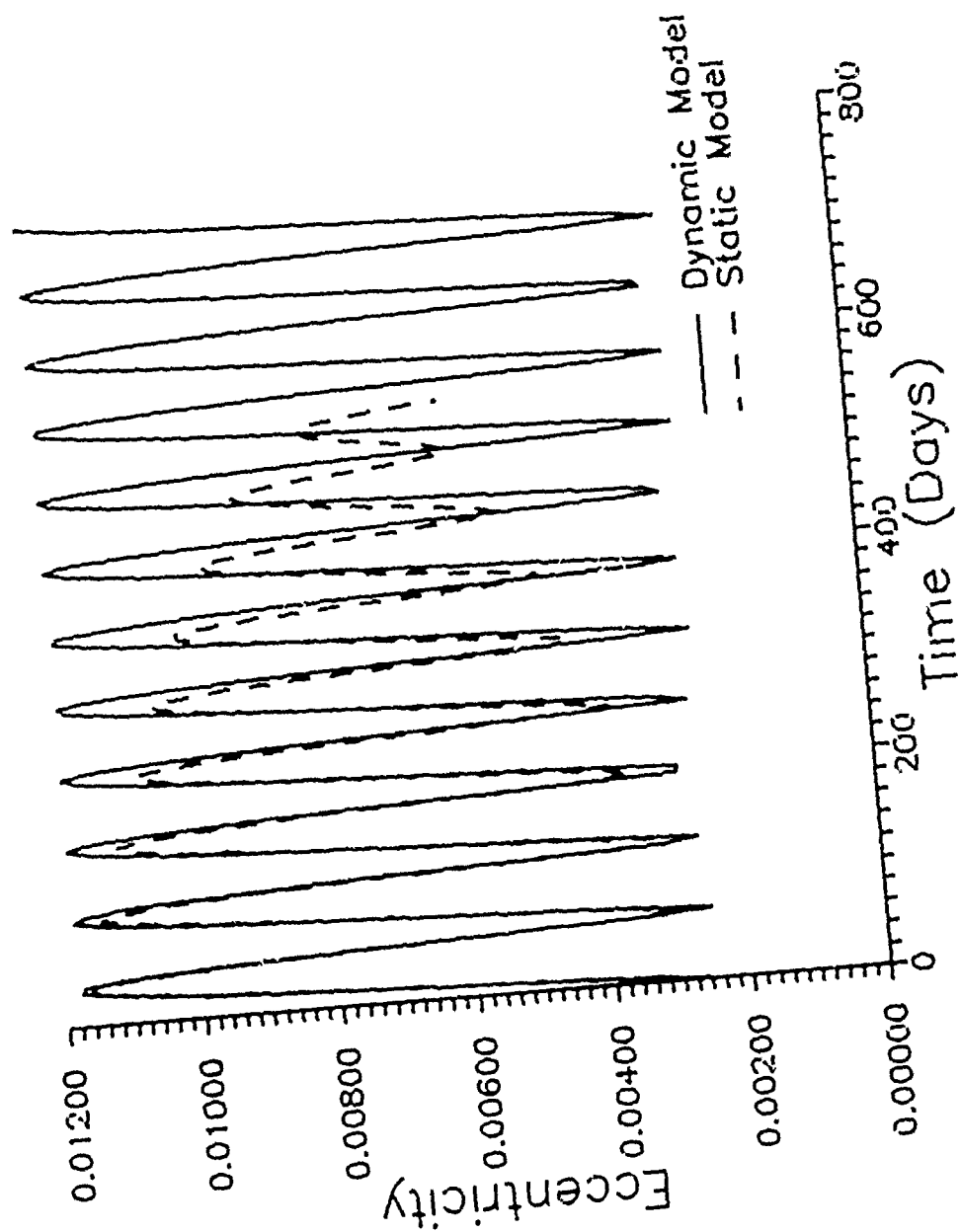
Fig. 5.7: Eccentricity vs. Time (Case 2)

85

Fig. 5.8: Argument of Periapsis vs. Time (Case 2)

— Dynamic Model
-- Static Model

86
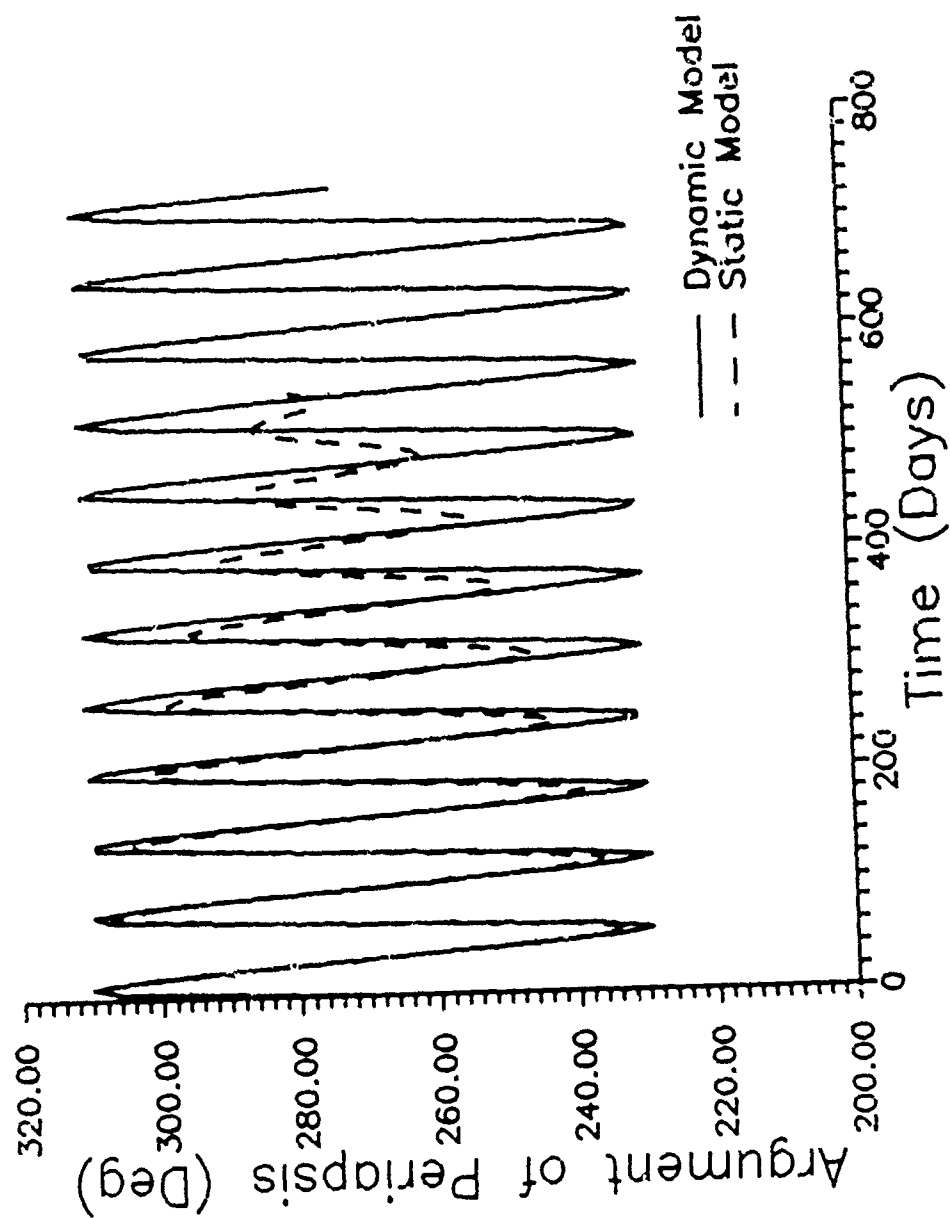
VI. Conclusions and Recommendations

Conclusions

The effect on long term orbital motion about the planet Mars using an initial dynamic model of the Martian atmosphere was studied. The effect is noted through comparing the orbital elements generated by the dynamic model with those generated by a static model of the Martian atmosphere. The following conclusions are evident:

1. The dynamic model exerts less atmospheric drag on the satellite, implying a less dense atmosphere and increasing the lifetime of the satellite.

2. The variation between the models increases with decreasing orbit size, as measured by semimajor axis length for fixed periapsis altitude, and length of time of the trajectory. A further factor is the input data chosen for the static model, particularly the reference density; the smaller the reference density the smaller the amount of variation between the two models.

3. Variation of other orbital parameters than the semimajor axis shows only limited effect on the orbit unless periapsis altitude is decreased as a result of the change.

1. The orbital parameters were internally consistent, which indicated the model worked correctly and supported the conclusions across several parameters.

5. The location of the lower limit of the atmosphere, the beginning of the dense part of the atmosphere, was verified to be at approximately 130 km altitude.

Recommendations

Based on the results of this investigation and on the research that was used to form the models, the following recommendations for further study are proposed:

1. Further data analysis of the space probe data from Mars to develop a better understanding of the Martian atmosphere in order to facilitate model development of the various effects present in the atmosphere as well as to provide standard numbers for such inputs as the reference density in the static model.

2. Development of a model which includes a greater number of the effects existing in the Martian atmosphere; e.g., polar cap sublimation/condensation, atmosphere wave perturbations, and latitude/longitude gradients.

3. Further research generating numerical data using this and subsequent models along with an in depth analysis of the resulting data in order to gain a large data base for the detailed evaluation of dynamic Martian atmosphere effects on long term orbits.

4. Form an atmosphere/trajectory model that includes short term orbits and effects in order to more realistically and accurately represent the Martian atmosphere's effect on orbits.

Appendix A

Supplemental Tables for Sections V and VI

The following pages contain tabulations of the data generated for cases three through seventeen.

Table A.1: Case 3 Data

Dynamic Data

t	a(km)	e	w( )	h_p(km)
0	3725.00000	.00700000	35.00000	301.72500
120	3724.12788	.01383227	311.92456	275.41472
240	3721.07098	.01524739	252.85715	267.13436
360	3717.80320	.01010305	190.60954	283.04203
480	3716.90853	.00538407	73.53509	299.69644
600	3716.61497	.01130528	334.78240	277.39759
720	3716.32255	.01512161	277.59429	262.92579

Case 3 Continued (Static Data)

0	3725.00000	.00700000	35.00000	301.72500
120	3719.66732	.01308124	312.33641	273.80945
240	3713.78845	.01407112	258.51358	264.33127
360	3706.99647	.00961410	209.89607	274.15703
480	3698.84002	.00323519	145.66006	289.67357
600	3688.71651	.00384913	359.54218	277.31814
720	3675.32101	.00694169	318.15801	252.60807

Table A.2: Case 4 Data				
t	a(km)	e	w(°)	h_p(km)

Dynamic Data

0	3700.00000	.00700000	35.00000	276.90000
120	3698.12682	.01223392	330.14531	255.68423
240	3692.44248	.01532293	286.81561	238.66345

t	a(km)	e	w(')	h_p(km)
360	3682.67101	.01516099	251.64807	229.63806
480	3680.42219	.01278364	219.20308	236.17300
600	3679.60498	.00906081	181.90217	249.06478
720	3678.71460	.00553958	124.75665	261.13606
Case 4 Continued (Static Data)				
0	3700.00000	.00700000	35.00000	276.90000
120	3688.67503	.01064301	330.23249	252.21642
240	3673.72708	.01183673	295.34194	233.04217
360	3650.31611	.01051592	276.89075	214.72966
480	3581.29682	.00692021	272.61030	159.31348

Table A.3: Case 5 Data

Dynamic Data				
t	a(km)	e	w(')	h_p(km)
0	3650.00000	.00700000	35.00000	227.25000
120	3639.12449	.00770013	21.16953	213.90275
200	3534.94210	.00583657	49.89566	117.11016
Case 5 Continued (Static Data)				
0	3650.00000	.00700000	35.00000	227.25000
120	3537.30945	.00219324	251.91097	132.35129

Table A.4: Case 6 Data

Dynamic Data				
t	a(km)	e	w(')	h_p(km)
0	3700.00000	.00700000	35.00000	276.90000
15	3699.90603	.01225080	209.15020	257.37920

25	3699.69948	.01580484	289.62480	244.02631
1600	3606.31746	.01280540	309.01570	162.93714

Case 6 Continued (Static Data)

0	3600.00000	.00700000	35.00000	177.60000
15	3578.35719	.01131349	220.85973	140.67348
25	3542.95578	.00947071	276.84234	112.20148

Table A.5: Case 7 Data

Dynamic Data

t	a(km)	e	w( )	h_p(km)
0	40850.00000	.89730000	35.00000	798.09500
120	40850.17026	.90239985	33.76714	589.78284
240	40850.15743	.90189507	33.40832	610.40202
360	40850.08705	.90395227	32.37761	526.35814
480	40849.87620	.90793429	31.92682	36'.67302
600	40849.86727	.90561511	31.69218	458.41004
720	40850.04342	.90774866·	31.05805	371.27116

Case 7 Continued (Static Data)

t	a(km)	e	w( )	h_p(km)
0	40850.00000	.89730000	35.0000	798.09500
120	40850.17025	.90239985	33.76714	589.78282
240	40850.15485	.90189506	33.40832	610.40200
360	40850.08699	.90395230	32.37762	526.35672
480	40849.56663	.90793384	31.92682	363.67195
600	40849.46672	.90561426	31.69216	458.40713
720	40849.57030	.90774763	31.05802	371.26966

Table A.6: Case 8 Data

Dynamic Data

t	a(km)	e	w( )	h_p(km)
0	40850.00000	.88010000	35.00000	1500.71500
120	40850.14119	.88547510	34.06634	1281.15819
240	40850.14505	.88513472	33.97313	1295.06333
360	40850.14171	.88688502	33.11451	1223.56290
480	40849.93049	.89146582	32.82584	1036.41370
600	40849.92690	.88908986	32.69441	1133.47097
720	40850.03299	.89062490	32.09720	1070.77649

Case 8 Continued (Static Data)

t	a(km)	e	w( )	h_p(km)
0	40850.00000	.88010000	35.00000	1500.71500
120	40850.14149	.88547510	34.06634	1281.15819
240	40850.14505	.88513472	33.97313	1295.06333
360	40850.14171	.88688502	33.11451	1223.56290
480	40849.93049	.89146582	32.82584	1036.41370
600	40849.92690	.88908986	32.69441	1133.47097
720	40850.03299	.89062490	32.09720	1070.77649

Table A.7: Case 9 Data

Dynamic Data

t	a(km)	e	w(')	h_p(km)
0	20000.00000	.81500000	35.00000	302.80000
120	20000.14489	.81707038	30.55843	261.41888
240	20000.09376	.81652226	26.38588	272.37194

94

360	19999.88509	.81900112	22.13464	222.75686
480	19999.88517	.81914910	18.15247	219.79727
600	19999.99772	.81970941	14.17258	208.61129
720	20000.10522	.82134796	10.25674	175.85950
Case 9 Continued (Static Data)				
0	20000.00000	.81500000	35.00000	302.80000
120	19997.16488	.81704281	30.55800	261.42503
240	19991.53239	.81644413	26.38310	272.36303
360	19983.11872	.81884697	22.12759	222.80246
480	19962.07634	.81880413	18.13516	219.84581
600	19942.69444	.81918958	14.13833	208.64696
720	19896.59695	.82040012	10.19529	176.22649

Table A.8: Case 10 Data				
Dynamic Data				
t	a(km)	e	$w(°)$	$h_p(km)$
0	10000.00000	.63530000	35.00000	249.80000
120	10000.01059	.63637648	19.28367	239.03901
240	9999.72140	.63753083	3.64970	227.39073
360	9999.69490	.63849873	348.09572	217.70236
480	9999.59779	.63887910	332.57364	213.86379
600	9999.49199	.63926847	317.06785	209.93206
720	9999.68040	.63922917	301.51692	210.39302
Case 10 Continued (Static Data)				
0	10000.00000	.63530000	35.00000	249.80000

120	9993.83322	.63615189	19.27510	239.03732
240	9985.15170	.63700294	3.61037	227.38074
360	9972.37600	.63750990	347.99307	217.68755
480	9957.81858	.63736709	332.36542	213.83274
600	9943.16039	.63723235	316.70995	209.85690
720	9929.67438	.63671780	300.96585	210.07400

Table A.9: Case 11 Data				
Dynamic Data				
t	a(km)	e	$w(^{\circ})$	h_p(km)
0	5000.00000	.27060000	35.00000	249.80000
120	4999.82315	.27639218	321.55416	220.71115
240	4999.24985	.27789333	249.28687	212.79168
360	4995.78748	.27247961	176.40634	237.33727
480	4995.71358	.26798495	101.86486	259.73753
600	4995.70813	.27050704	26.99135	247.13392
720	4995.70066	.27625108	313.53795	218.43295
Case 11 Continued (Static Data)				
0	5000.00000	.27060000	35.00000	249.80000
120	4993.73020	.27552065	321.45260	220.65443
240	4985.17939	.27584452	248.80682	212.84497
360	4977.42737	.26963612	175.28874	238.13316
480	4973.82942	.26467018	99.90200	260.20509
600	4971.05403	.26705131	24.12279	246.32757
720	4964.24556	.27183542	309.66514	217.58779

	Table A.10: Case 12 Data			
Dynamic Data				
t	a(km)	e	$w( )$	$h_p(km)$
0	5000.00000	.27060000	35.00000	249.80000
120	4999.60428	.27082420	13.94098	248.39044
240	4999.07370	.27113772	353.17342	246.43624
360	4996.34753	.27109197	333.39445	244.67784
480	4996.14283	.27130026	314.36703	243.48798
600	4996.10494	.27144986	295.41280	242.71297
720	4996.03811	.27155605	276.47089	242.13372
Case 12 Continued (Static Data)				
0	5000.00000	.27060000	35.00000	249.80000
120	4995.35223	.27018277	15.18149	248.49412
240	4990.66638	.26982746	357.96249	246.84755
360	4985.98804	.26937066	343.36737	245.70918
480	4981.33806	.26885673	331.41692	244.87178
600	4976.67017	.26829597	322.13487	244.24964
720	4971.96437	.26771465	315.53546	243.69665

	Table A.11: Case 13 Data			
Dynamic Data				
t	a(km)	e	$w(°)$	$h_p(km)$
0	10000.00000	.63530000	35.00000	249.80000
120	10000.15440	.63498769	259.90822	252.97946
240	10000.21016	.63393996	124.93690	263.47730

97

360	10000.10408	.63521187	351.60167	250.71925
480	9999.74419	.63609138	216.29255	241.79315
600	9999.60265	.63494866	83.38914	253.16839
720	9999.60450	.63581136	309.91811	244.51236

Case 13 Continued (Static Data)				
0	10000.00000	.63530000	35.00000	219.80000
120	9994.95423	.63479912	260.02277	252.96605
240	9990.65152	.63359845	125.37798	263.39020
360	9985.43387	.63468131	352.58220	250.66565
480	9979.11712	.63534572	218.06626	241.72776
600	9972.40889	.63394591	86.16906	253.24105
720	9966.37191	.63460121	314.11492	244.50021

Table A.12: Case 14 Data				
Dynamic Data				
t	a(km)	e	$w(')$	$h_p(km)$
0	20000.00000	.81500000	35.00000	302.80000
120	20000.32918	.81479121	96.77242	307.03684
240	20000.53455	.81782455	159.37721	246.40634
360	20000.57169	.81912787	225.67056	220.34600
480	20000.42574	.81753433	292.68151	252.19106
600	20000.29002	.81569181	357.09877	289.01717
720	20000.08480	.81477000	60.15629	307.41565
Case 14 Continued (Static Data)				
0	20000.00000	.81500000	35.00000	302.80000

120	19998.77302	.81477669	96.77658	307.03890
240	19994.79723	.81777109	159.39778	246.43019
360	19978.02947	.81892391	225.76558	220.34343
480	19964.35529	.81721454	292.94967	251.99383
600	19959.31764	.81533099	357.59101	288.66735
720	19957.00771	.81437821	60.88218	307.25542

Table A.13: Case 15 Data				
Dynamic Data				
t	a(km)	e	$w(°)$	h_p(km)
0	5000.00000	.27060000	35.00000	249.80000
120	4999.55755	.26966883	131.50579	254.13272
240	4999.17581	.27733025	226.22172	215.55313
360	4996.54172	.27670514	318.84402	216.77295
480	4996.23941	.26894529	53.25147	255.32435
600	4996.18743	.27044997	149.18642	247.76869
720	4996.09627	.27790313	242.90518	210.46549
Case 15 Continued (Static Data)				
0	5000.00000	.27060000	35.00000	249.80000
120	4992.72282	.26863994	130.99989	254.27807
240	4986.82938	.27542920	224.50469	216.11097
360	4981.82717	.27476373	315.32094	215.80178
480	4975.91550	.26627296	47.01537	253.76373
600	4968.69449	.26566655	139.58943	251.47856
720	4962.87185	.27232759	229.45923	214.14492

Table A.14: Case 16 Data			
Dynamic Data				
t	a(km)	e	w(˙)	h_p(km)
0	10000.00000	.63530000	35.00000	249.80000
120	9999.95380	.63788457	338.16373	223.93753
240	9999.87033	.63925371	281.67942	210.21608
360	9998.83121	.63836116	225.28241	218.76572
480	9998.87389	.63625965	168.61203	239.79389
600	9998.86252	.63437761	11.56627	258.60798
720	9999.01324	.63428386	54.41548	259.60056
Case 16 Continued (Static Data)				
0	10000.00000	.63530000	35.00000	249.80000
120	9991.71527	.63758789	338.12500	223.91864
240	9980.55809	.63856010	281.48910	210.17196
360	9969.78988	.63729995	224.82070	218.84329
480	9959.72721	.63479035	167.76473	240.18852
600	9954.98099	.63274012	110.24516	258.86516
720	9952.39850	.63264429	52.58695	258.87037

Table A.15: Case 17 Data			
Dynamic Data				
t	a(km)	e	w(˙)	h_p(km)
0	20000.00000	.81500000	35.00000	302.80000
120	20000.06508	.81675934	19.03105	267.62517
240	20000.01976	.81658411	3.07461	271.12147

360	20000.01611	.81758658	347.07064	251.07133
480	20000.12724	.81638078	331.20081	275.20775
600	20000.12863	.81594742	315.40398	283.87521
720	20000.11430	.81589036	299.70516	285.01381
Case 17 Continued (Static Data)				
0	20000.00000	.81500000	35.00000	302.80000
120	19997.34369	.81673420	19.02958	267.62926
240	19991.65376	.81650769	3.06544	271.11480
360	19985.81237	.81745654	347.04657	251.07940
480	19979.58406	.81619343	331.15241	275.17885
600	19976.79774	.81573750	315.32567	283.77468
720	19974.07560	.81565400	299.59326	284.94085

Appendix B

Supplemental Figures for Sections V and VI

The following pages contain two dimensional graphs of the data tabulated in Appendix A.
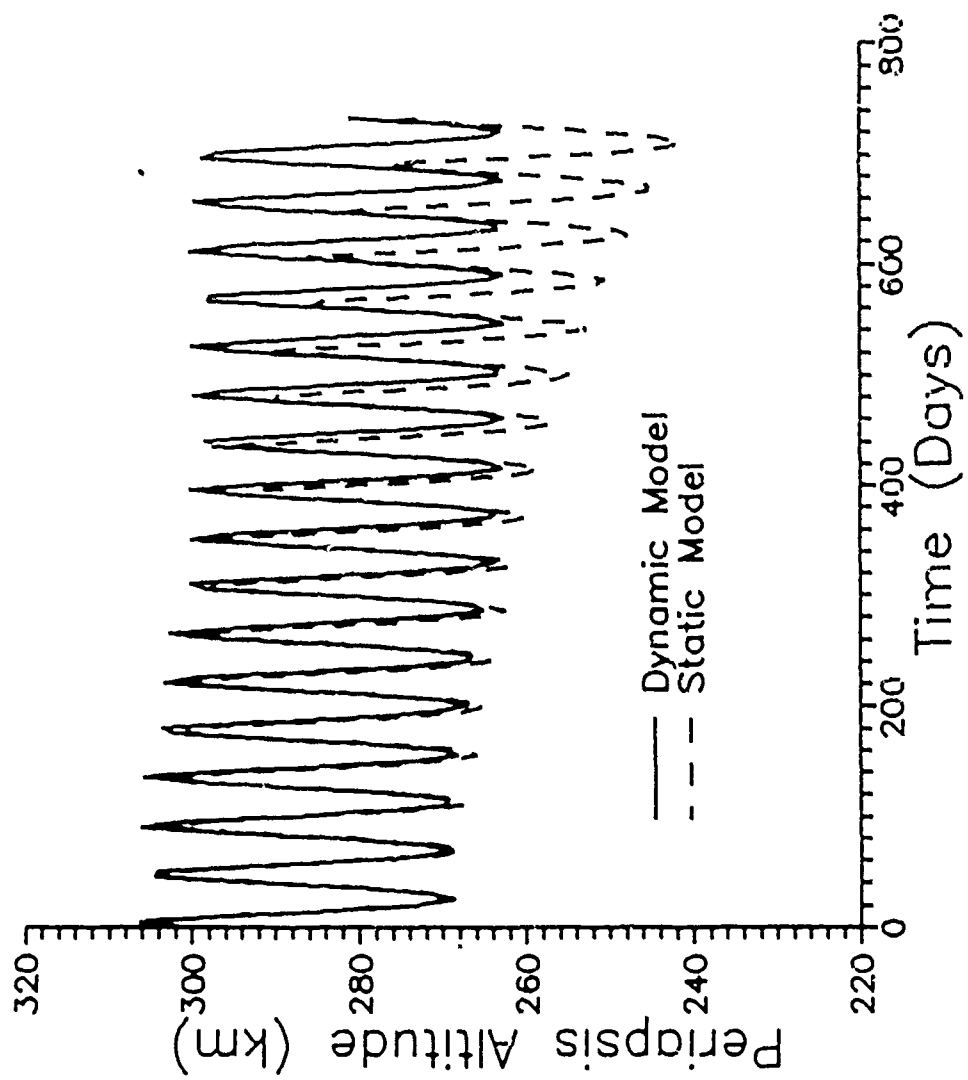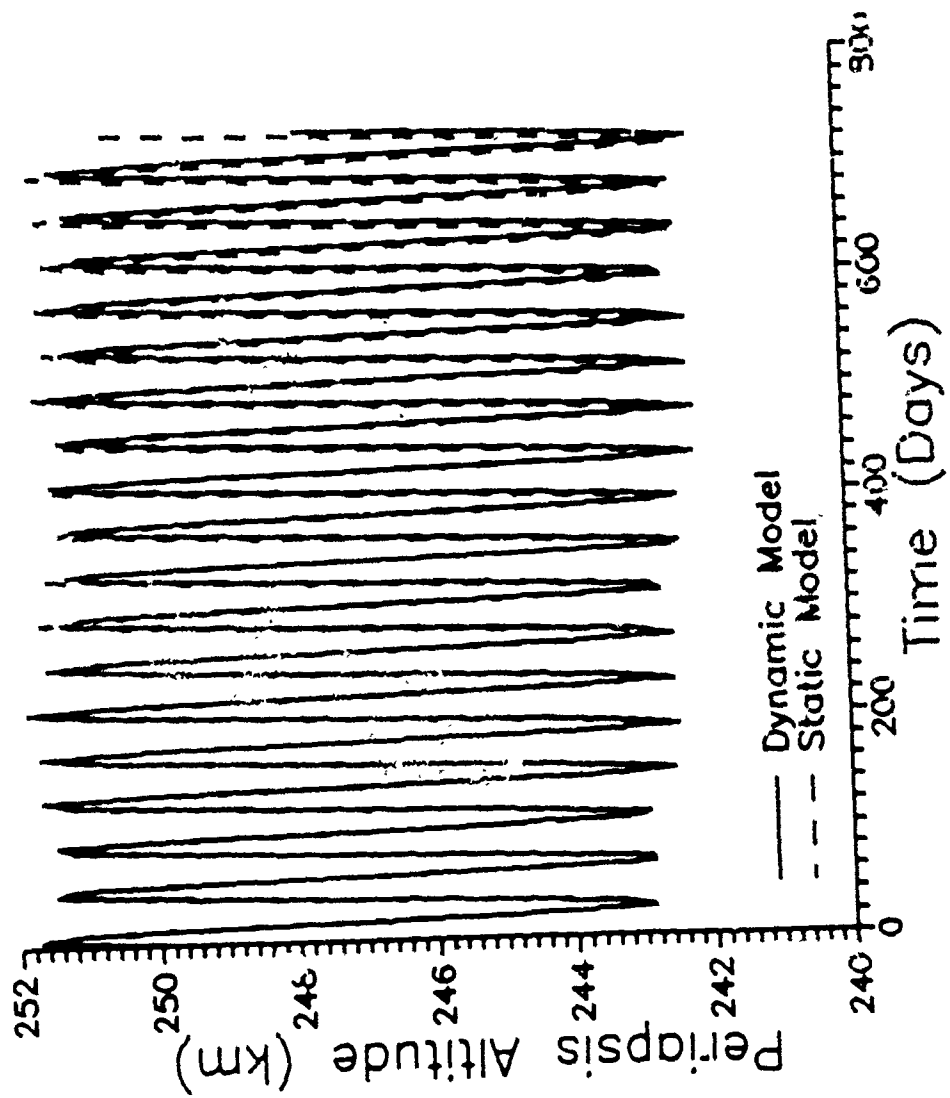
Fig. B.1: Periapsis Altitude vs. Time (Case 3)

103
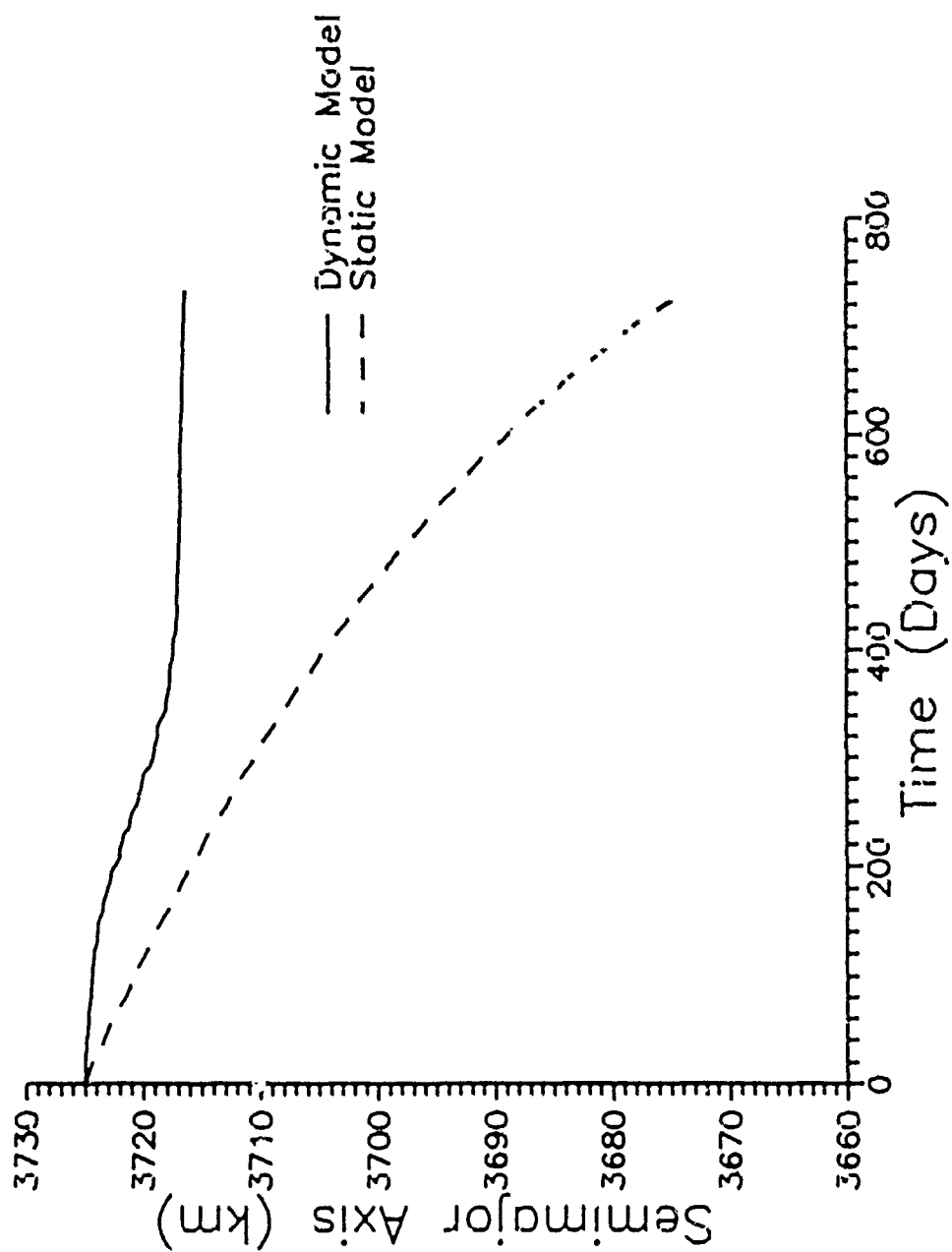
Fig. B.2: Semimajor Axis vs. Time (Case 3)
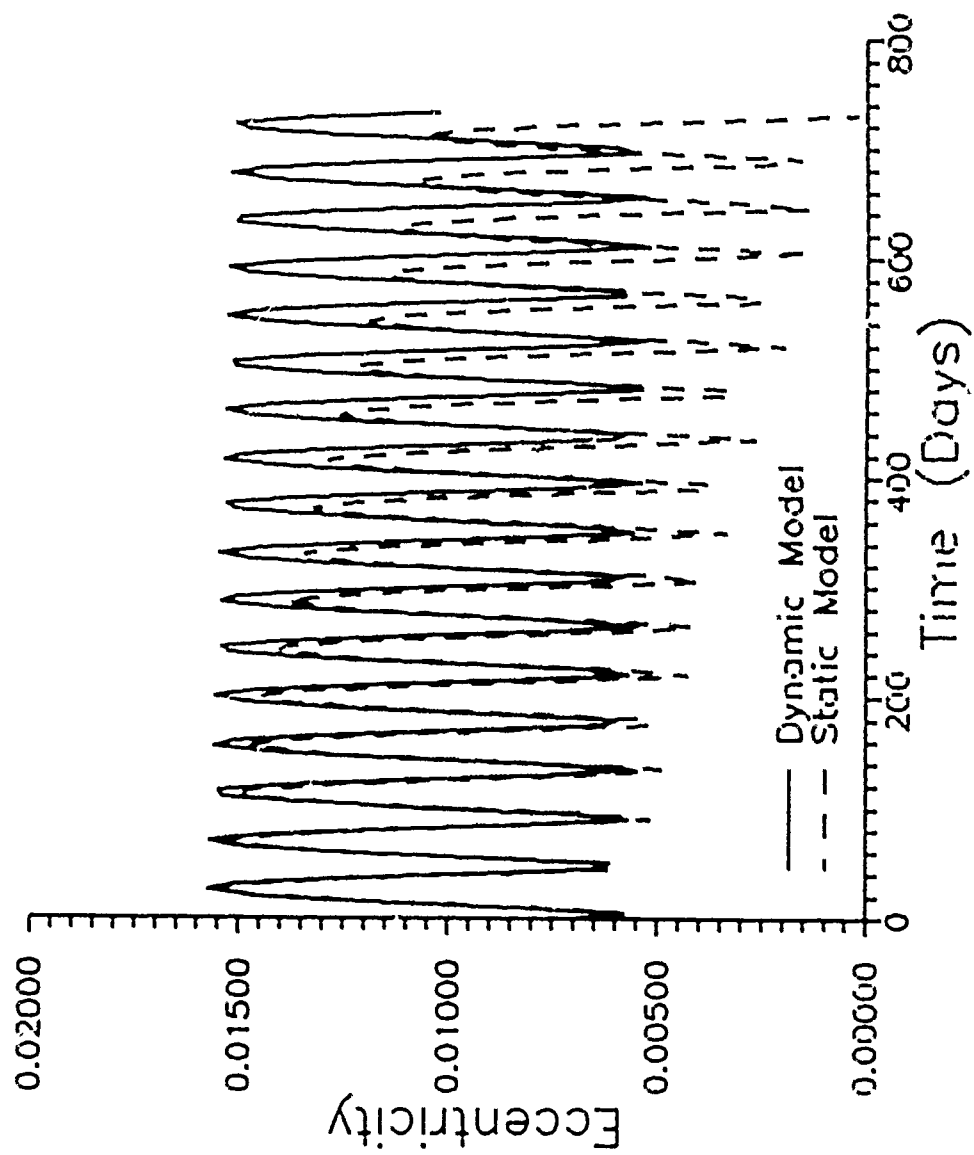
Fig. B.3: Eccentricity vs. Time (Case 3)

Eccentricity

Dynamic Model
Static Model

Time (Days)
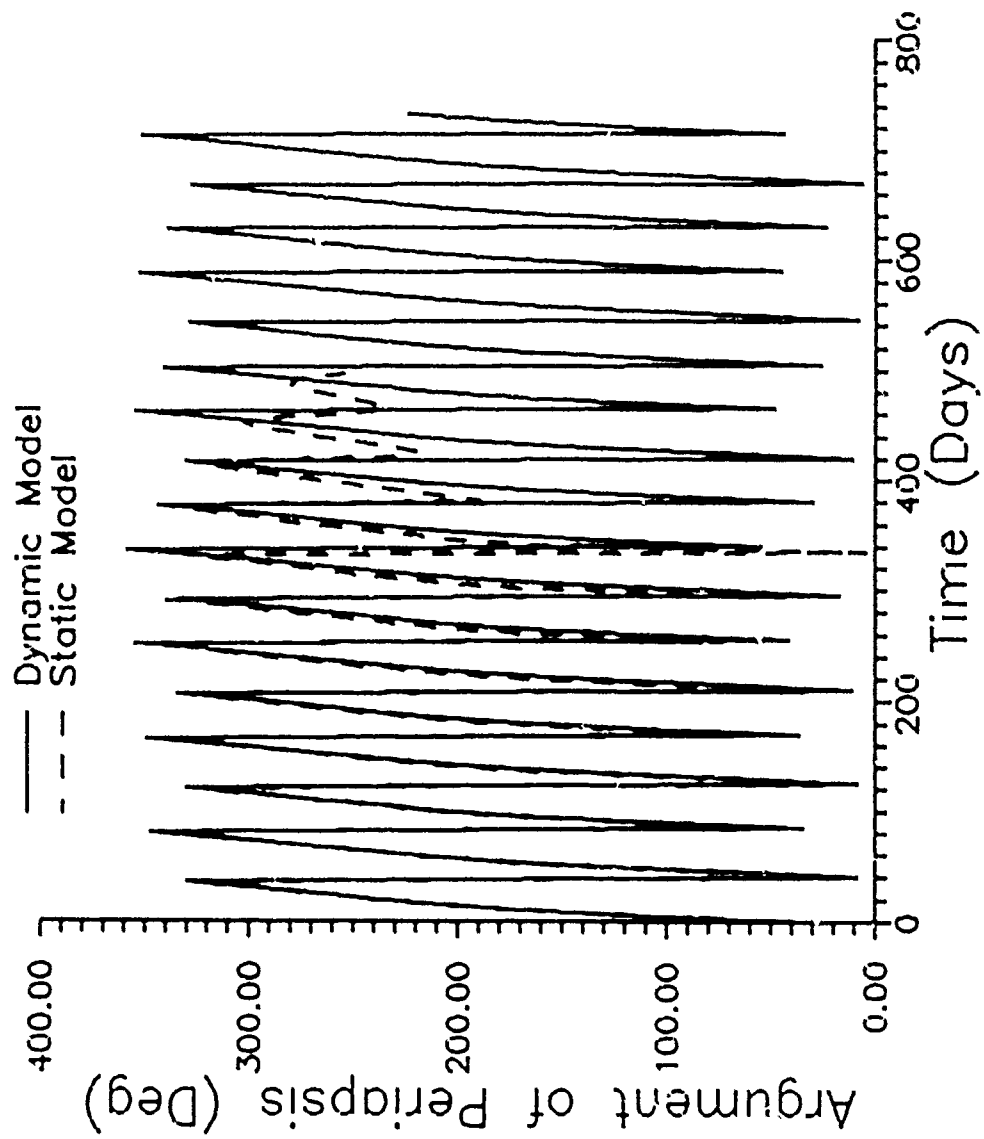
Fig. B.4: Argument of Periapsis vs. Time (Case 3)
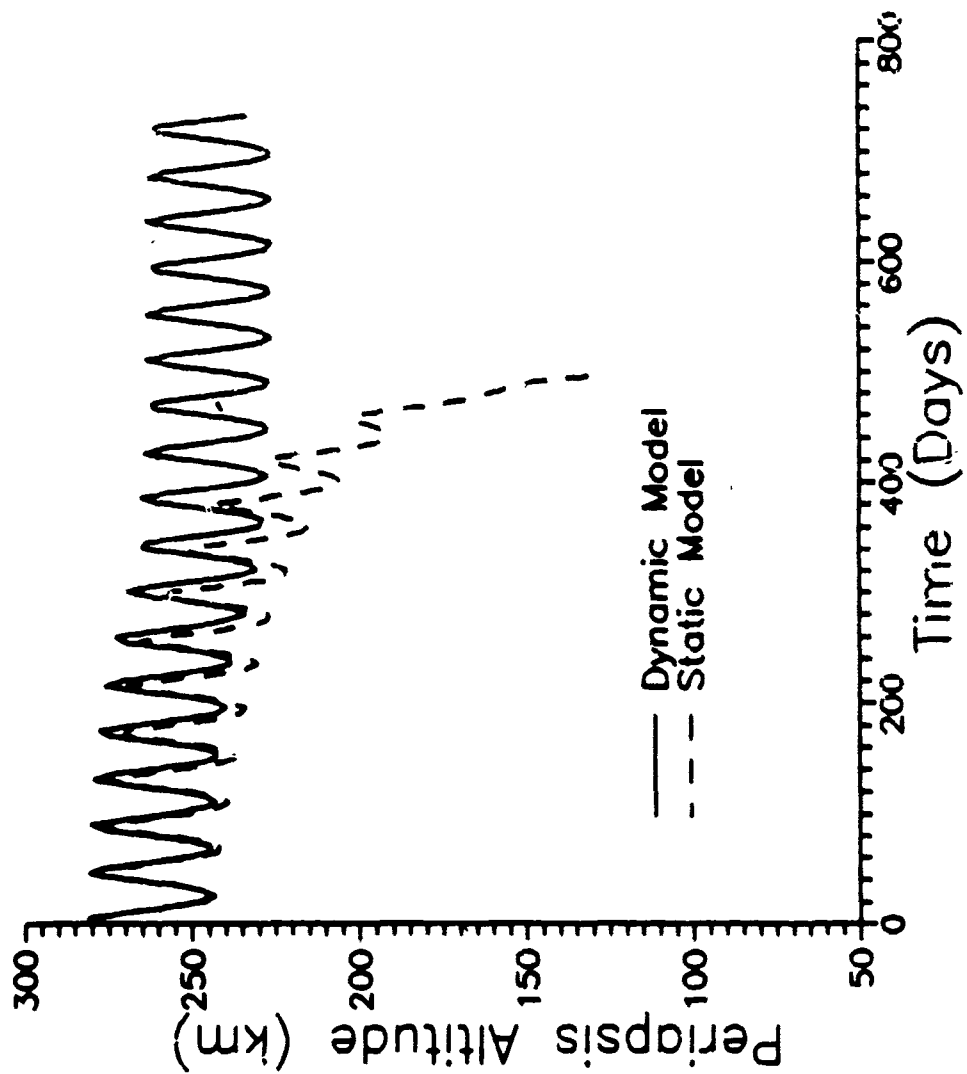
Fig. B.5: Periapsis Altitude vs. Time ((Case 4)

107
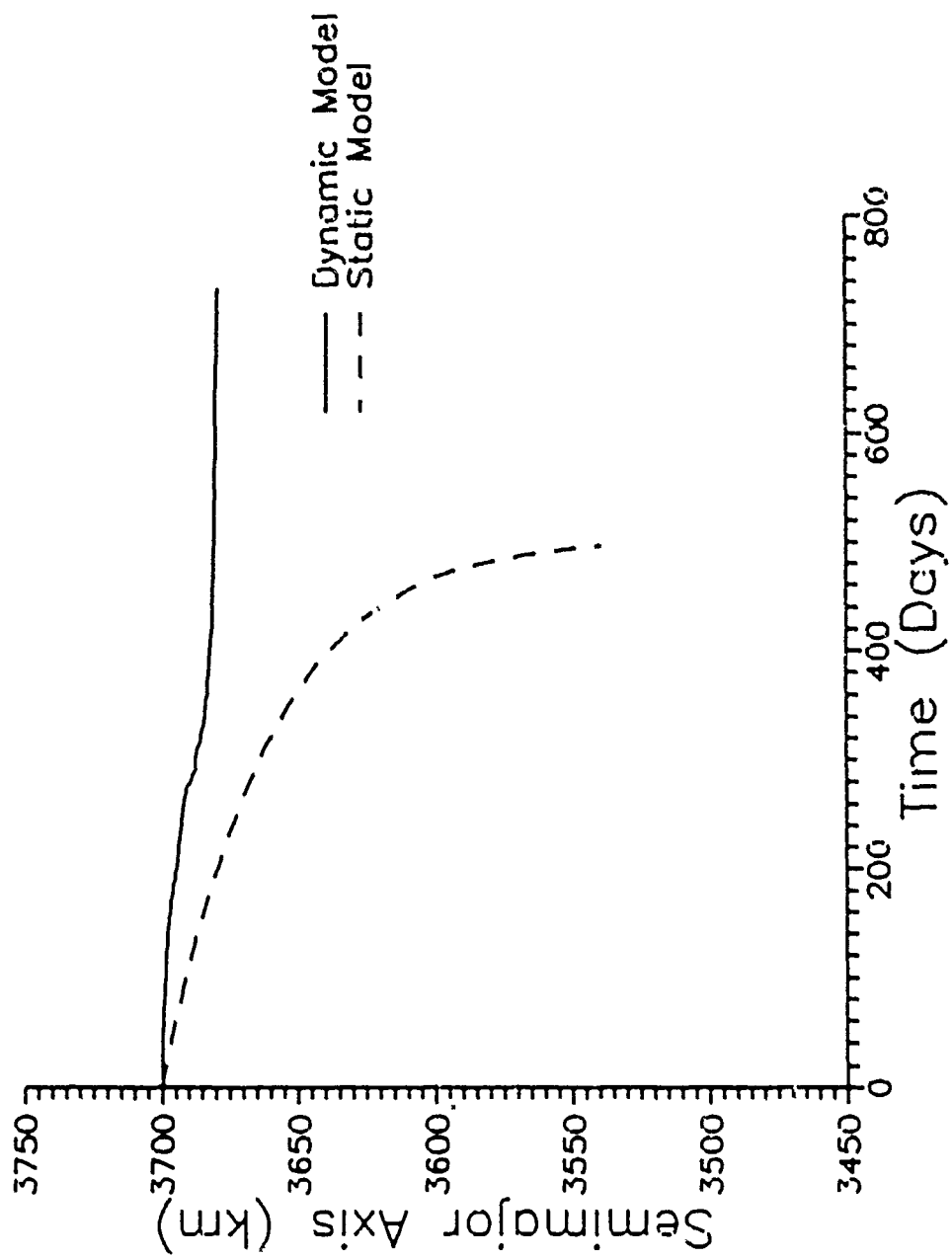
Fig. B.6: Semimajor Axis vs. Time (Case 4)
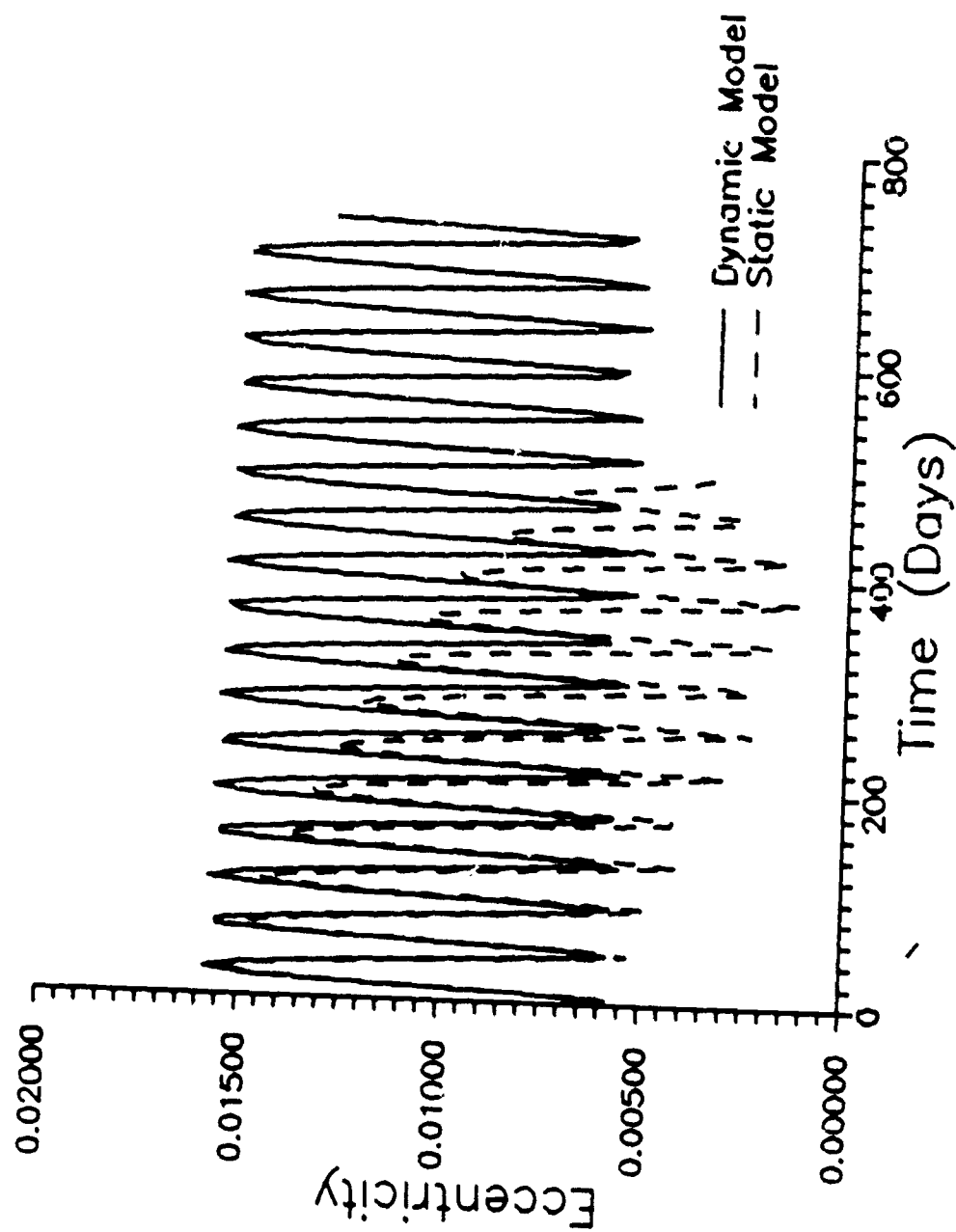
Fig. B.7: Eccentricity vs. Time (Case 4)
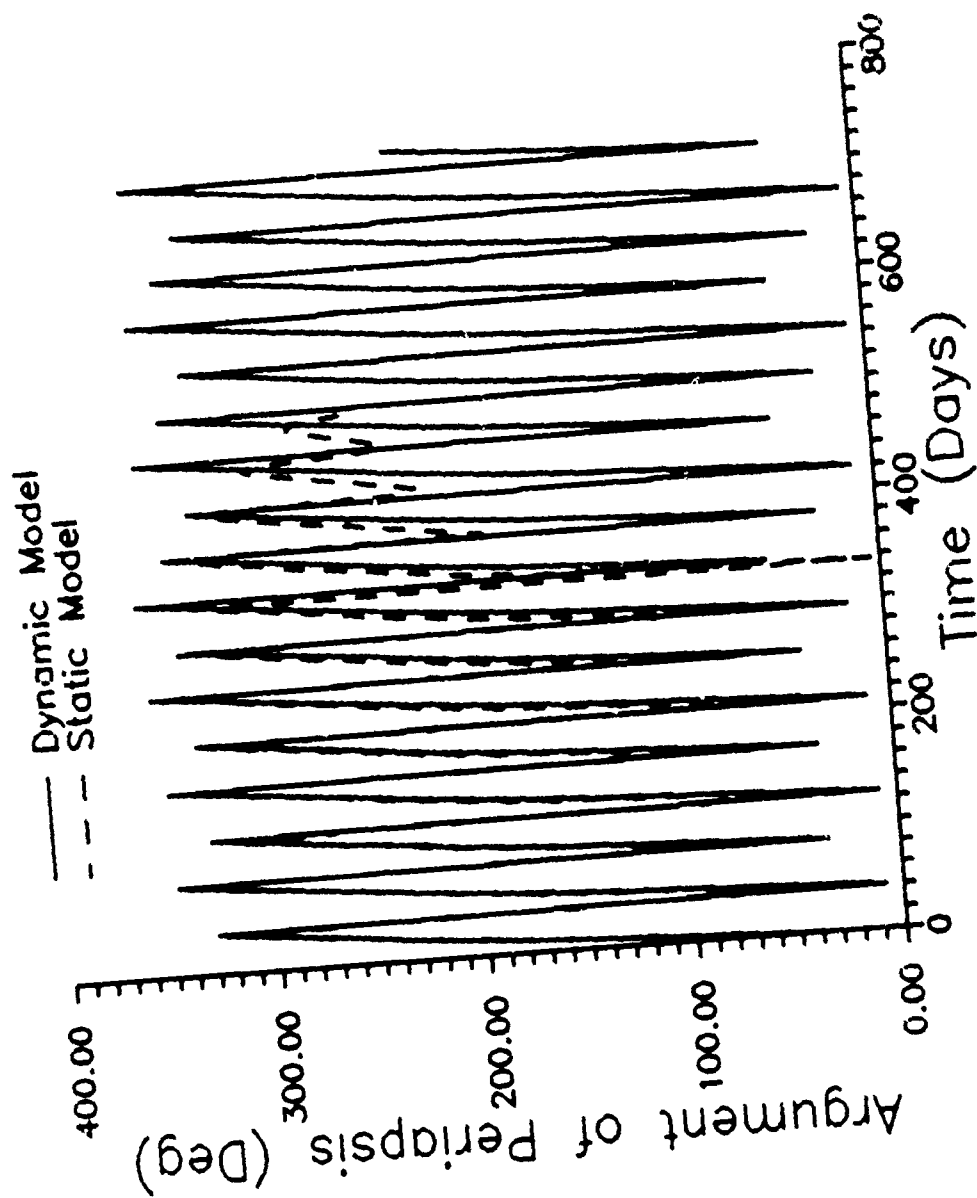
Fig. B.8: Argument of Periapsis vs. Time (Case 4)

110
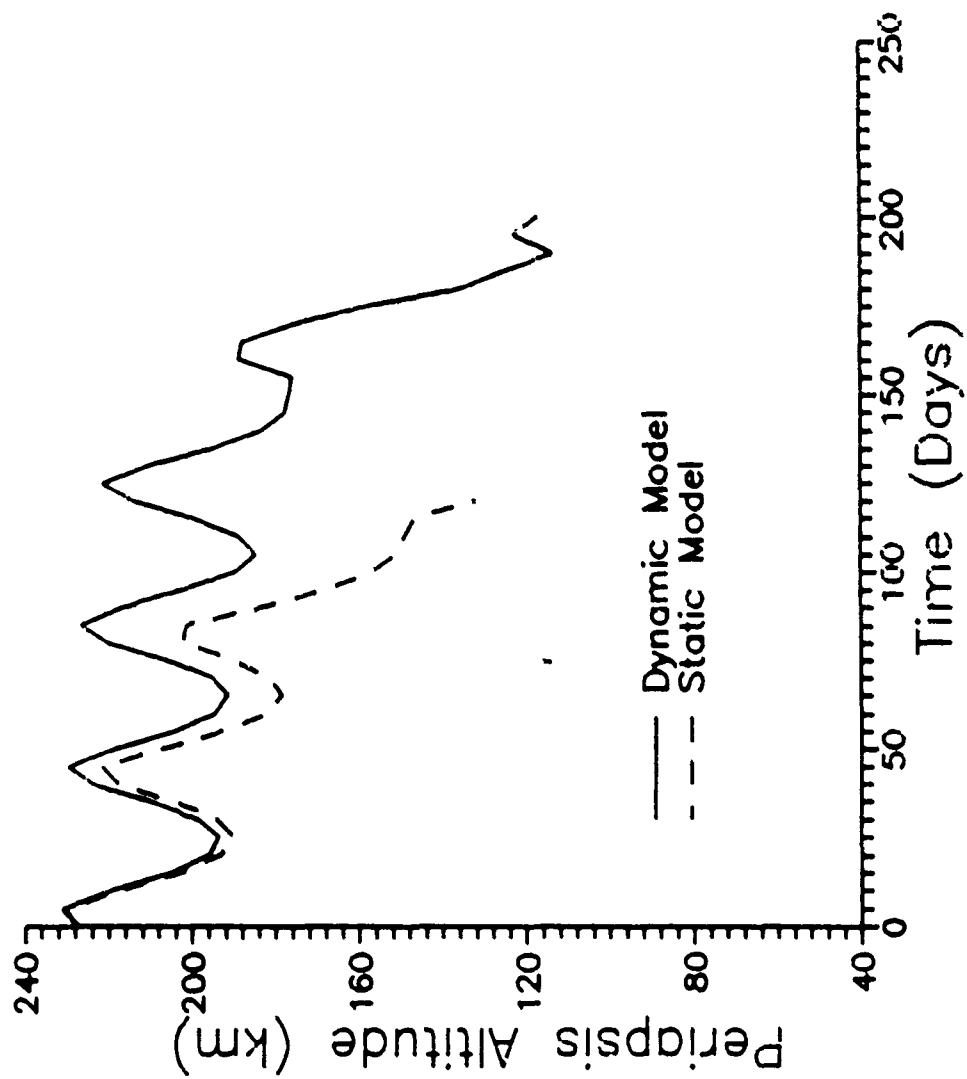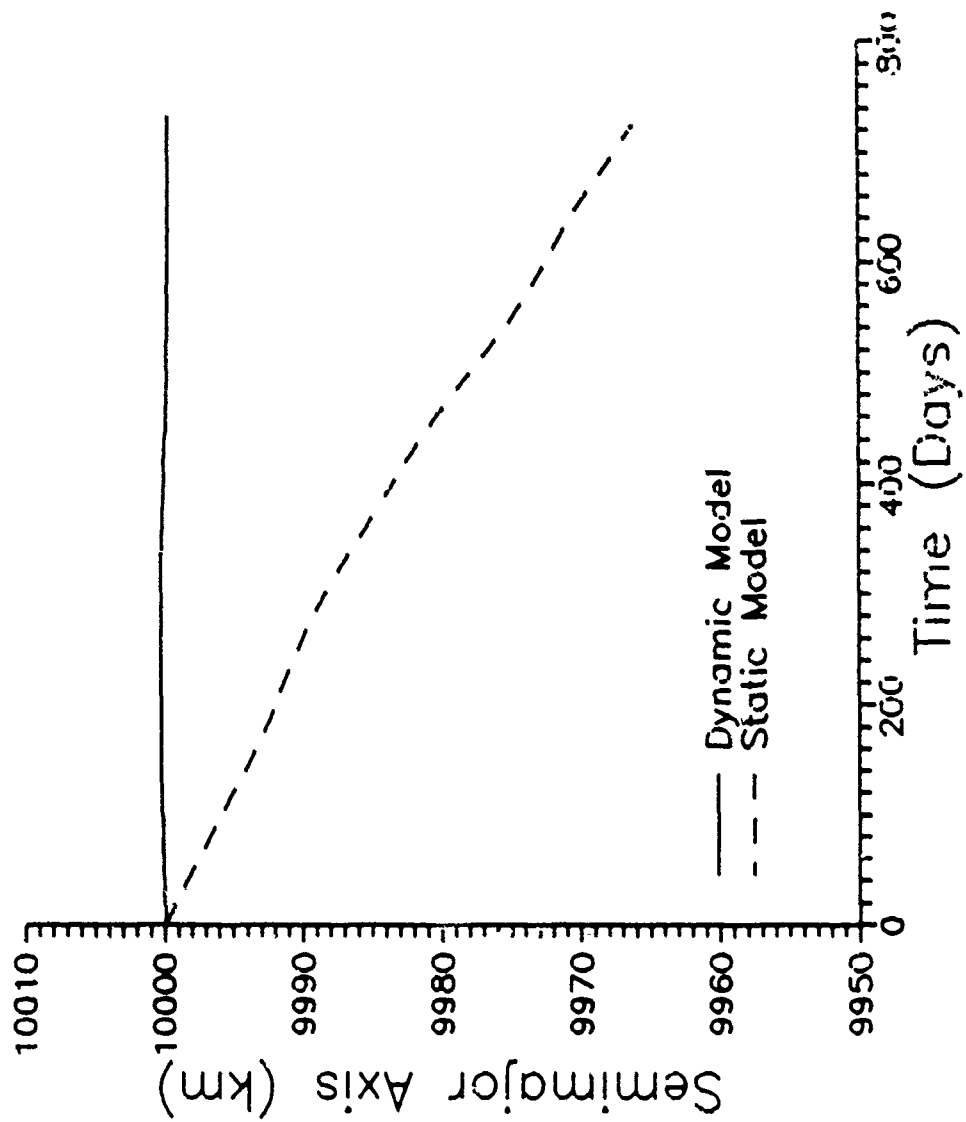
Fig. B.9: Periapsis Altitude vs. Time ((Case 5)
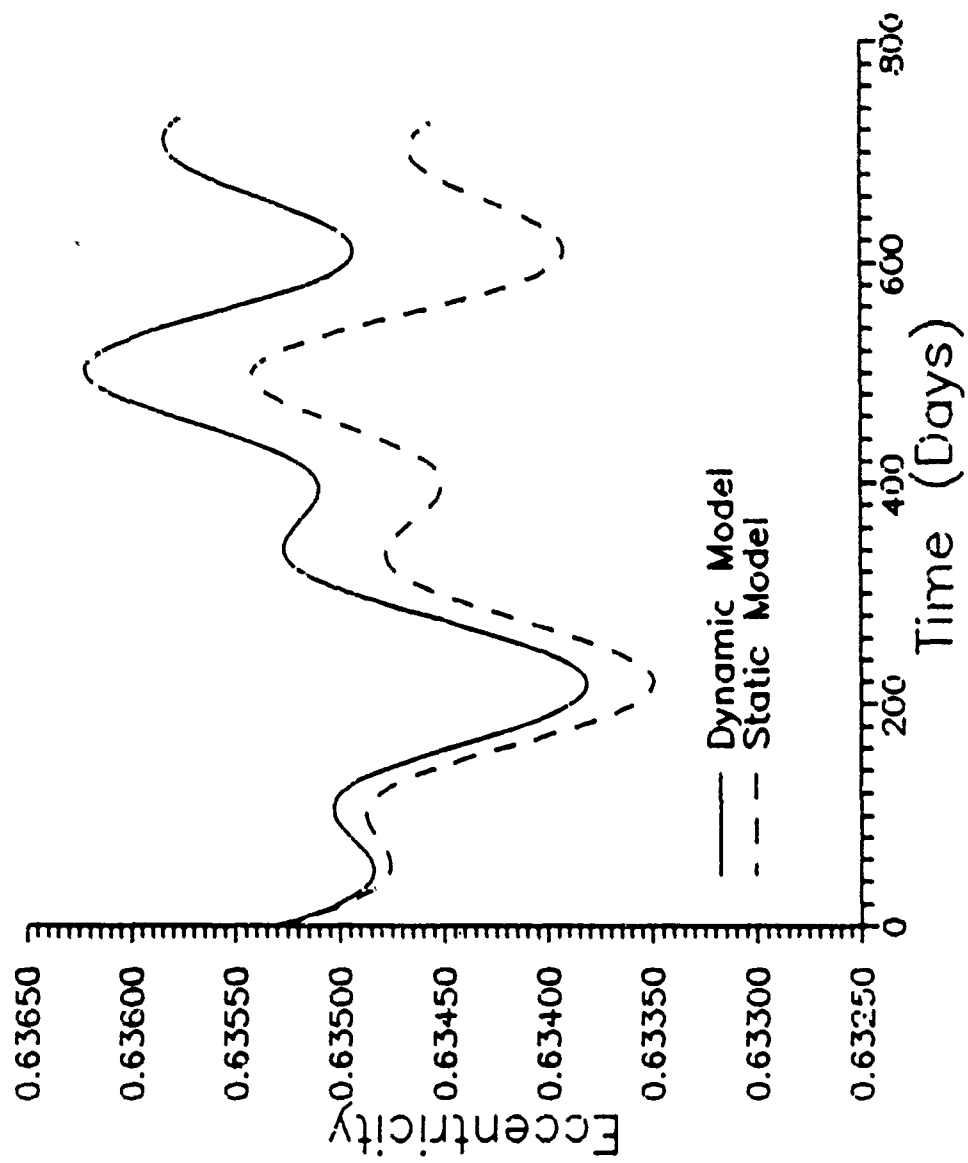
111
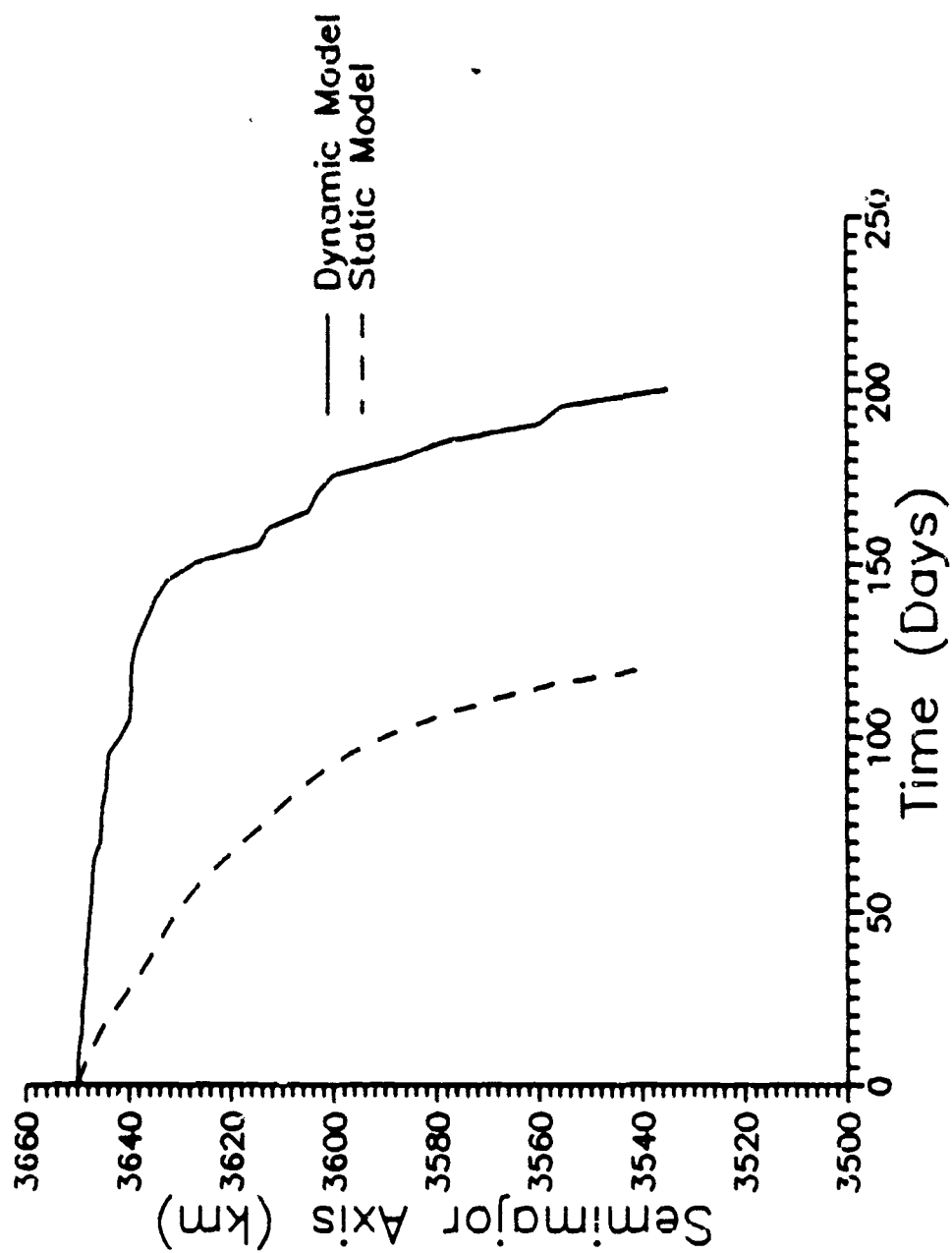
Fig. B.10: Semimajor Axis vs. Time (Case 5)
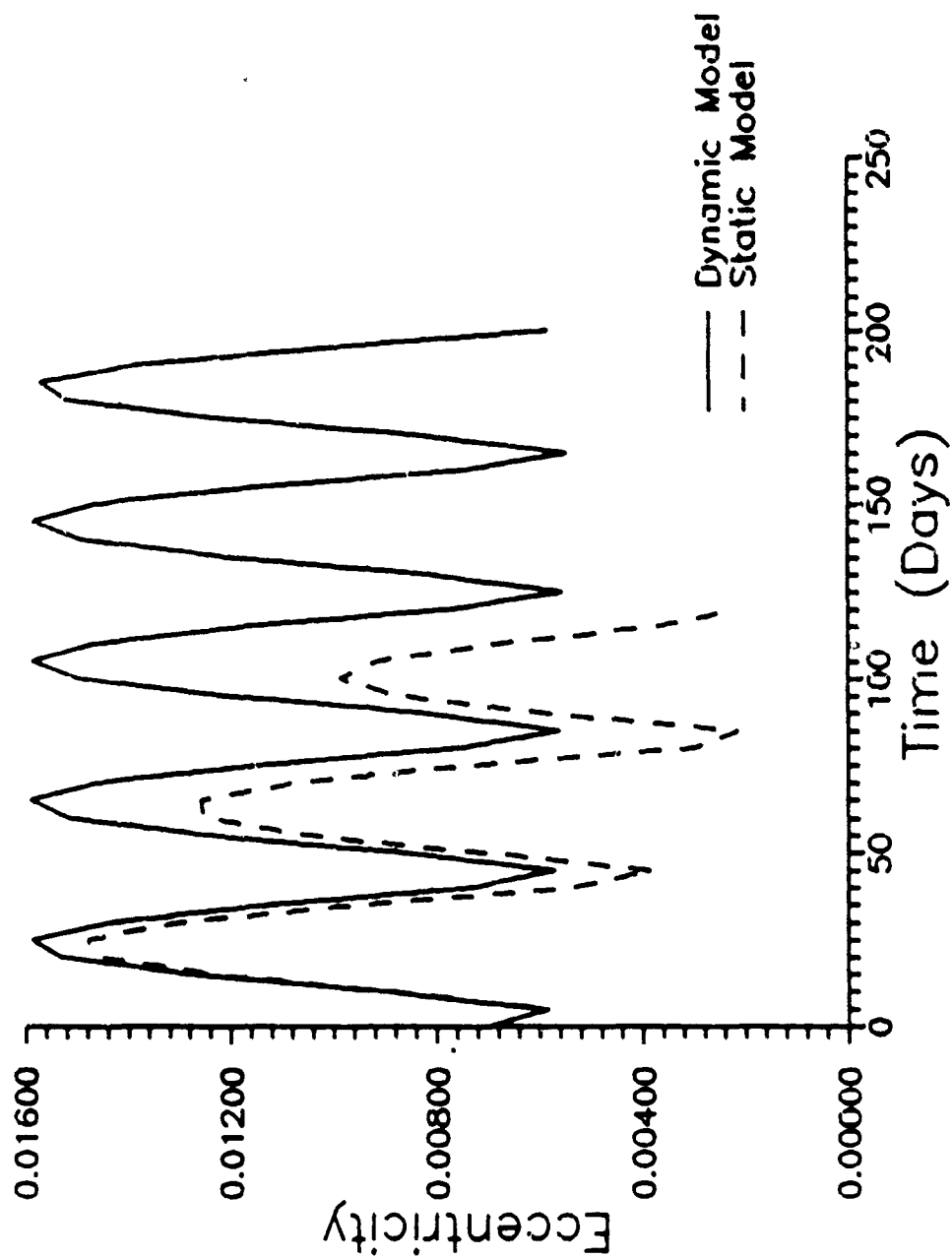
Fig. B.11: Eccentricity vs. Time (Case 5)

113
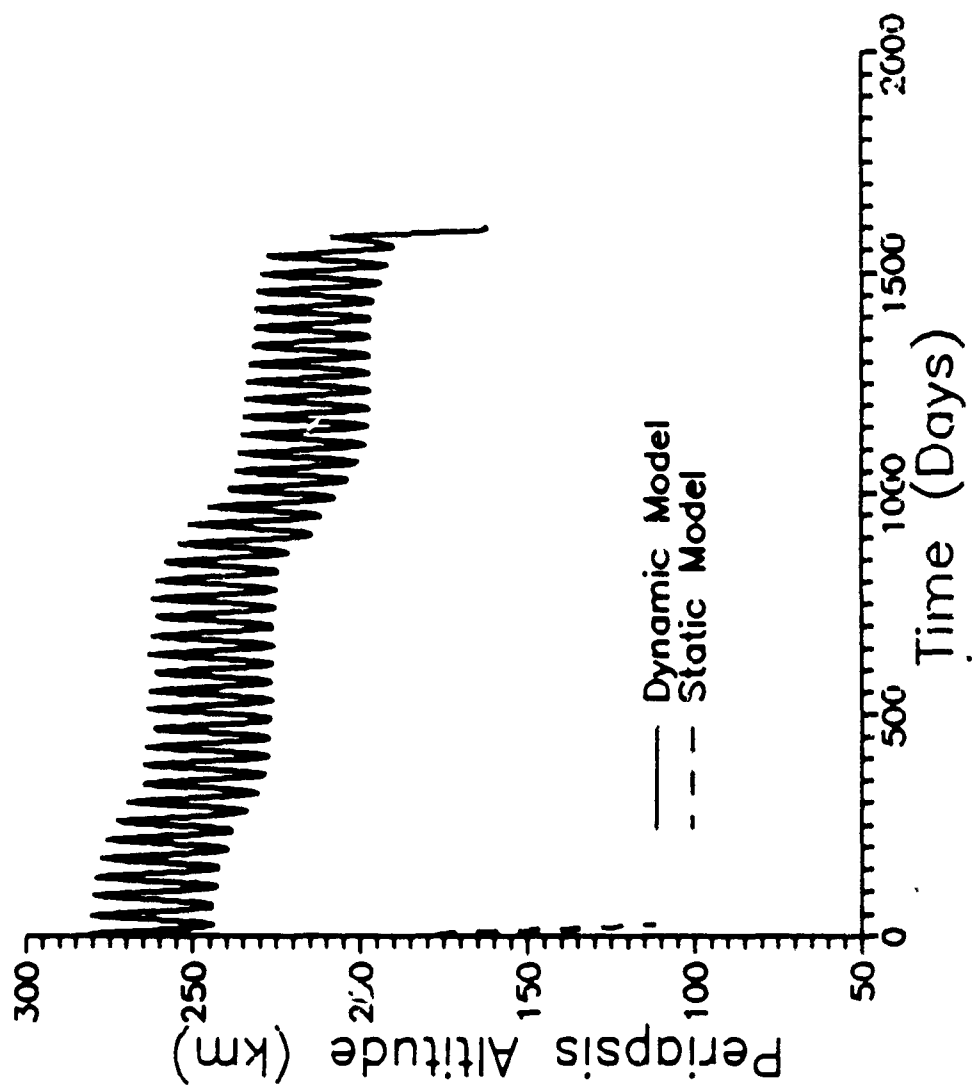
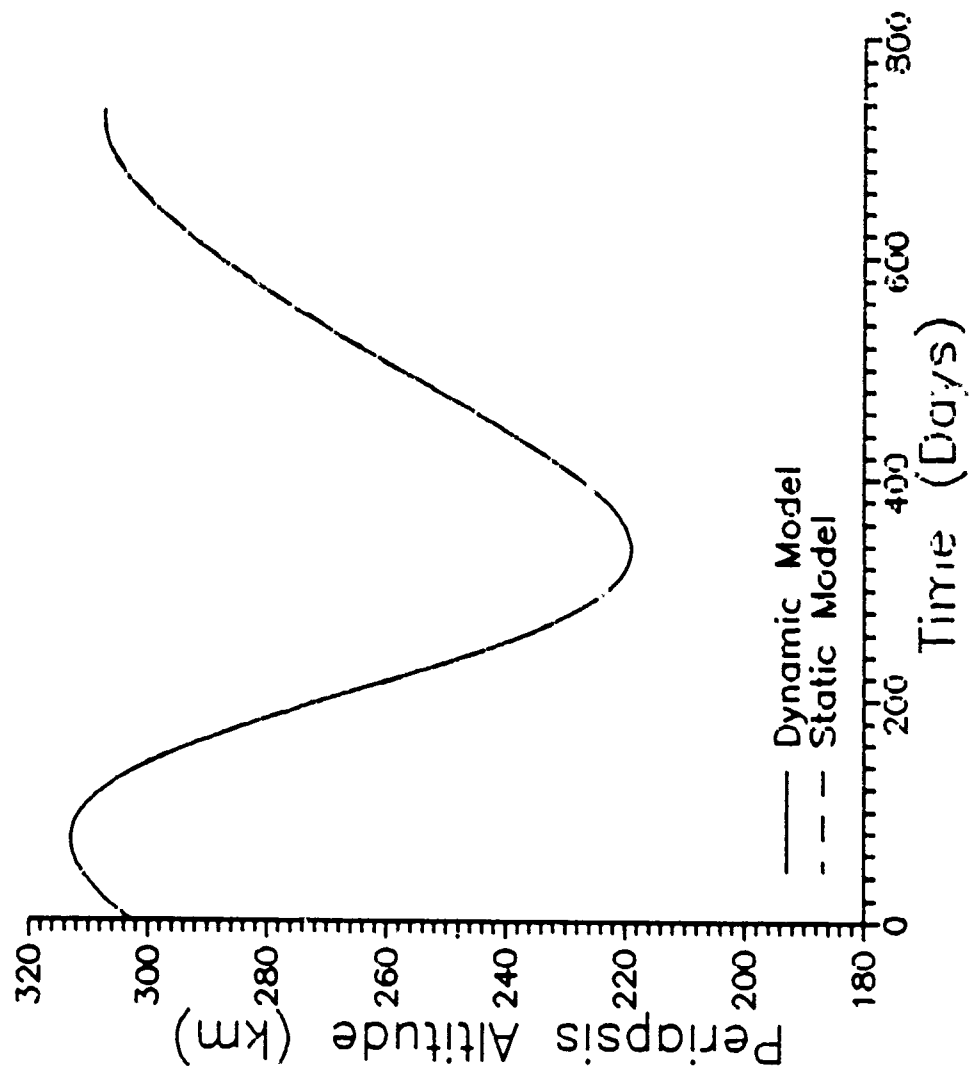Fig. B.12: Periapsis Altitude vs. Time (Case 6)
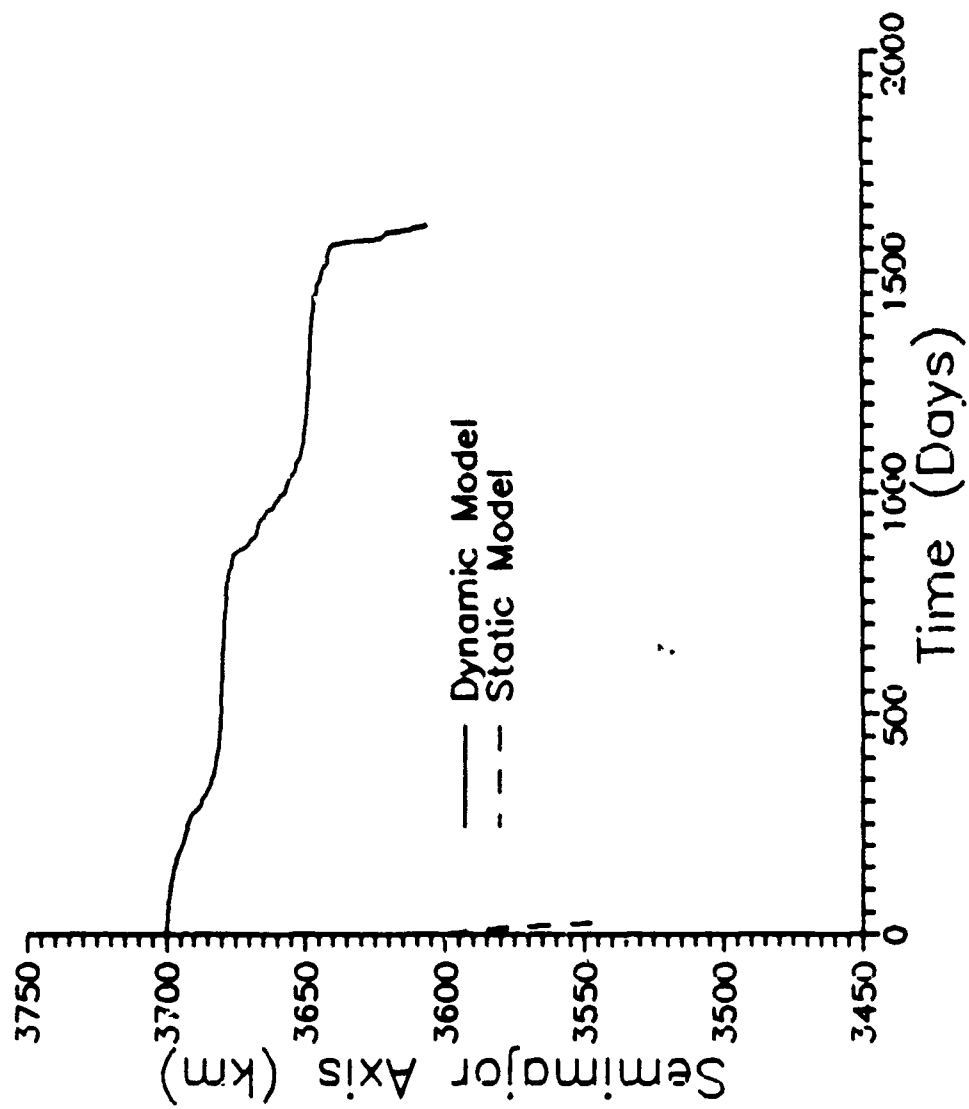
Fig. B.13: Semimajor Axis vs. Time (Case 6)

115
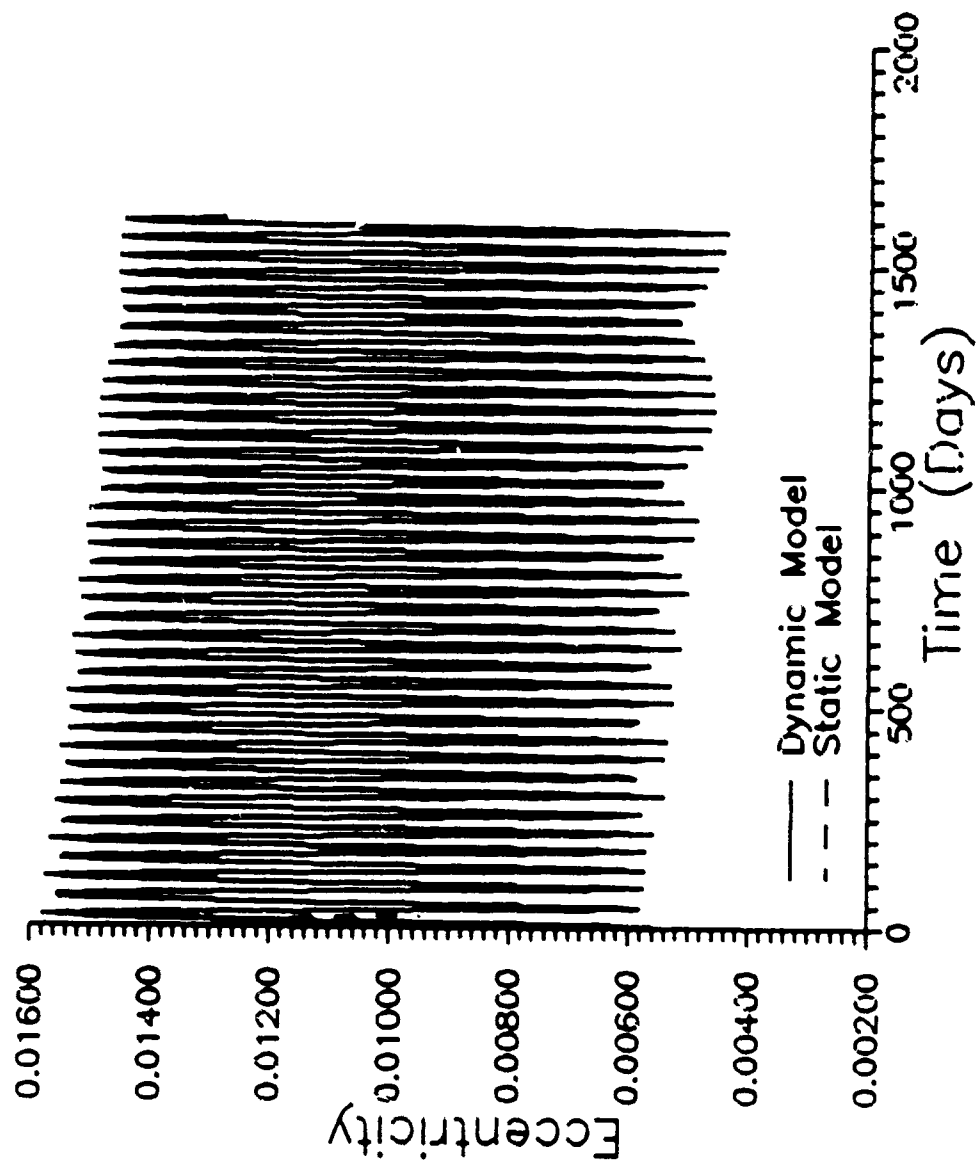
Fig. B.14: Eccentricity vs. Time (Case 6)

116
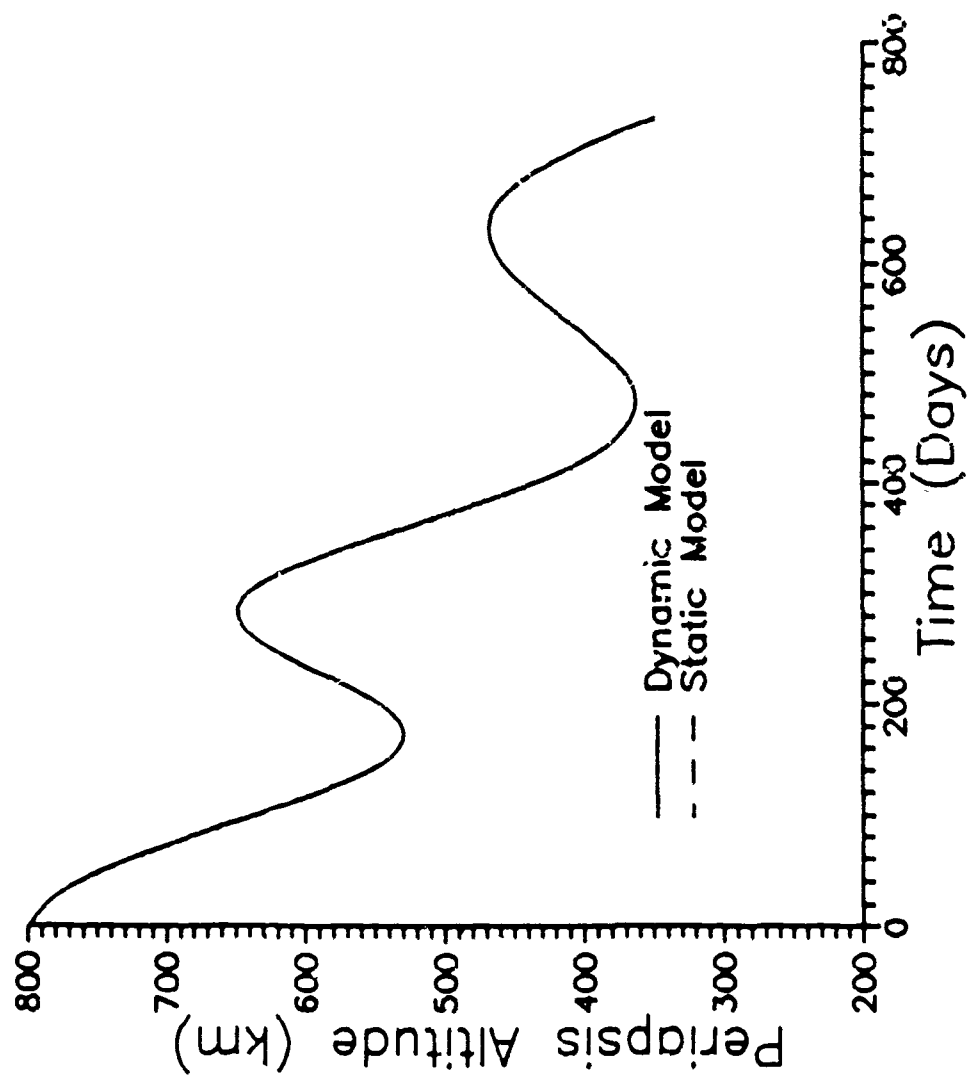
Fig. B.15: Periapsis Altitude vs. Time (Case 7)

— Dynamic Model
– – Static Model
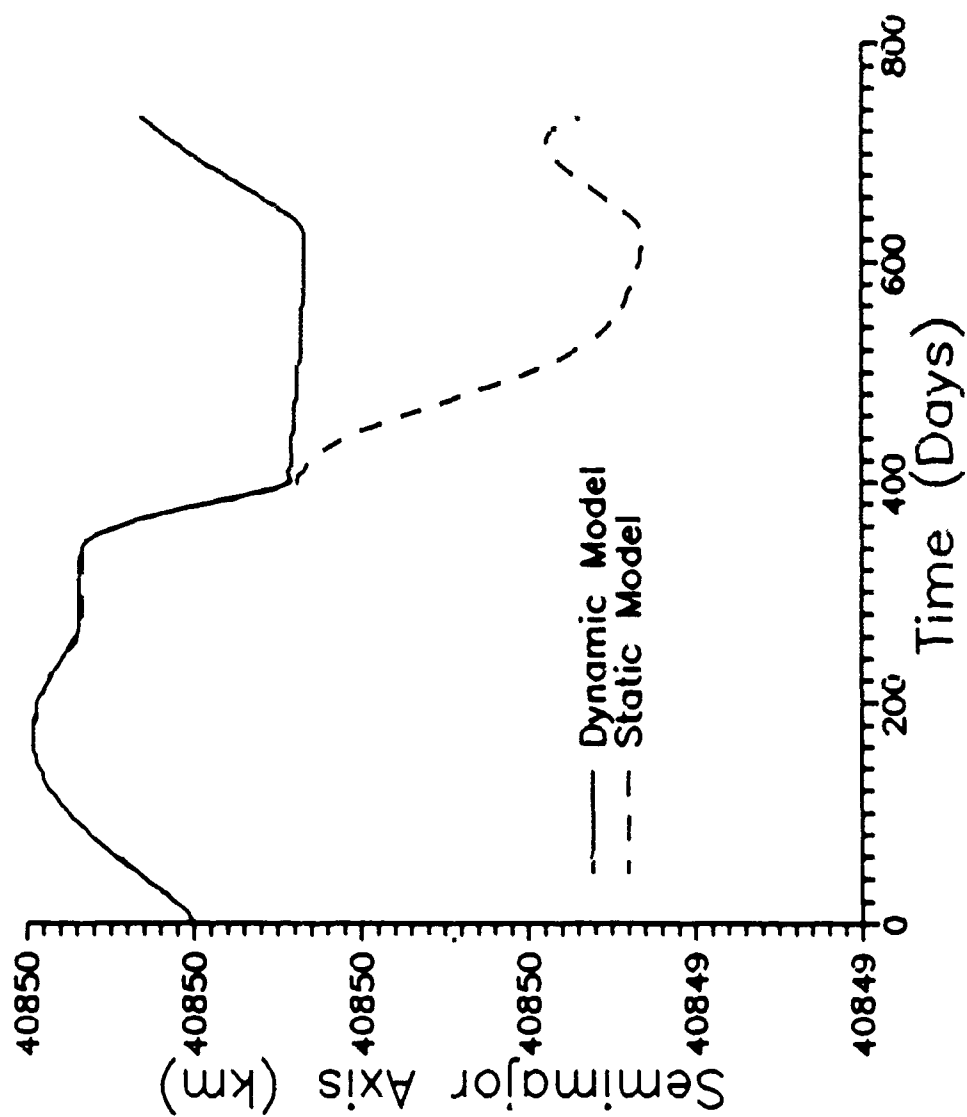
Fig. B.16: Semimajor Axis vs. Time (Case 7)
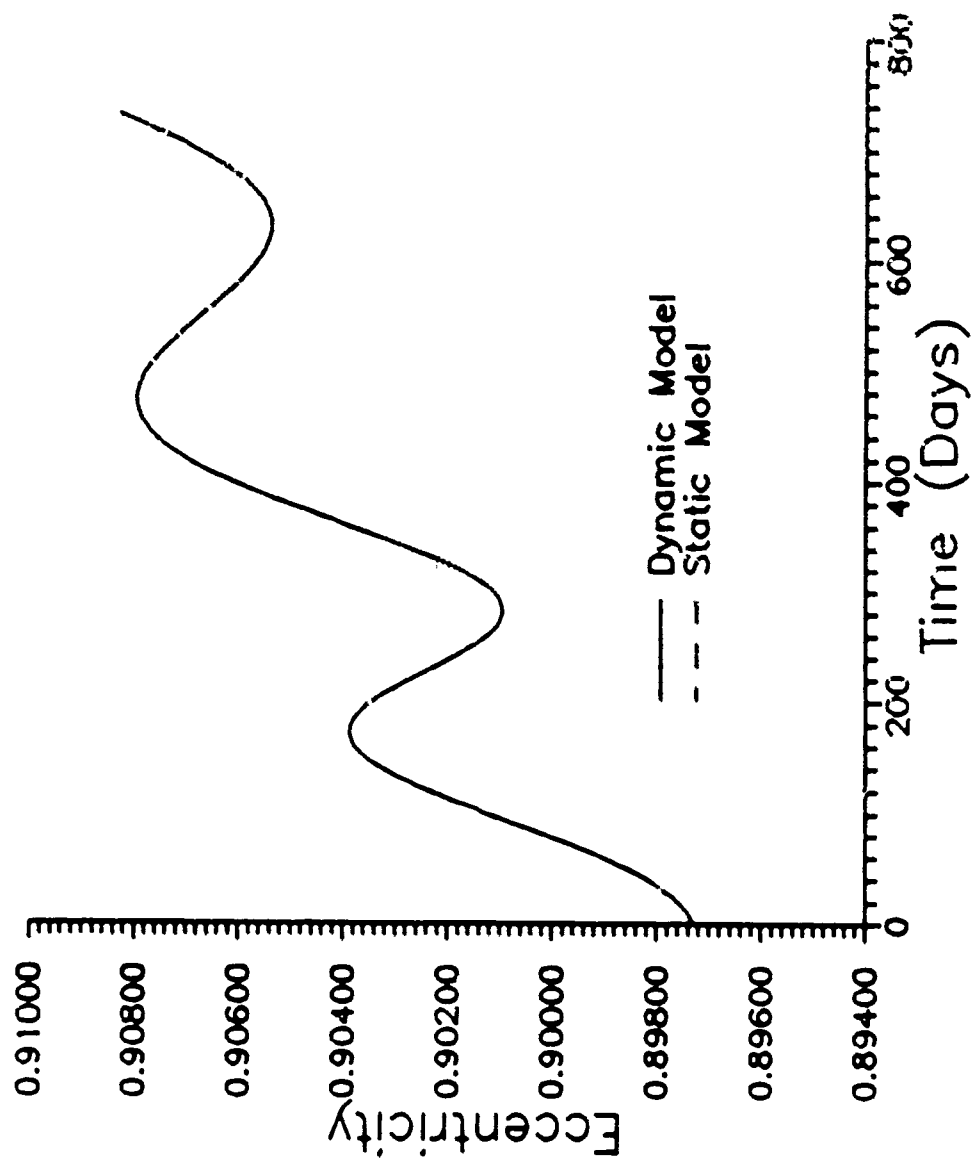
Fig. B.17: Eccentricity vs. Time (Case 7)

119
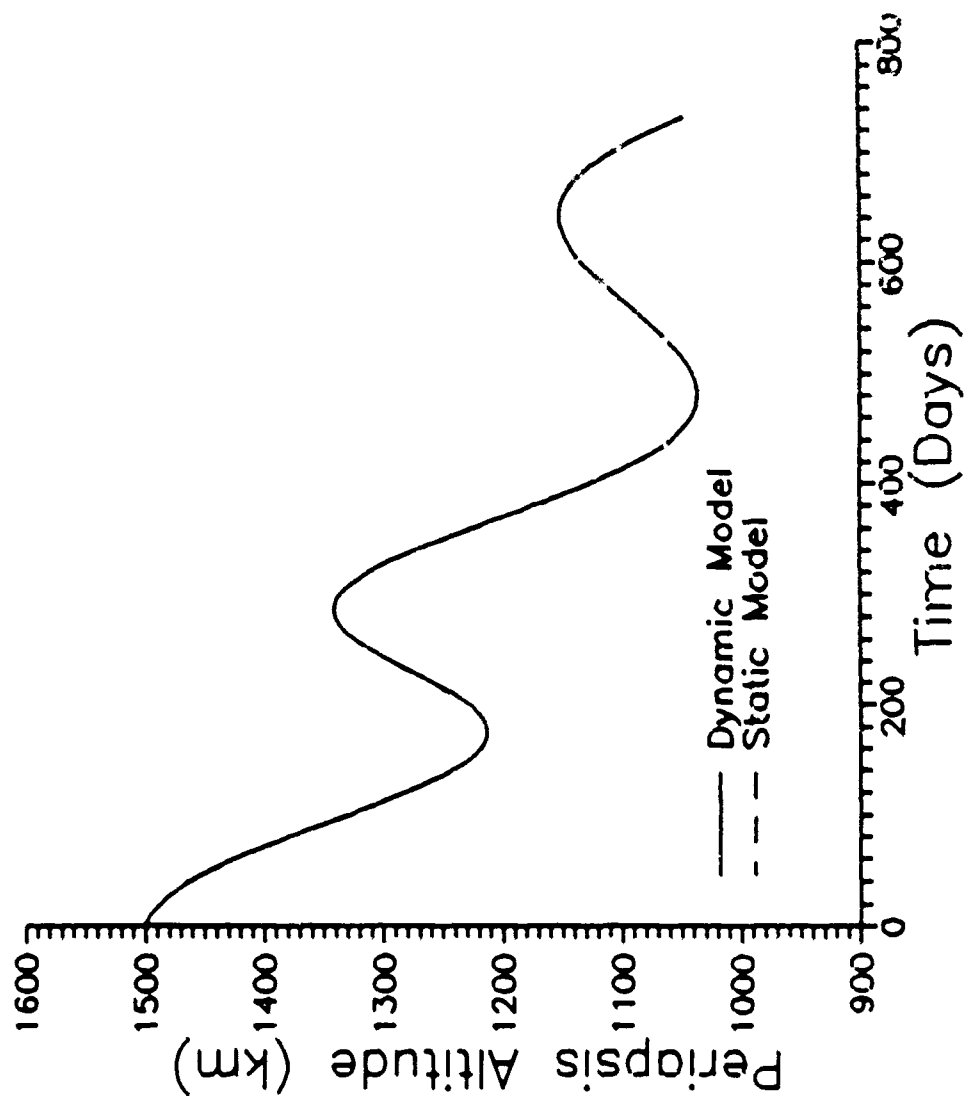
Fig. B.18: Periapsis Altitude vs. Time (Case 3)

— Dynamic Model
– – Static Model

Fig. B.19: Semimajor Axis vs. Time (Case 3)

408850

408850

408850

408850

408850

408850

408850

408850

nimajor Axis (km)

Dynamic Model
Static Model

Time (Days)

0

200

400

600

800
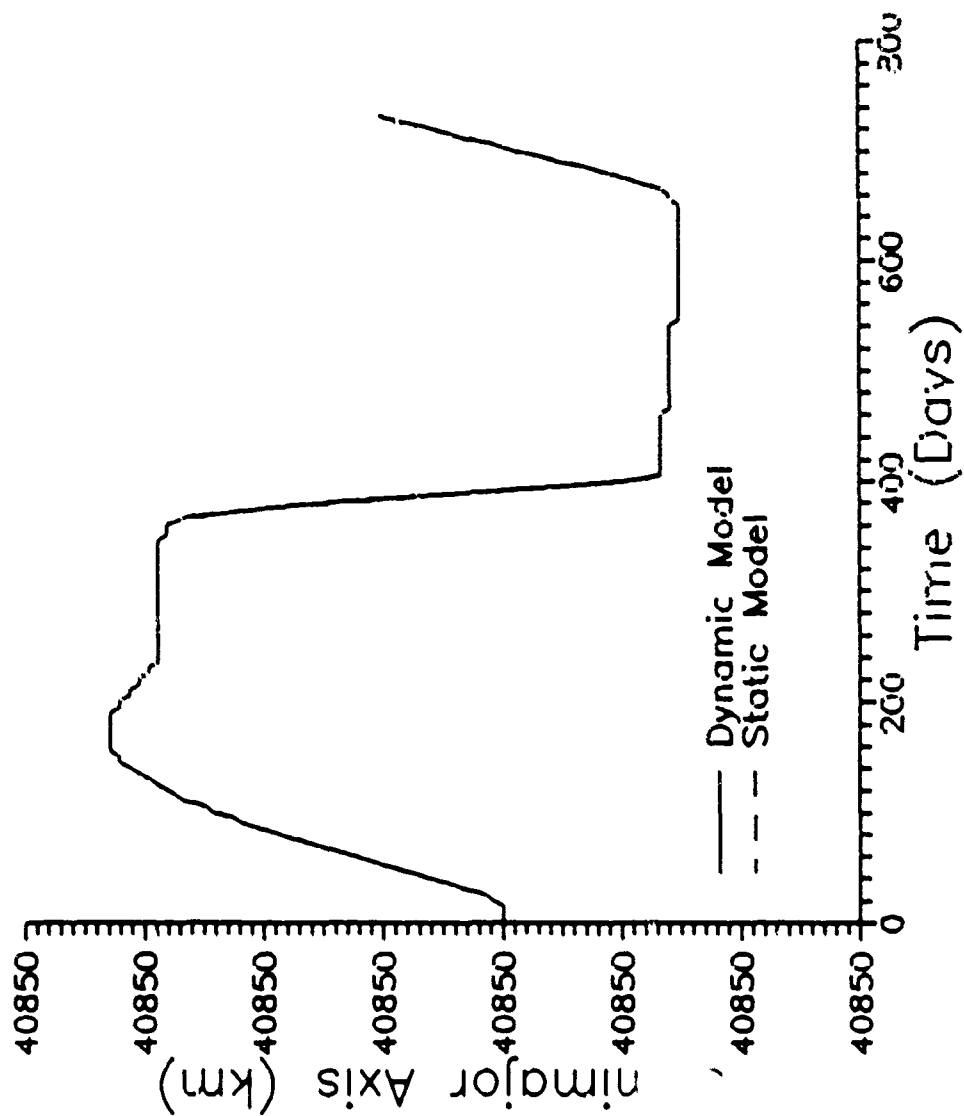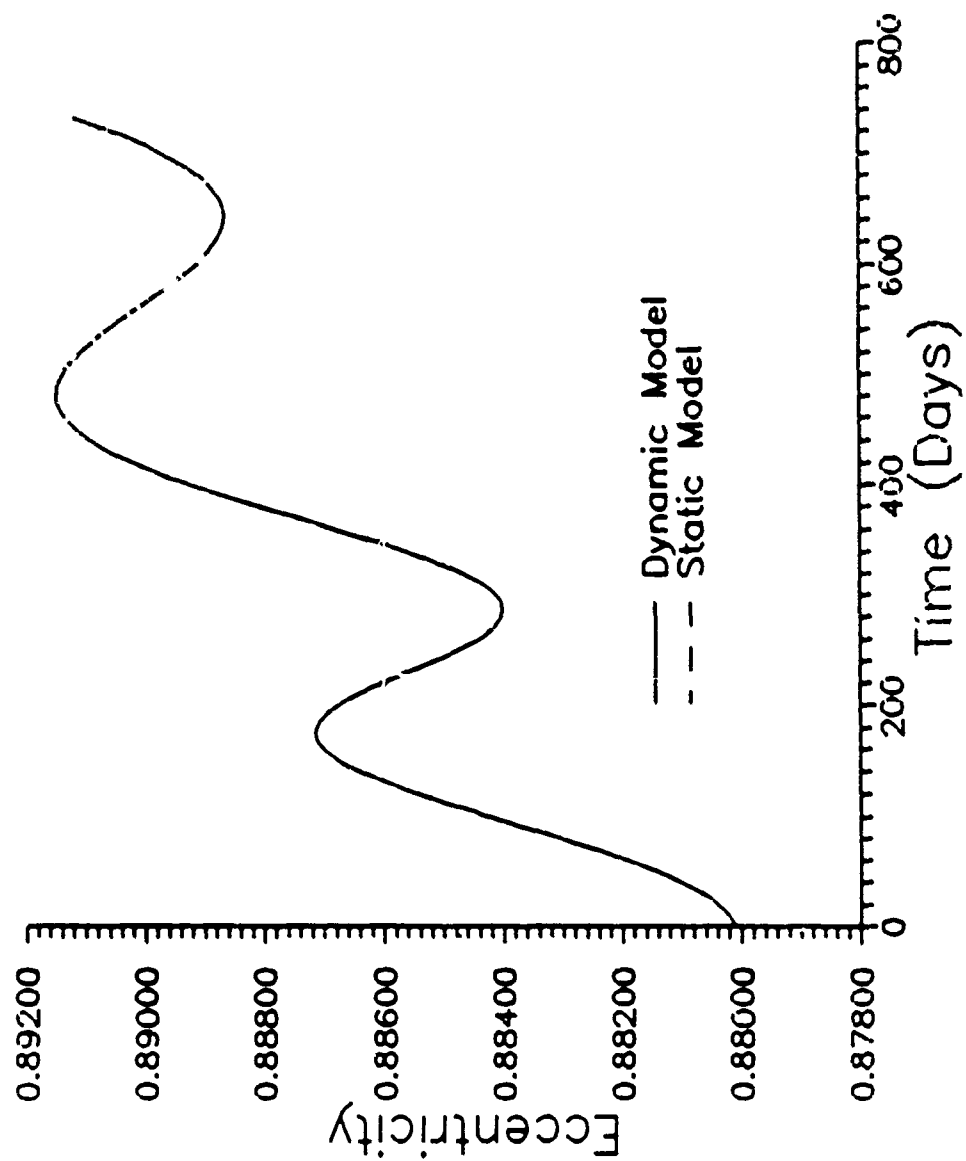
Fig. B.20: Eccentricity vs. Time (Case S)
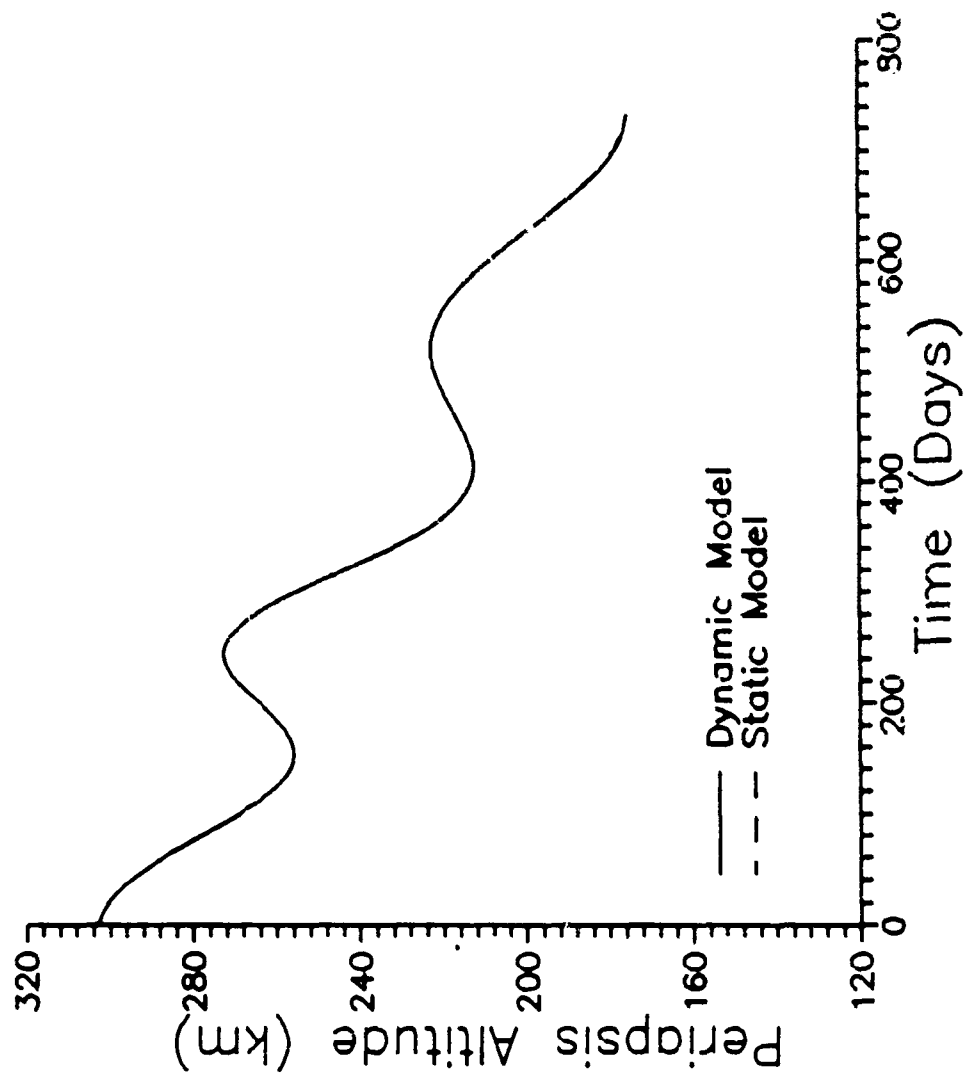
Fig. B.21: Periapsis Altitude vs. Time (Case 9)

123
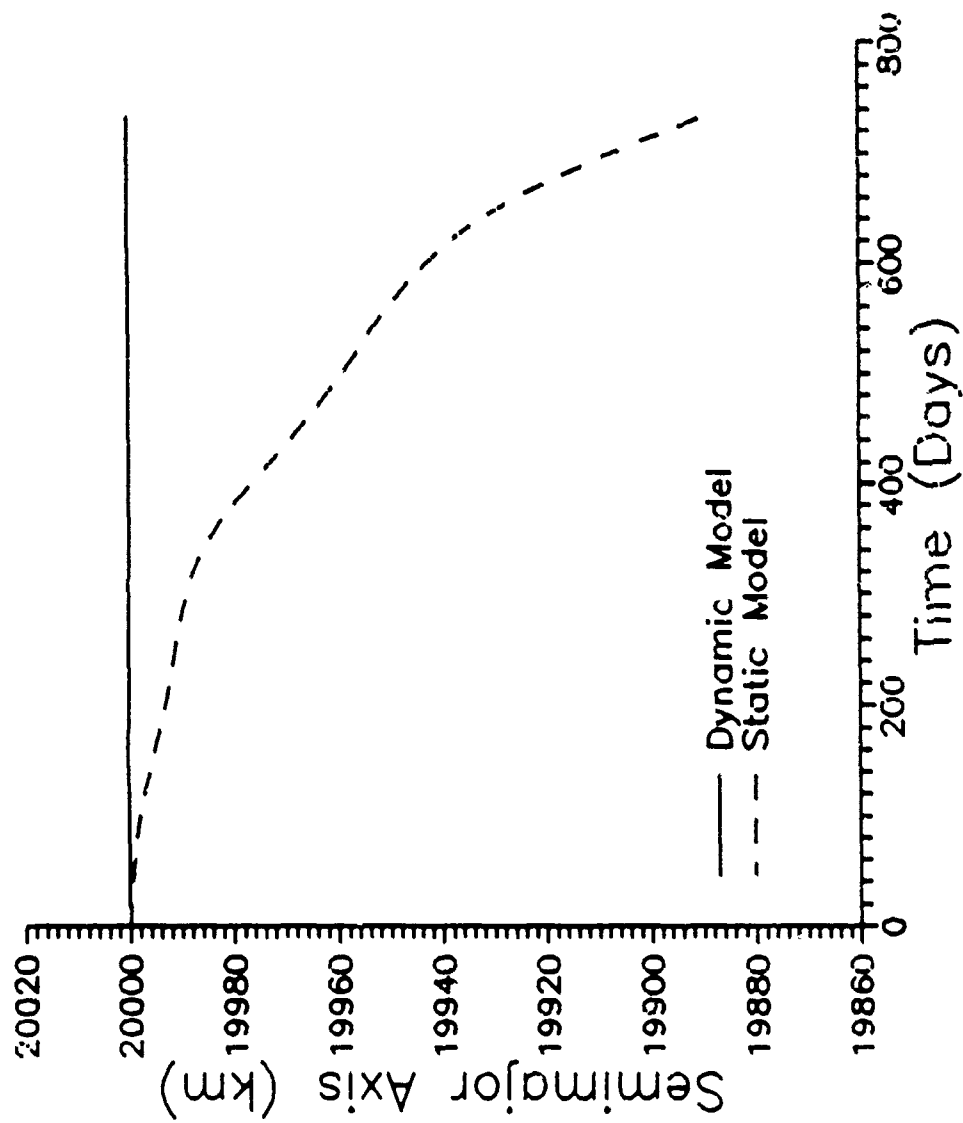
Fig. B.22: Semimajor Axis vs. Time (Case 9)

124

Fig. B.23: Eccentricity vs. Time (Case 9)

Time (Days)

Eccentricity

— Dynamic Model
-- Static Model
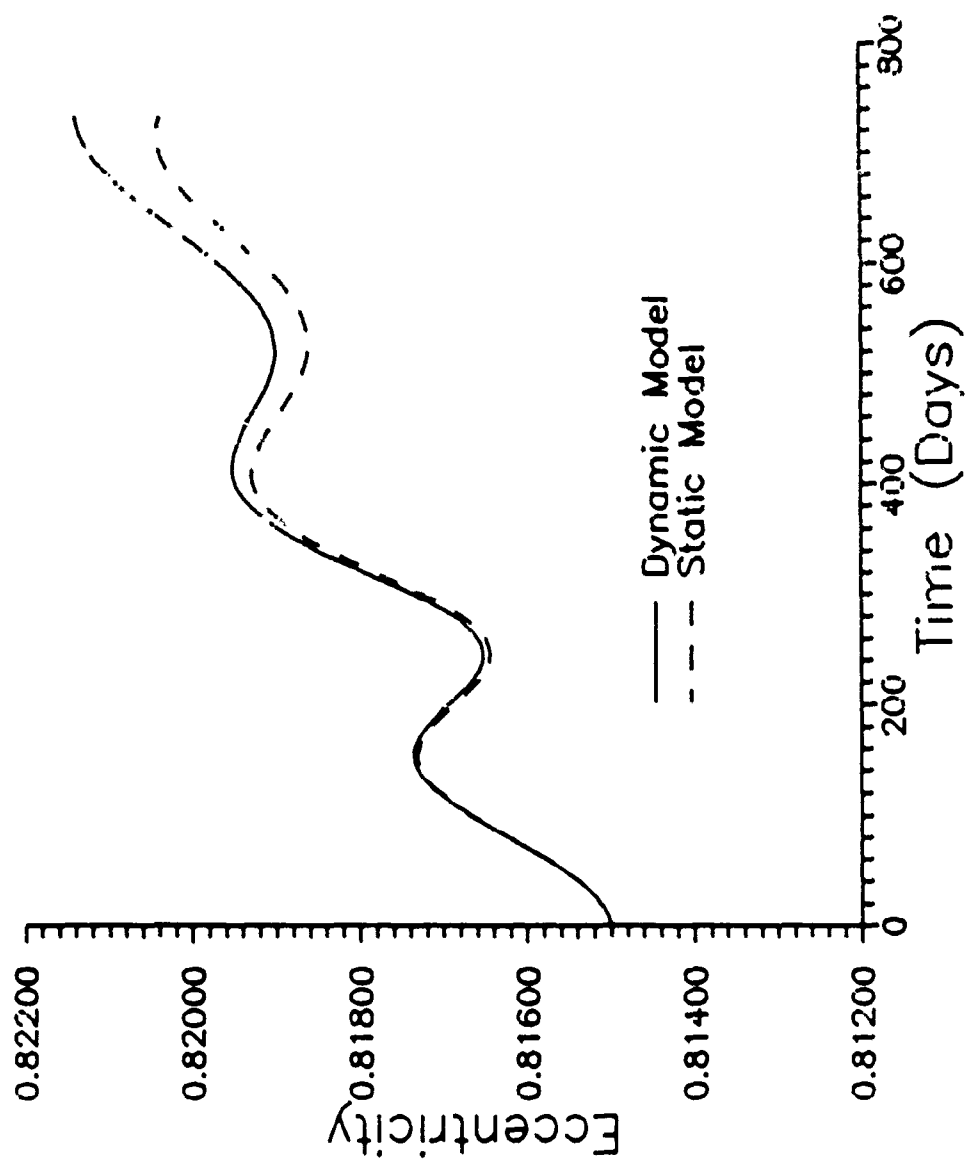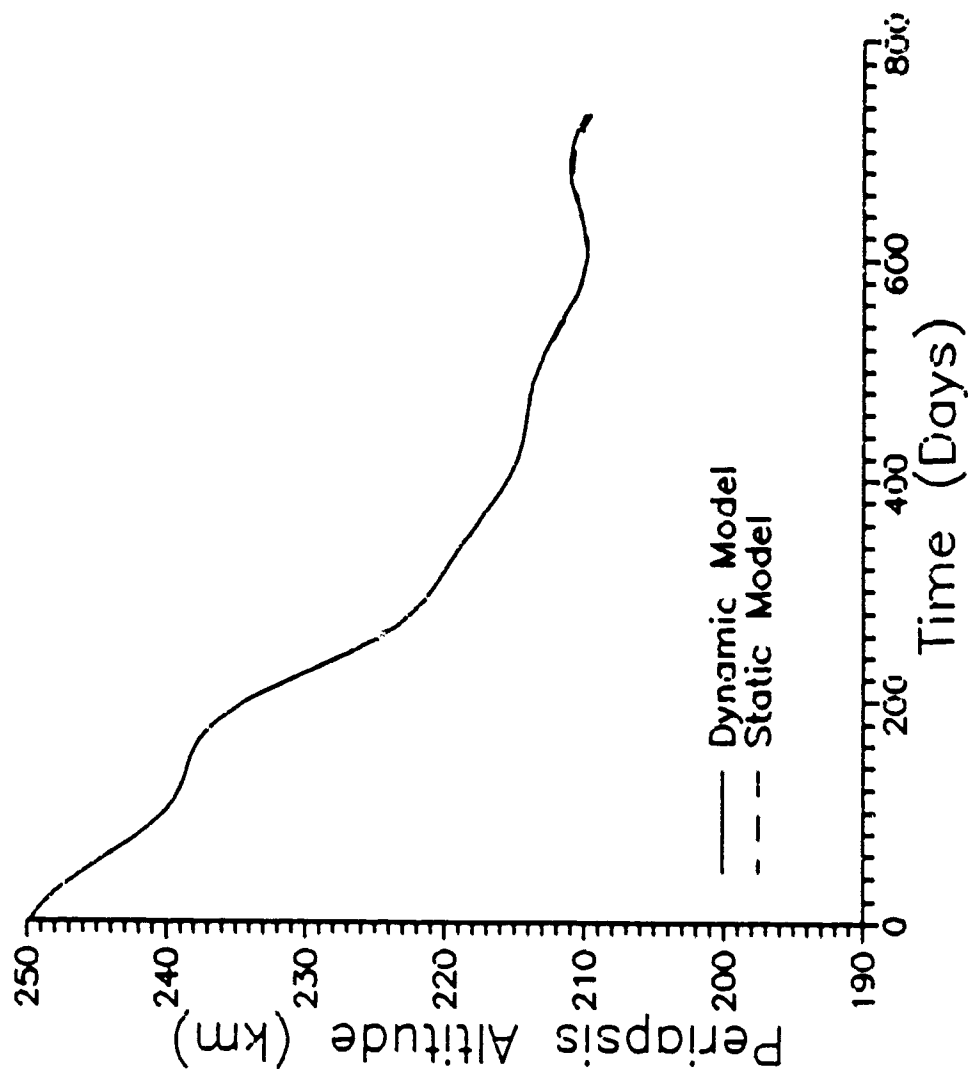
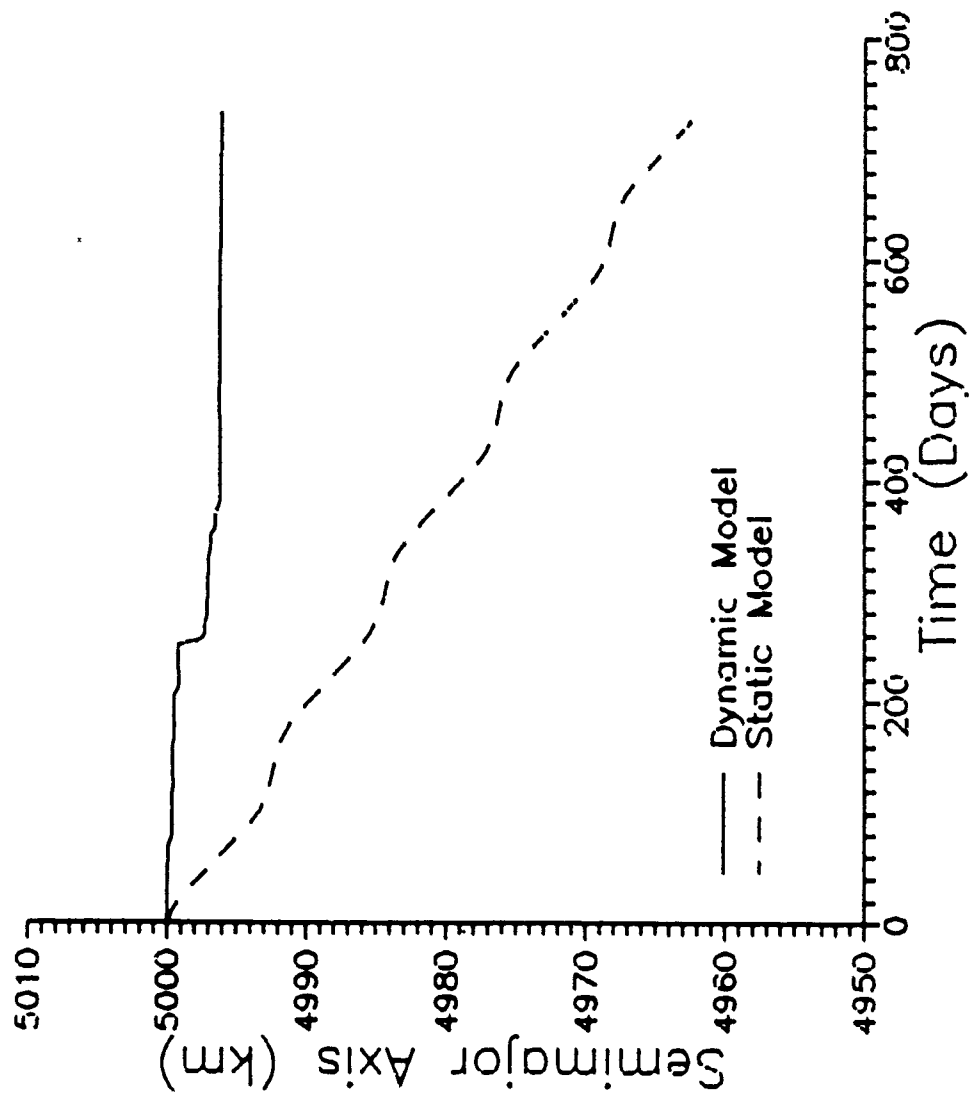Fig. B.24: Periapsis Altitude vs. Time (Case 10)
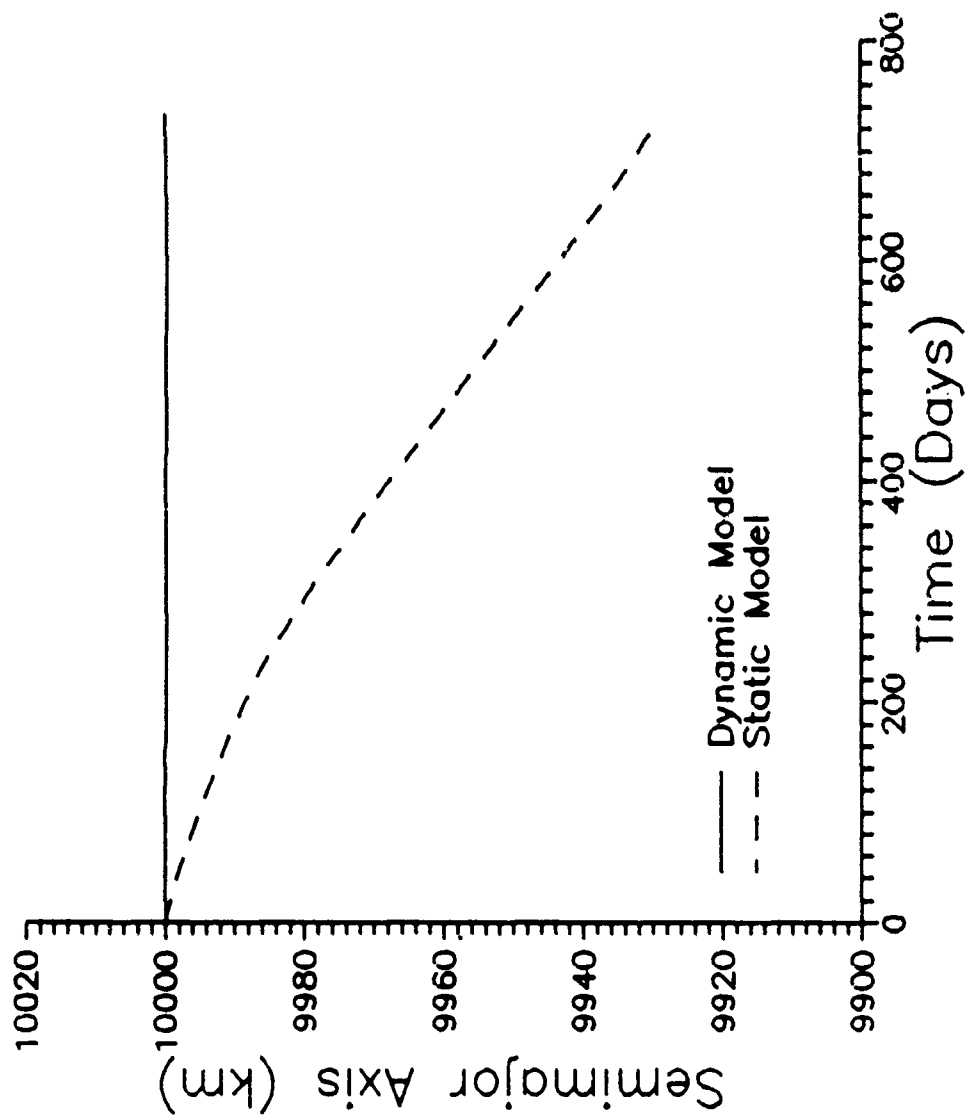
Fig. B.25: Semimajor Axis vs. Time (Case 10)
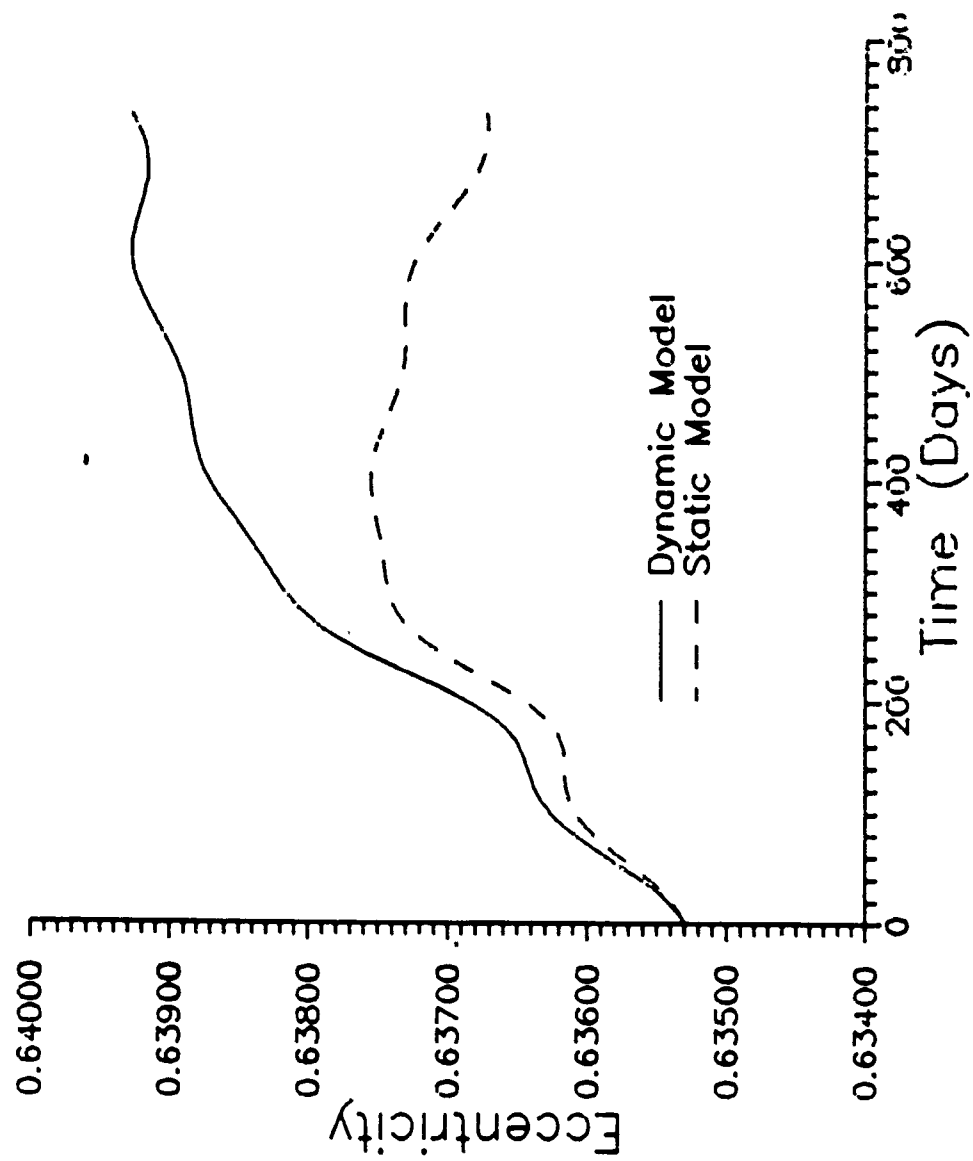
Fig. B.26: Eccentricity vs. Time (Case 10)

128
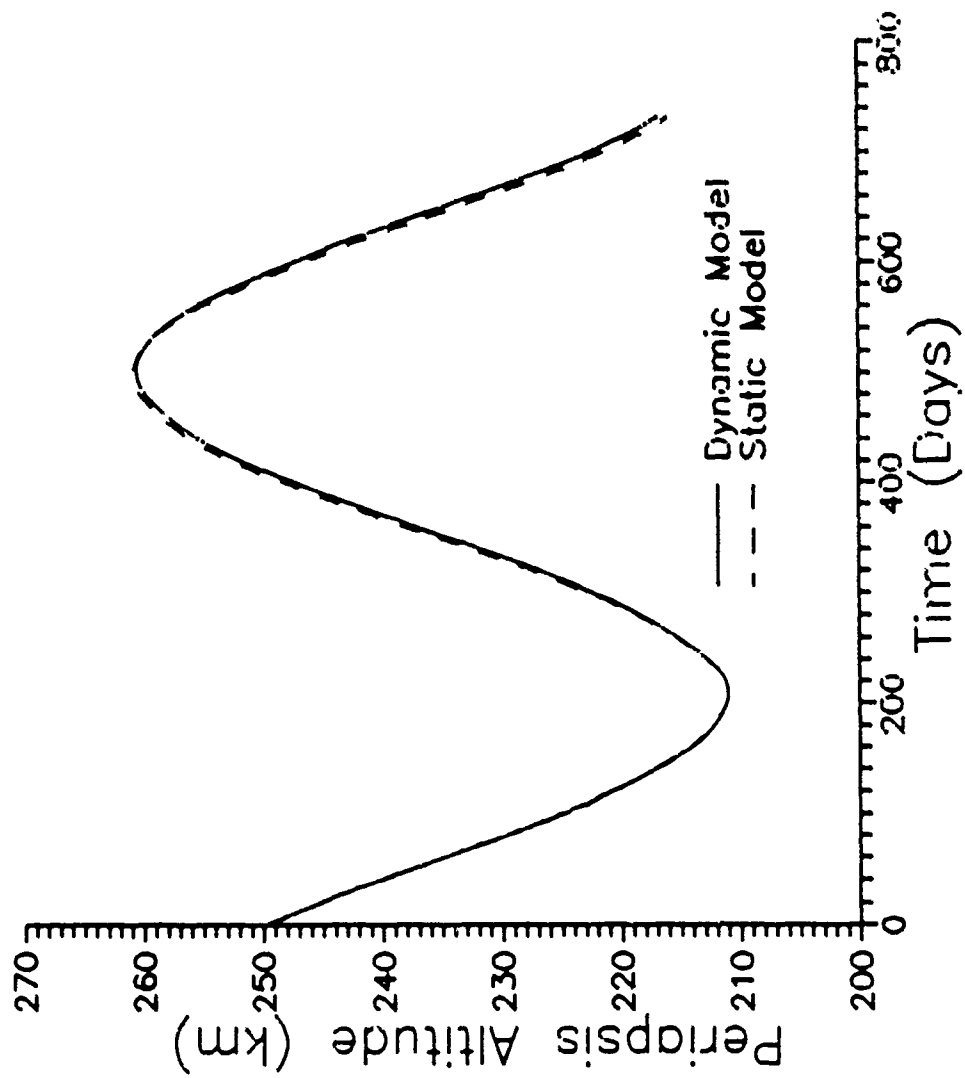
Fig. B.27: Periapsis Altitude vs. Time (Case 11)
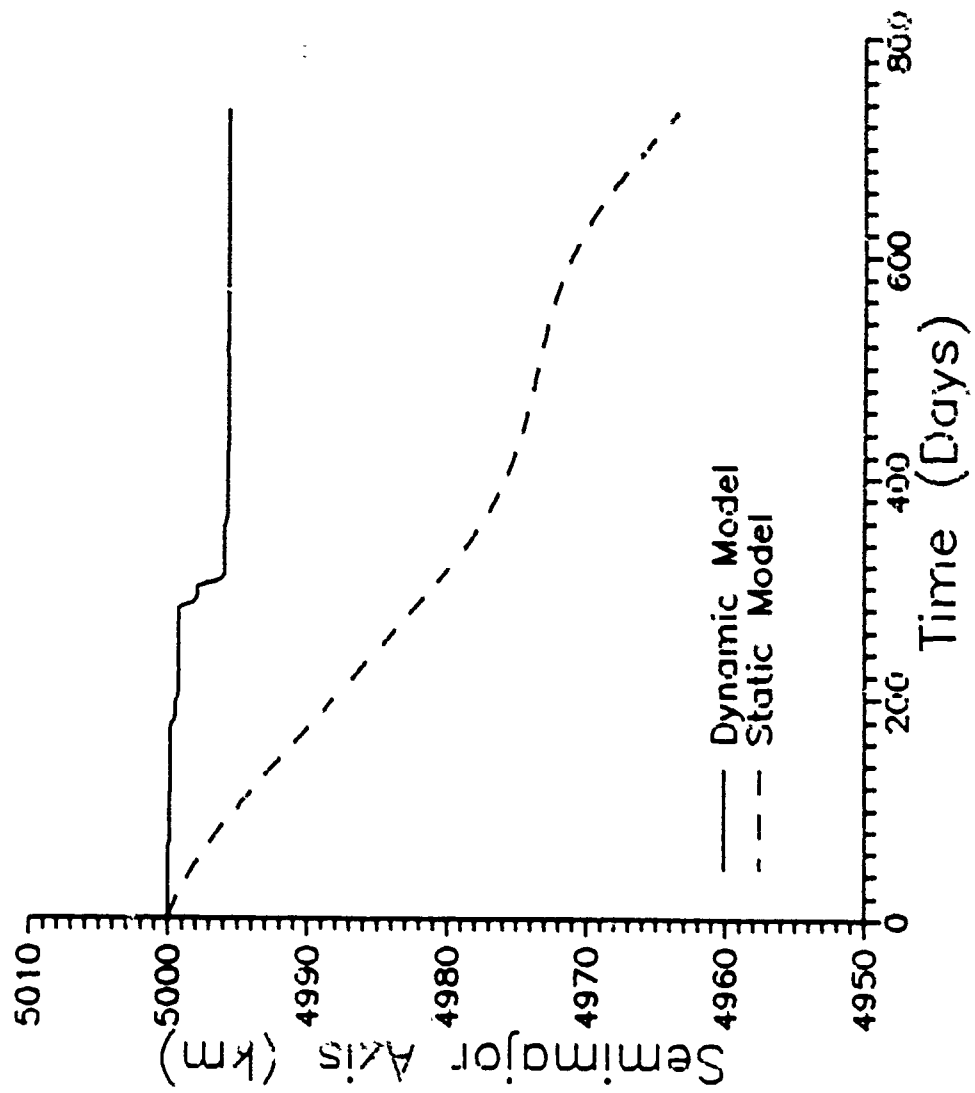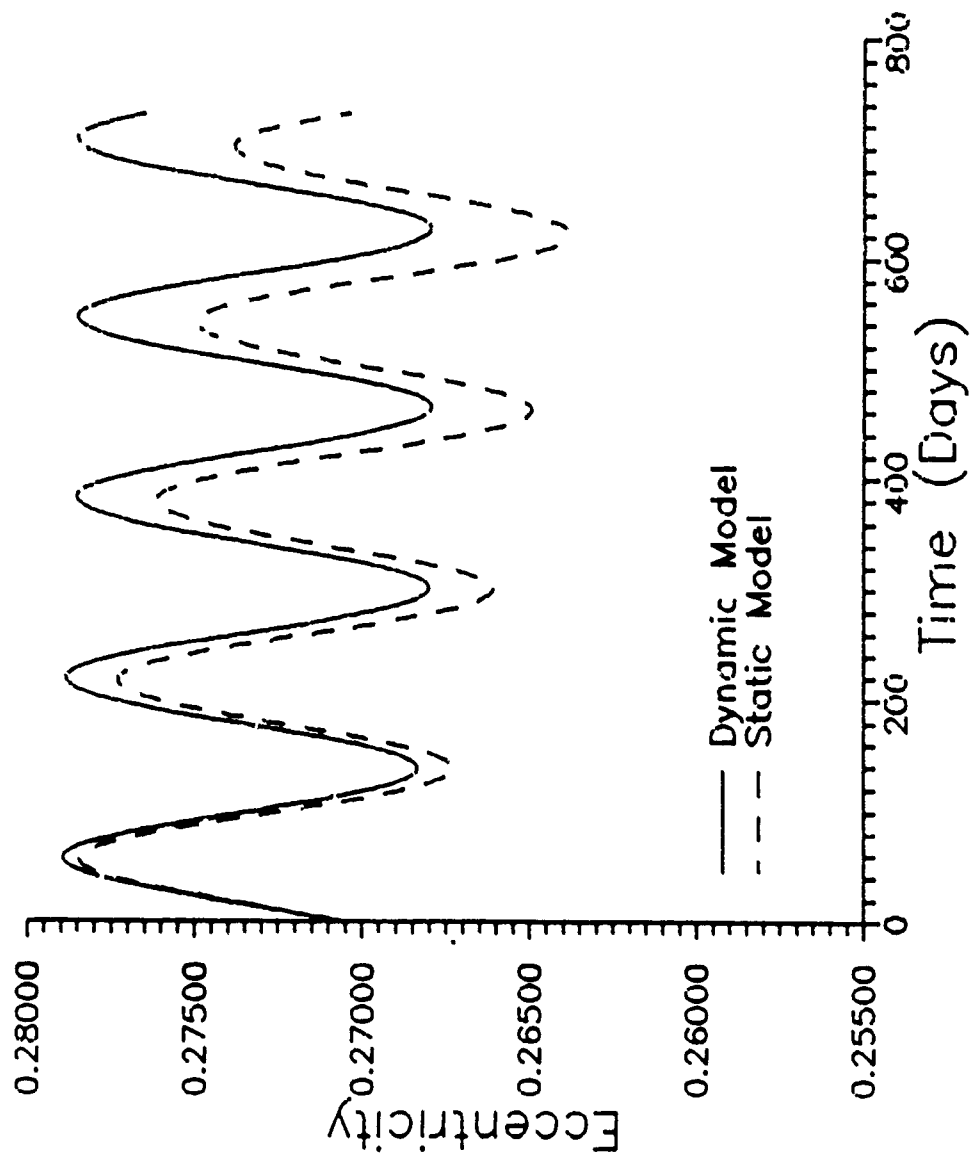
Fig. B.28: Semimajor Axis vs. Time (Case 11)
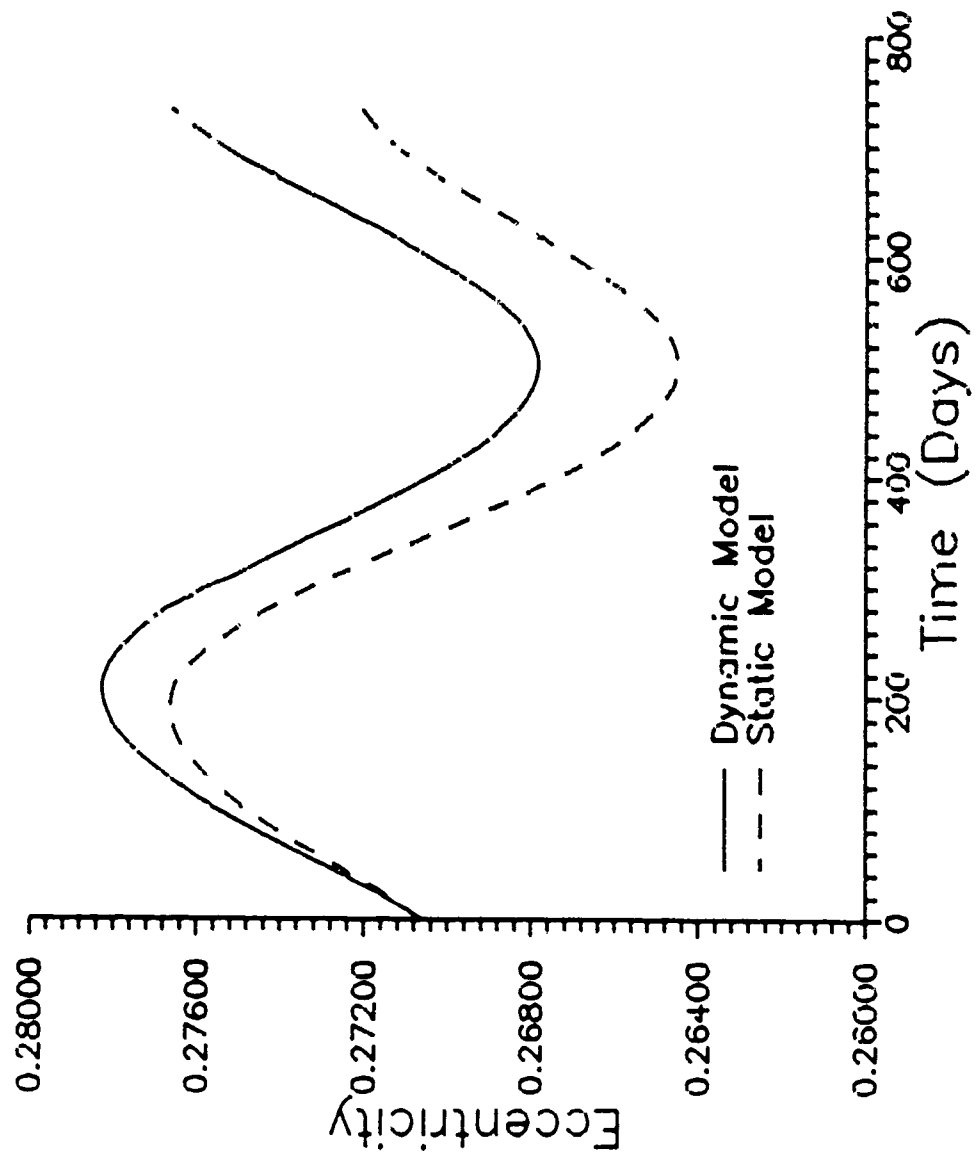
Fig. B.29: Eccentricity vs. Time (Case 11)

Fig. B.30: Periapsis Altitude vs. Time (Case 13)
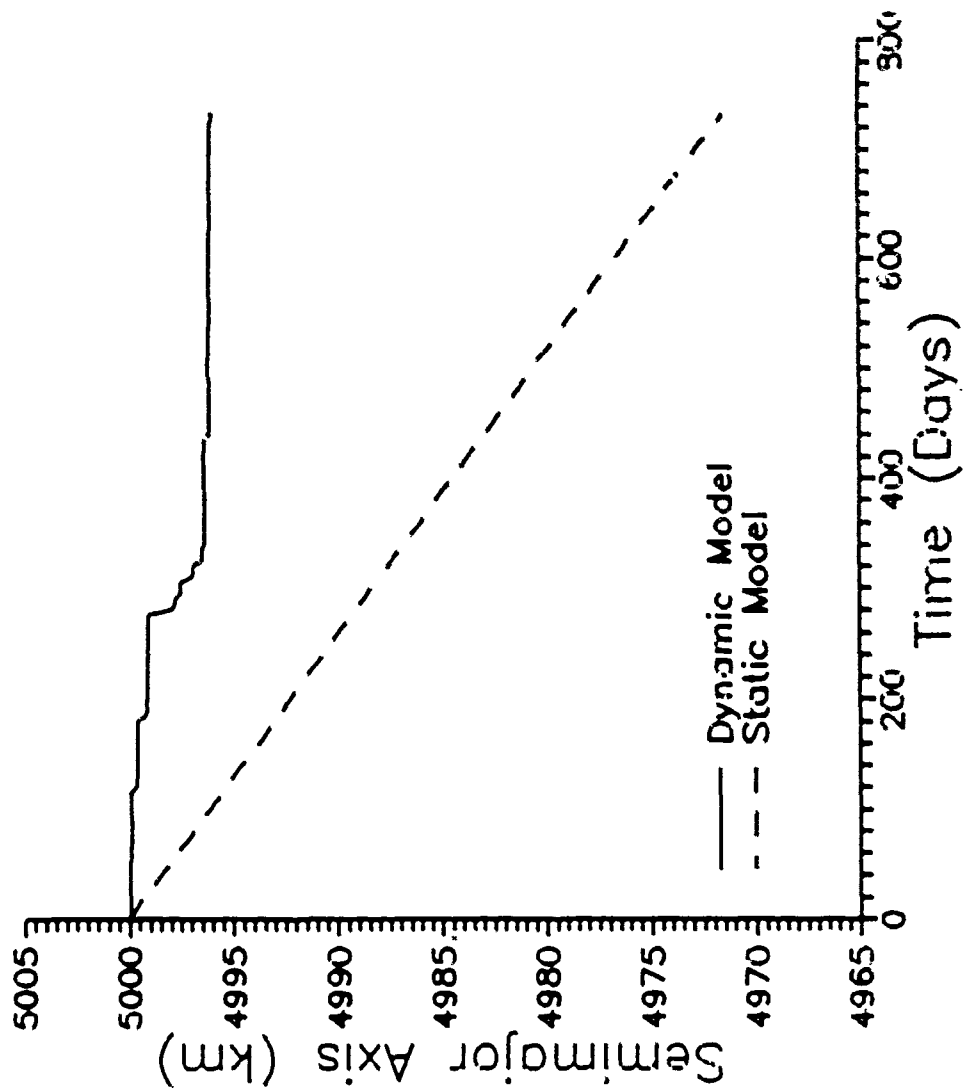
Fig. B.31: Semimajor Axis vs. Time (Case 12)

133
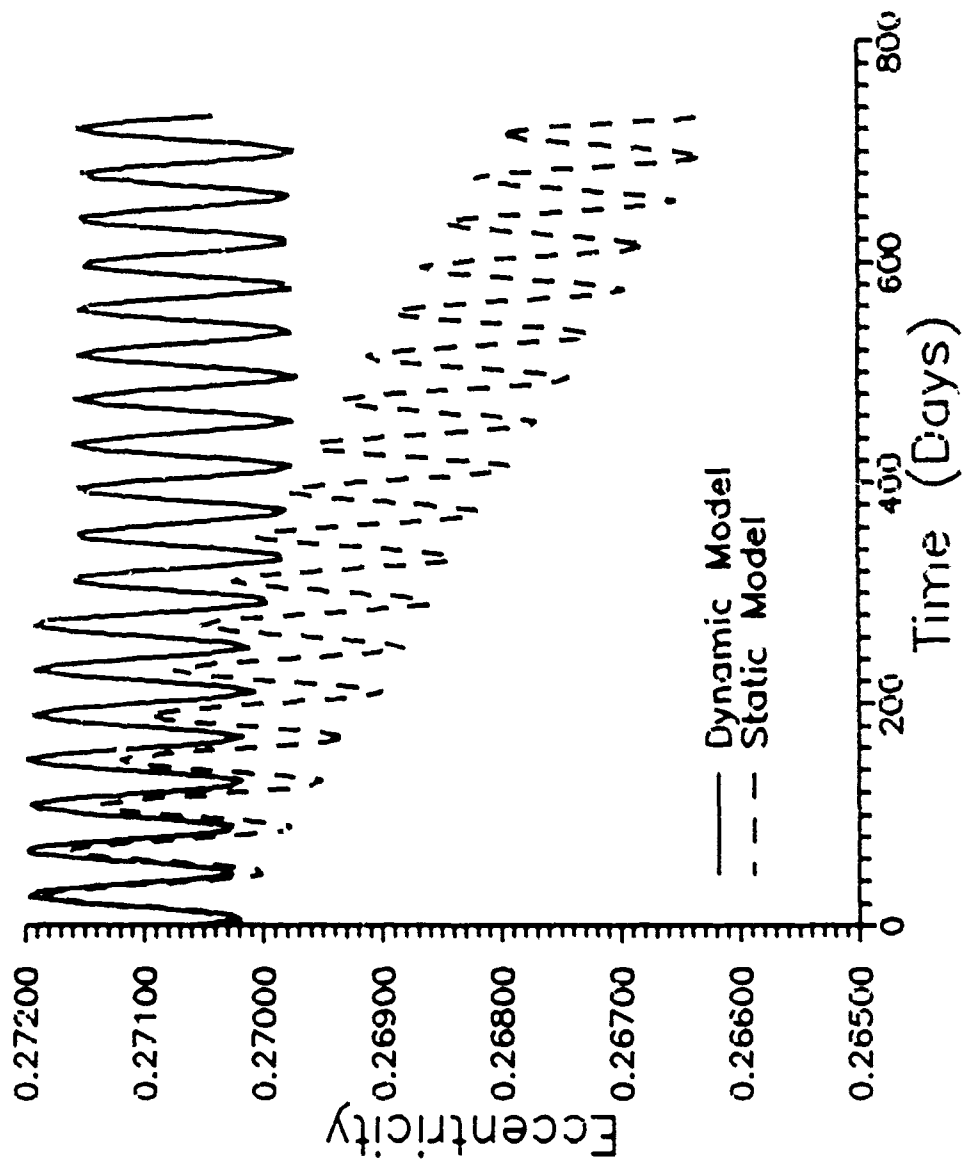
Fig. B.32: Eccentricity vs. Time (Case 12)

134
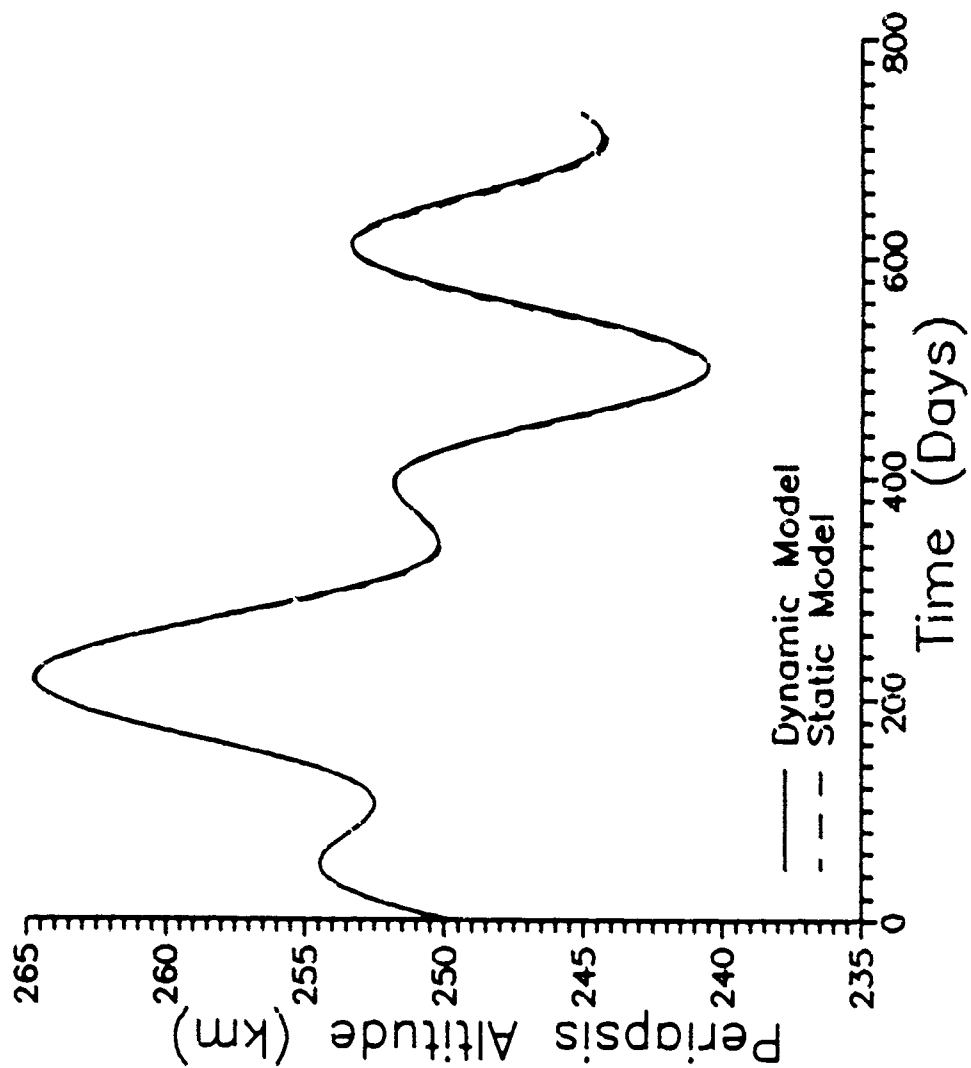
Fig. B.33: Periapsis Altitude vs. Time (Case 13)

Fig. B.34: Semimajor Axis vs. Time (Case 13)

Fig. B.35: Eccentricity vs. Time (Case 13)

Fig. B.36: Periapsis Altitude vs. Time (Case 14)
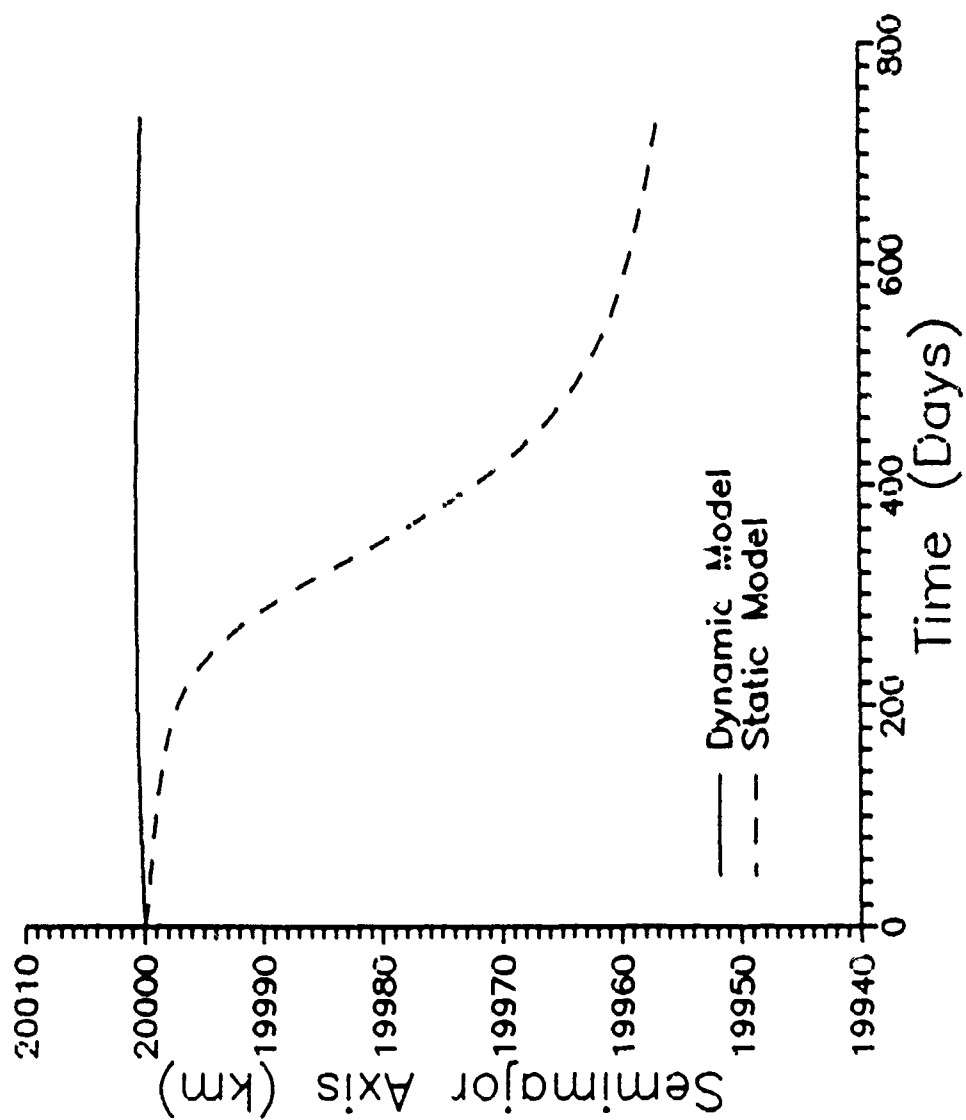
Fig. B.37: Semimajor Axis vs. Time (Case 14)
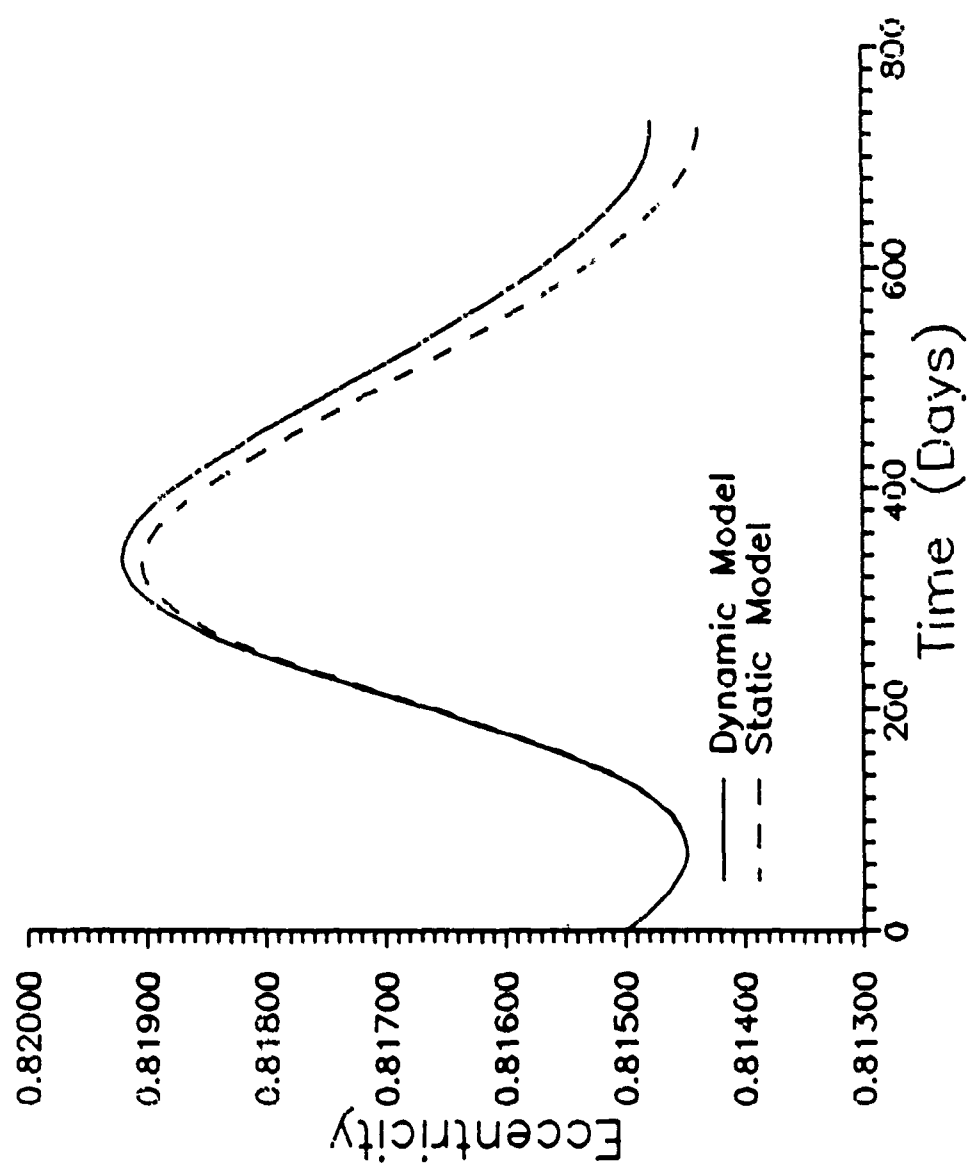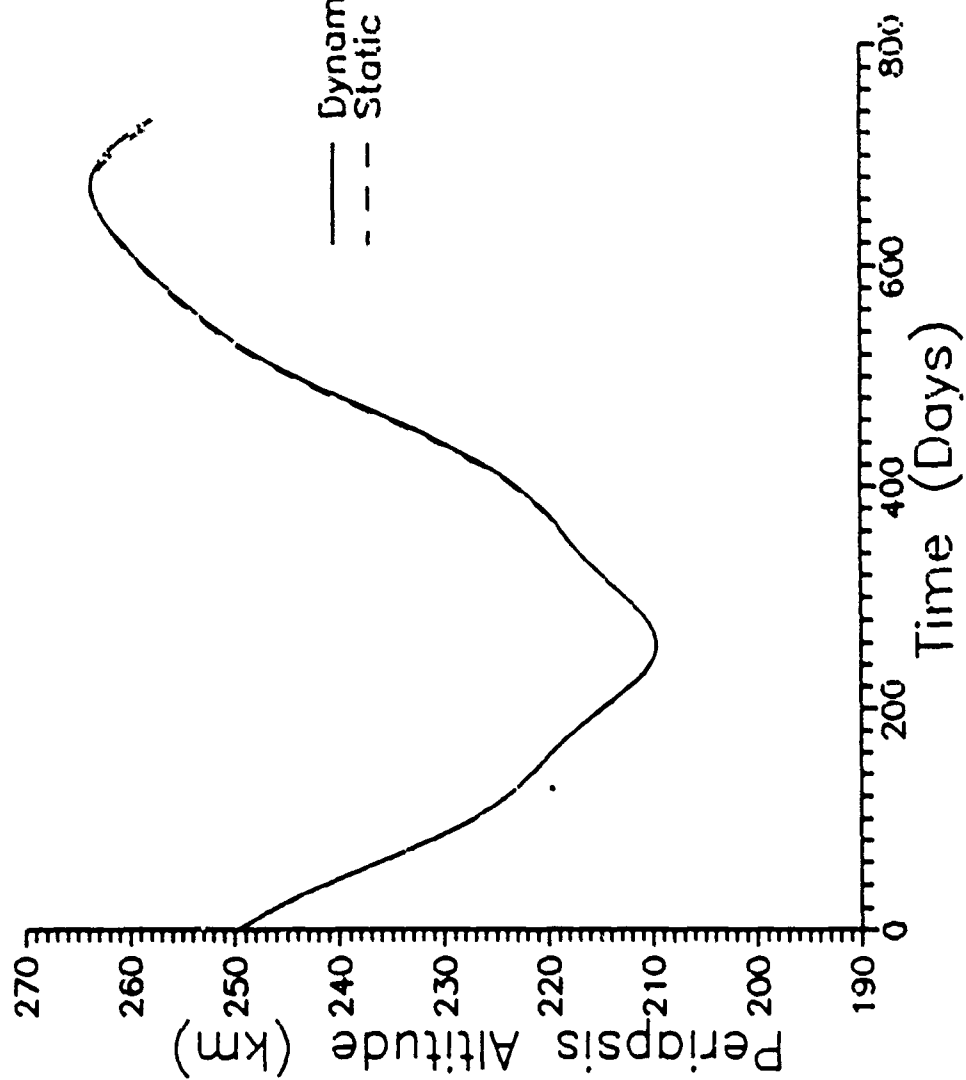
Fig. B.38: Eccentricity vs. Time (Case 14)
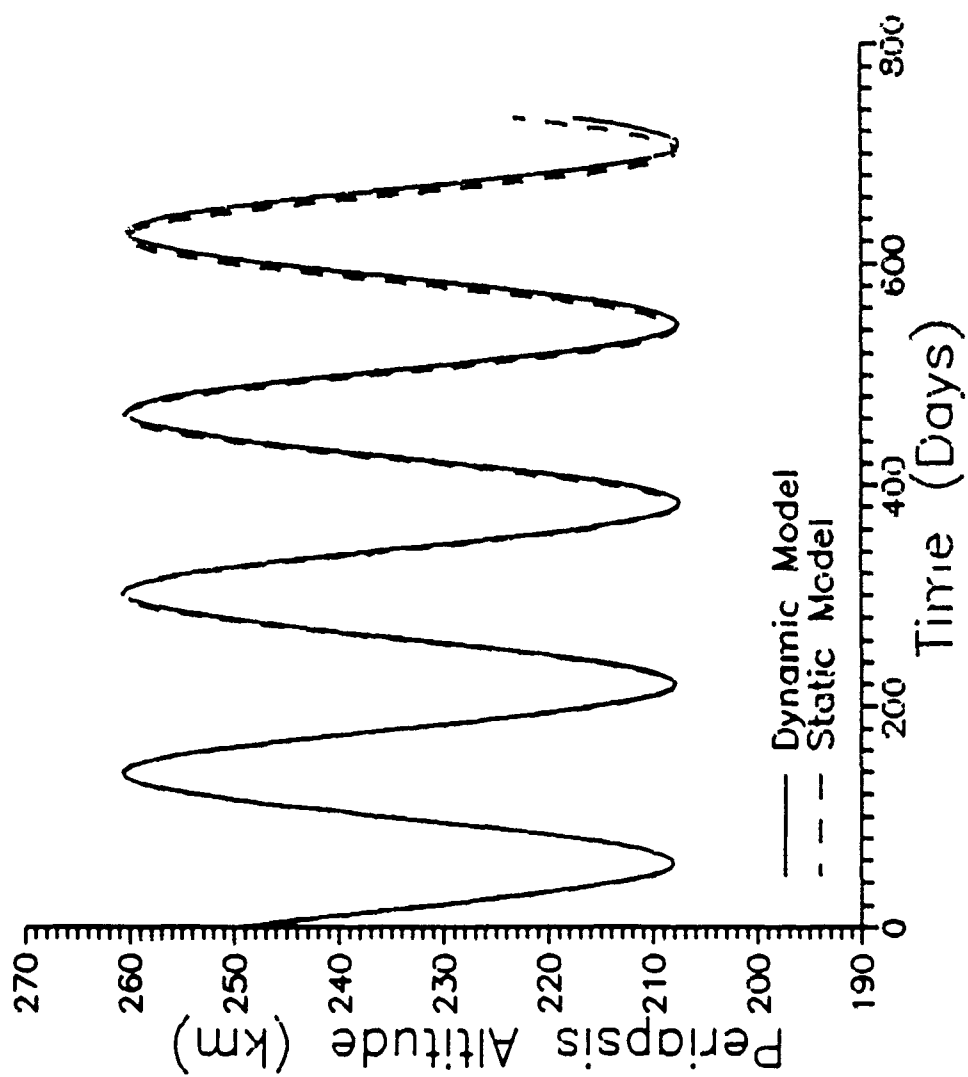
Fig. B.39: Periapsis Altitude vs. Time (Case 15)

Fig. B.40: Semimajor Axis vs. Time (Case 15)

Fig. B.41: Eccentricity vs. Time (Case 15)
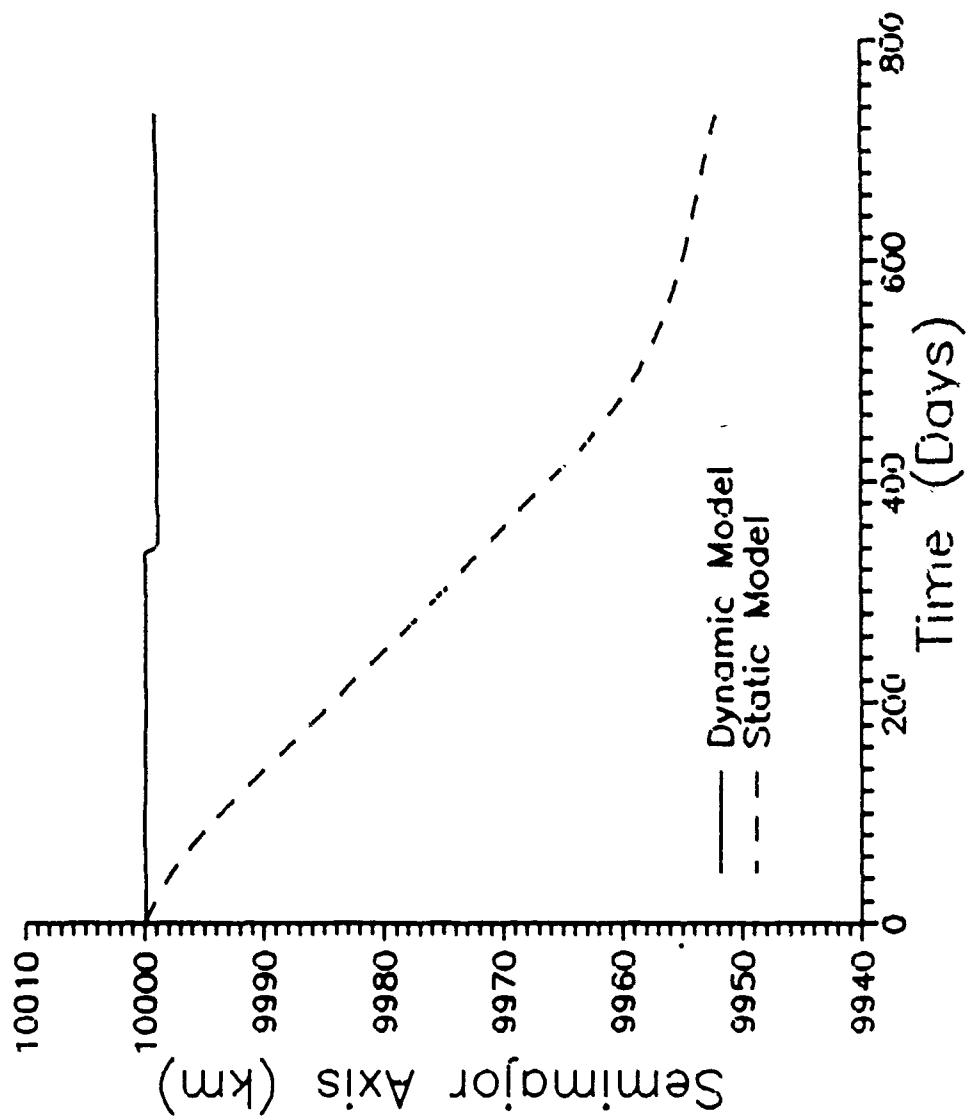
Fig. B.42: Periapsis Altitude vs. Time (Case 16)

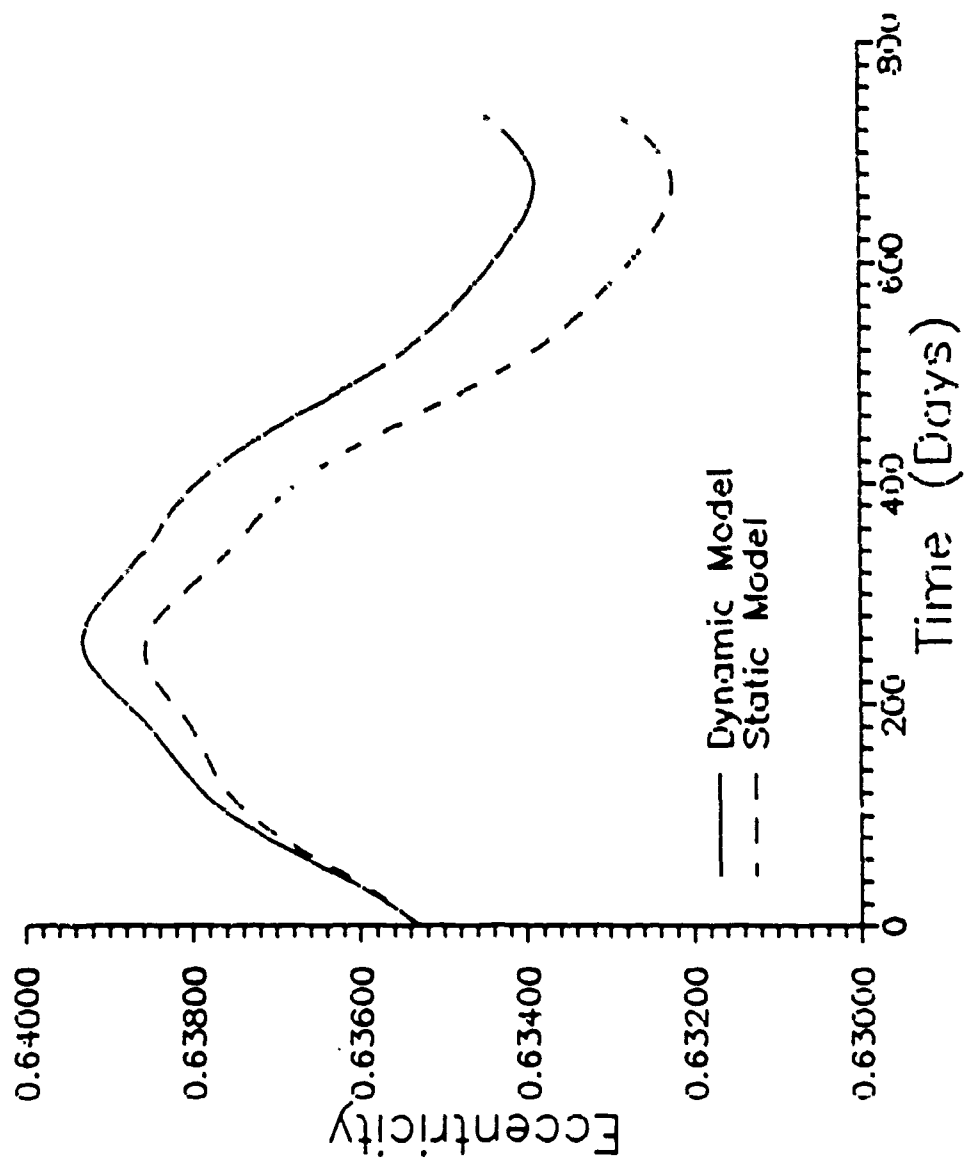144

Fig. B.43: Semimajor Axis vs. Time (Case 16)

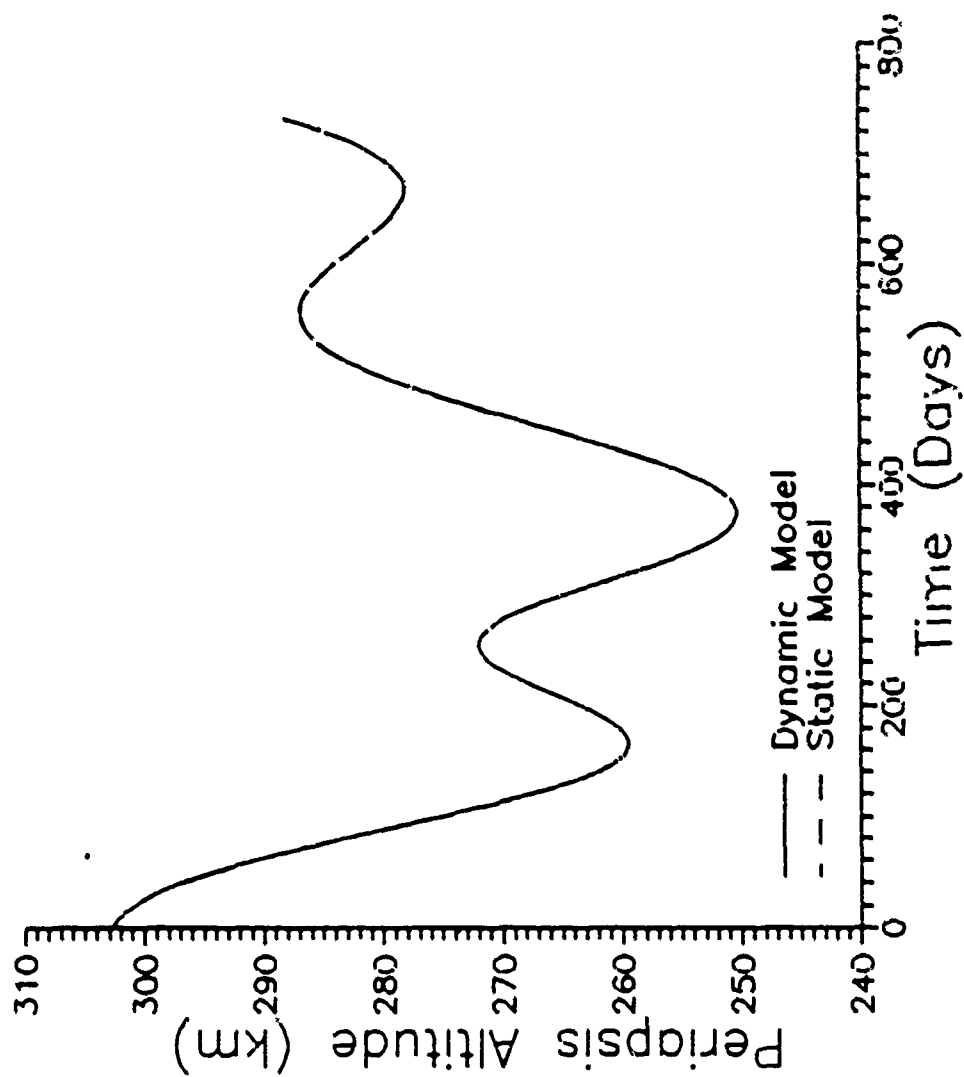Fig. B.44: Eccentricity vs. Time (Case 16)

Fig. B.45: Periapsis Altitude vs. Time (Case 17)

147

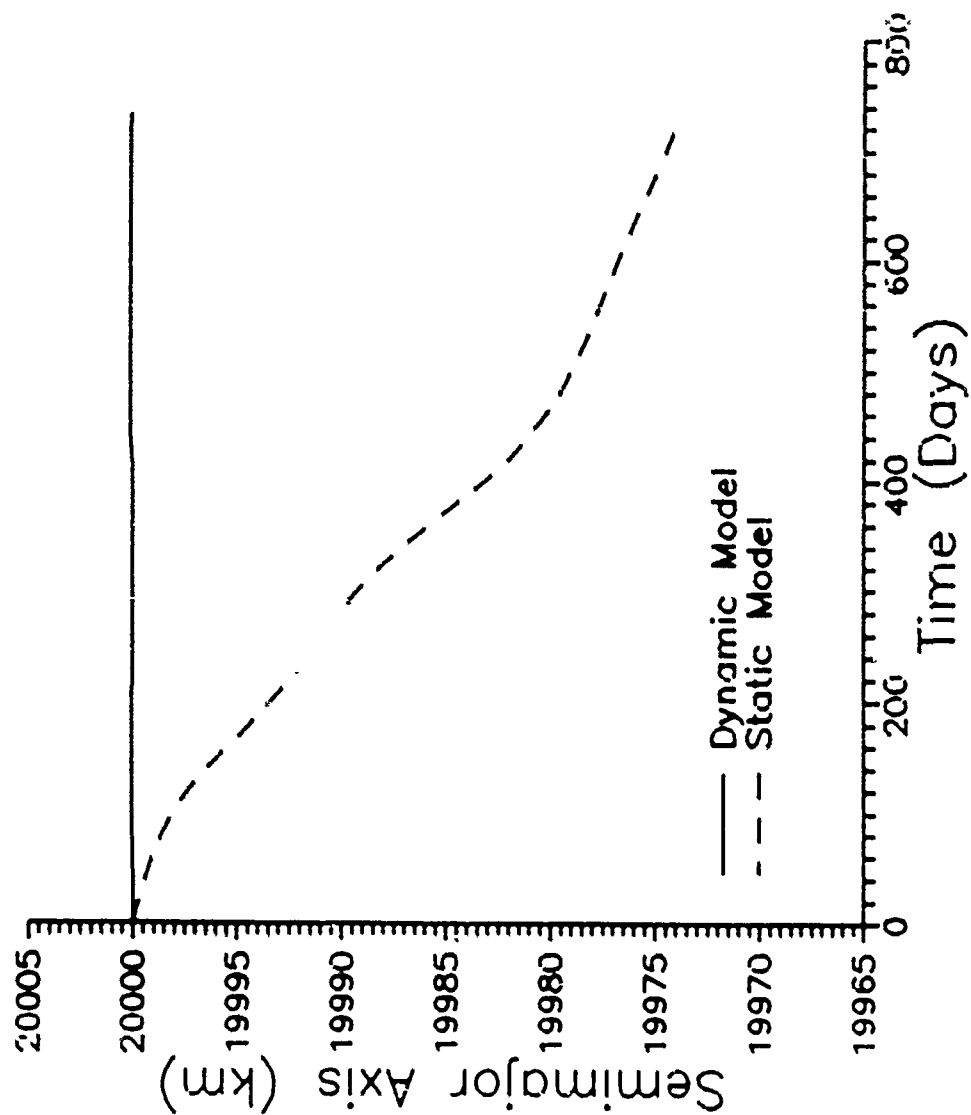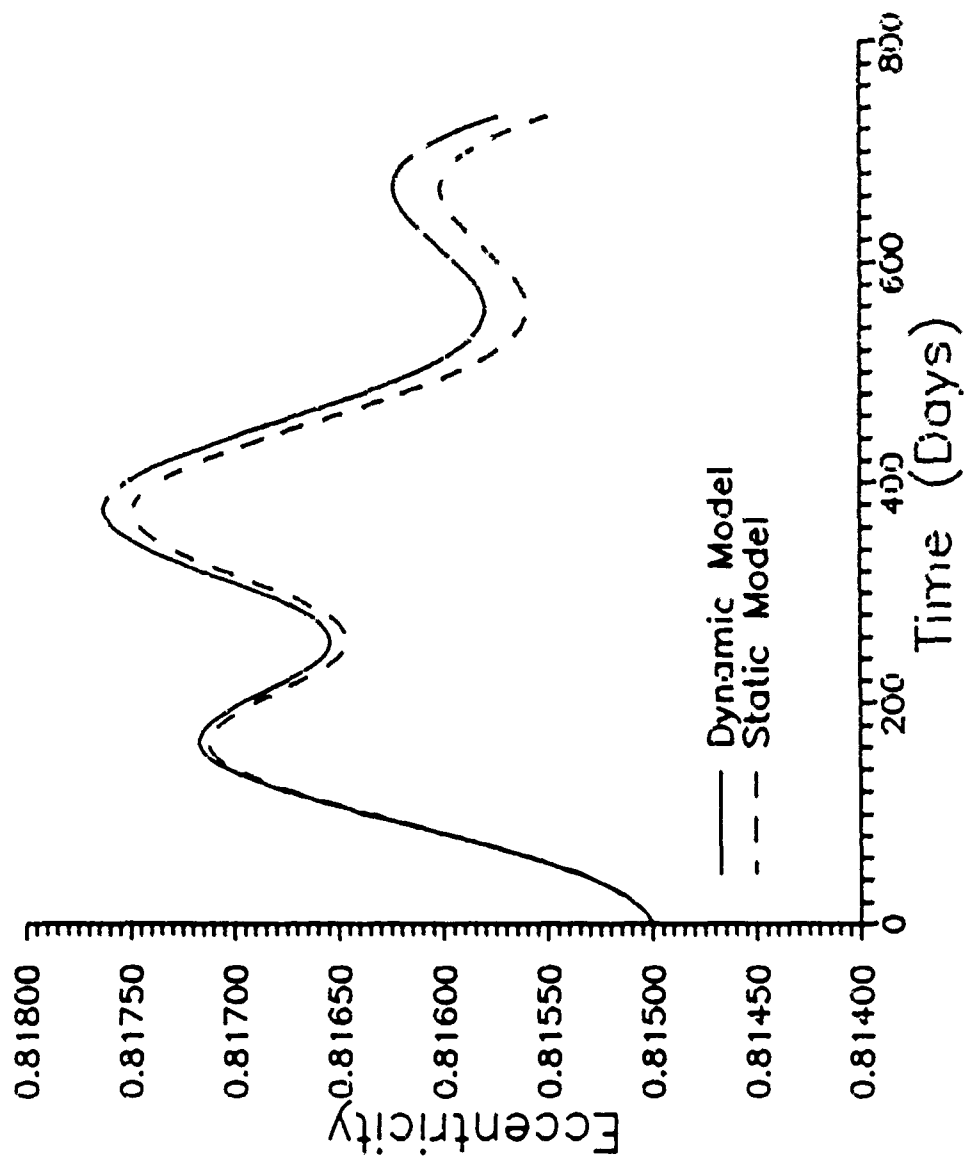Fig. B.46: Semimajor Axis vs. Time (Case 17)

148

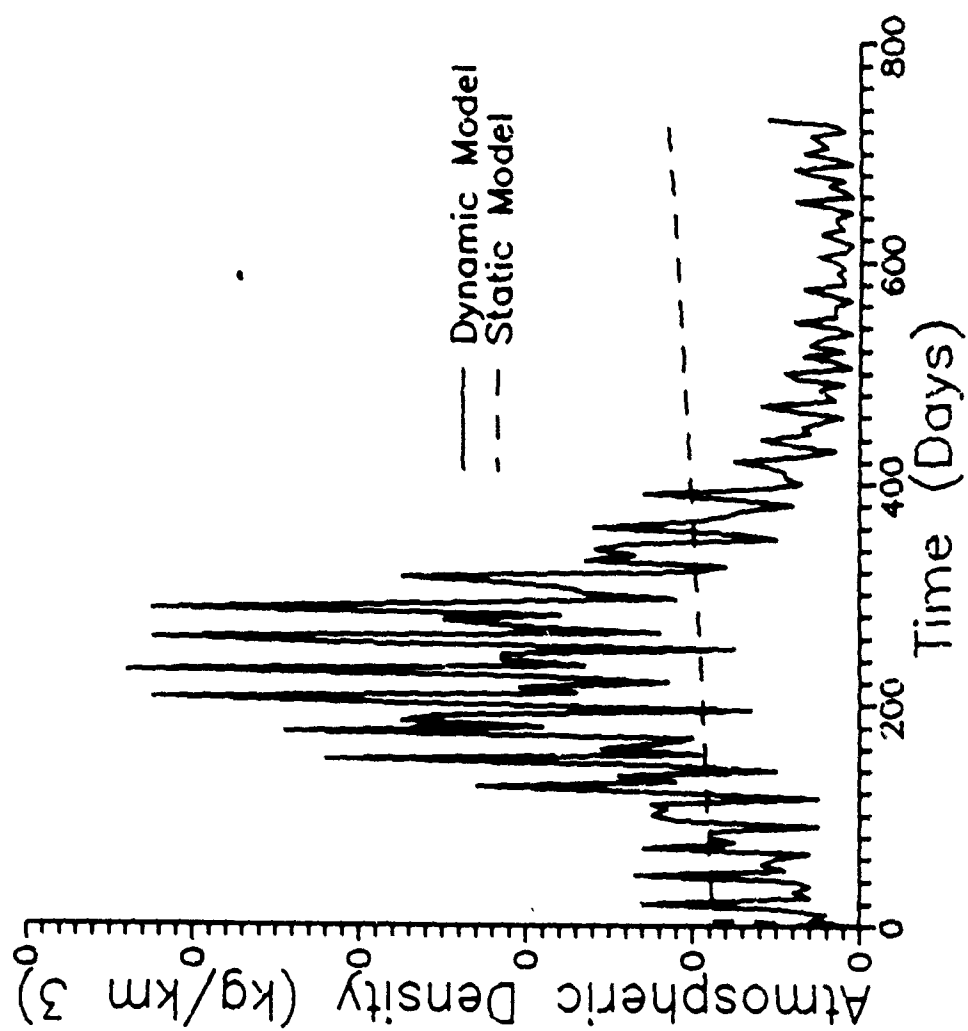Fig. B.47: Eccentricity vs. Time (Case 17)

149
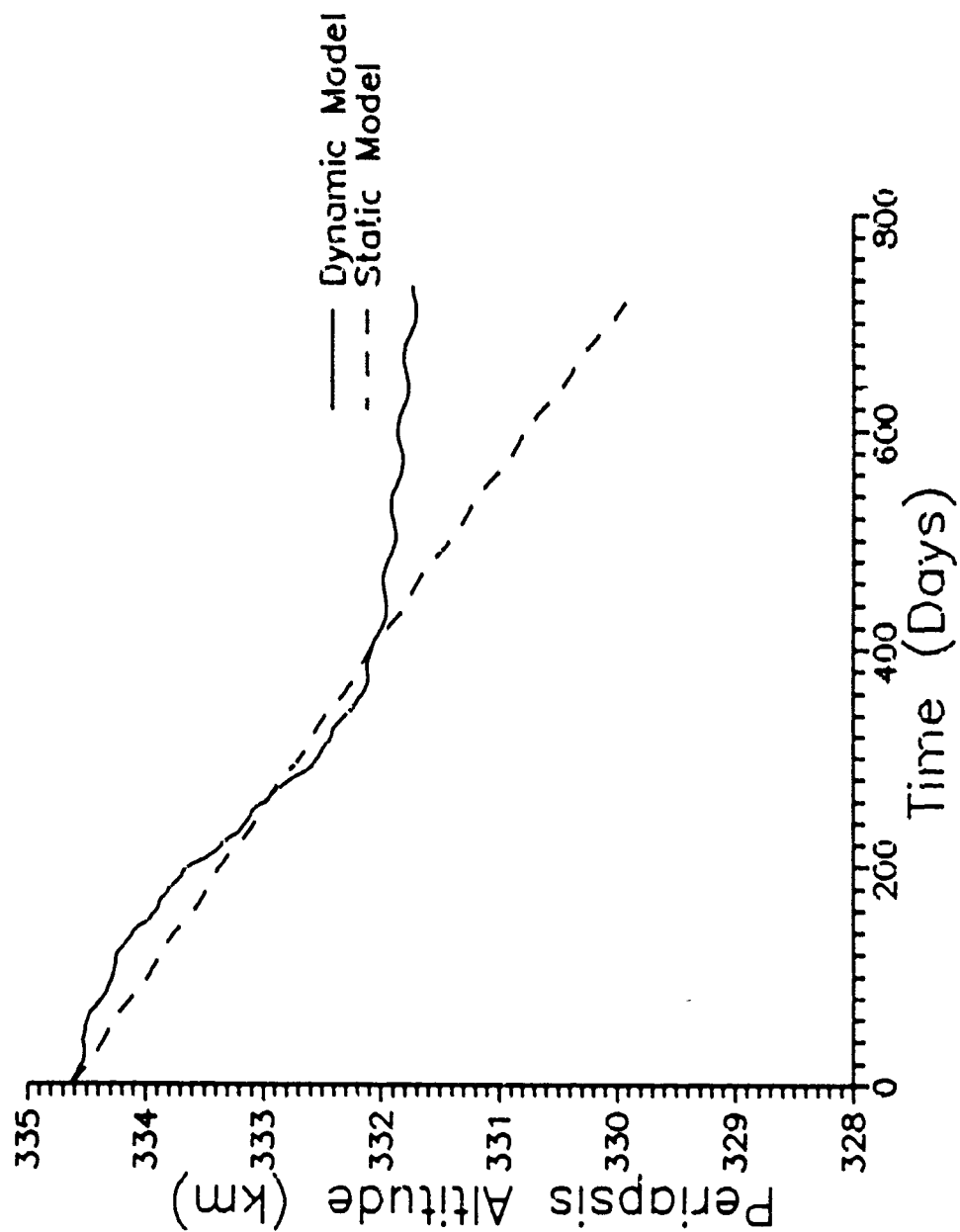
Fig. B.48: Atmospheric Density vs. Time

150

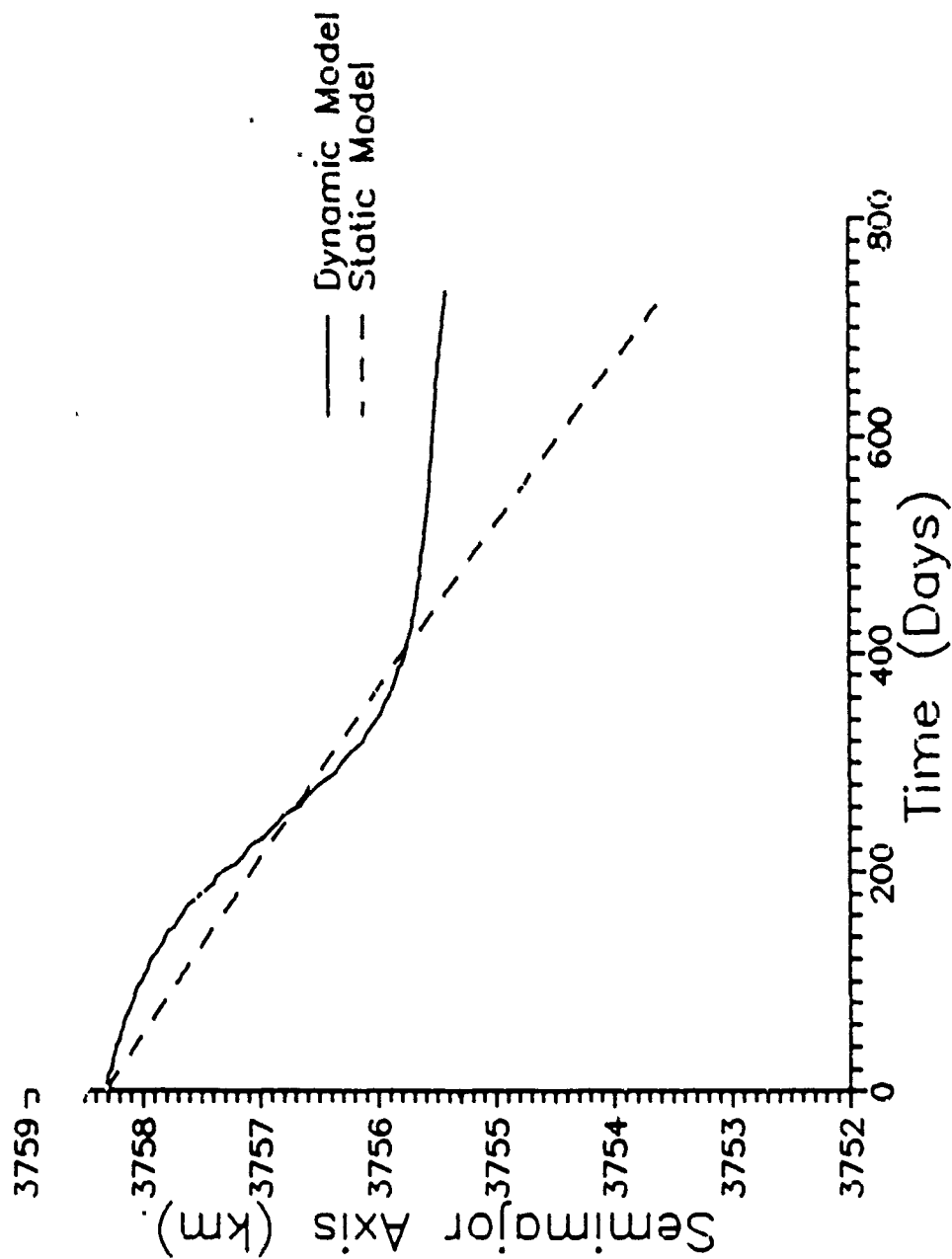Fig. B.49: Periapsis Altitude vs. Time (Check Case)

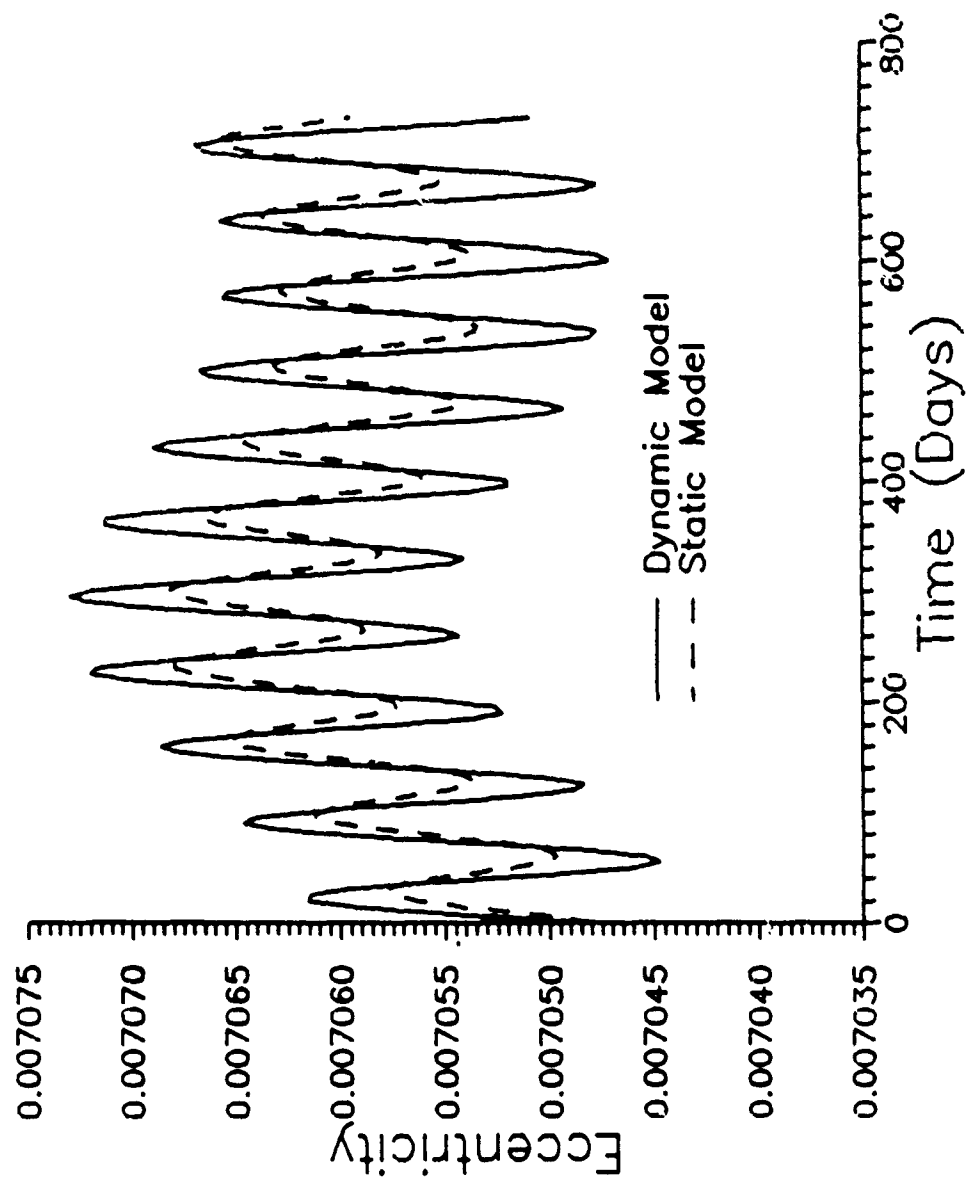Fig. B.50: Semimajor Axis vs. Time (Check Case)

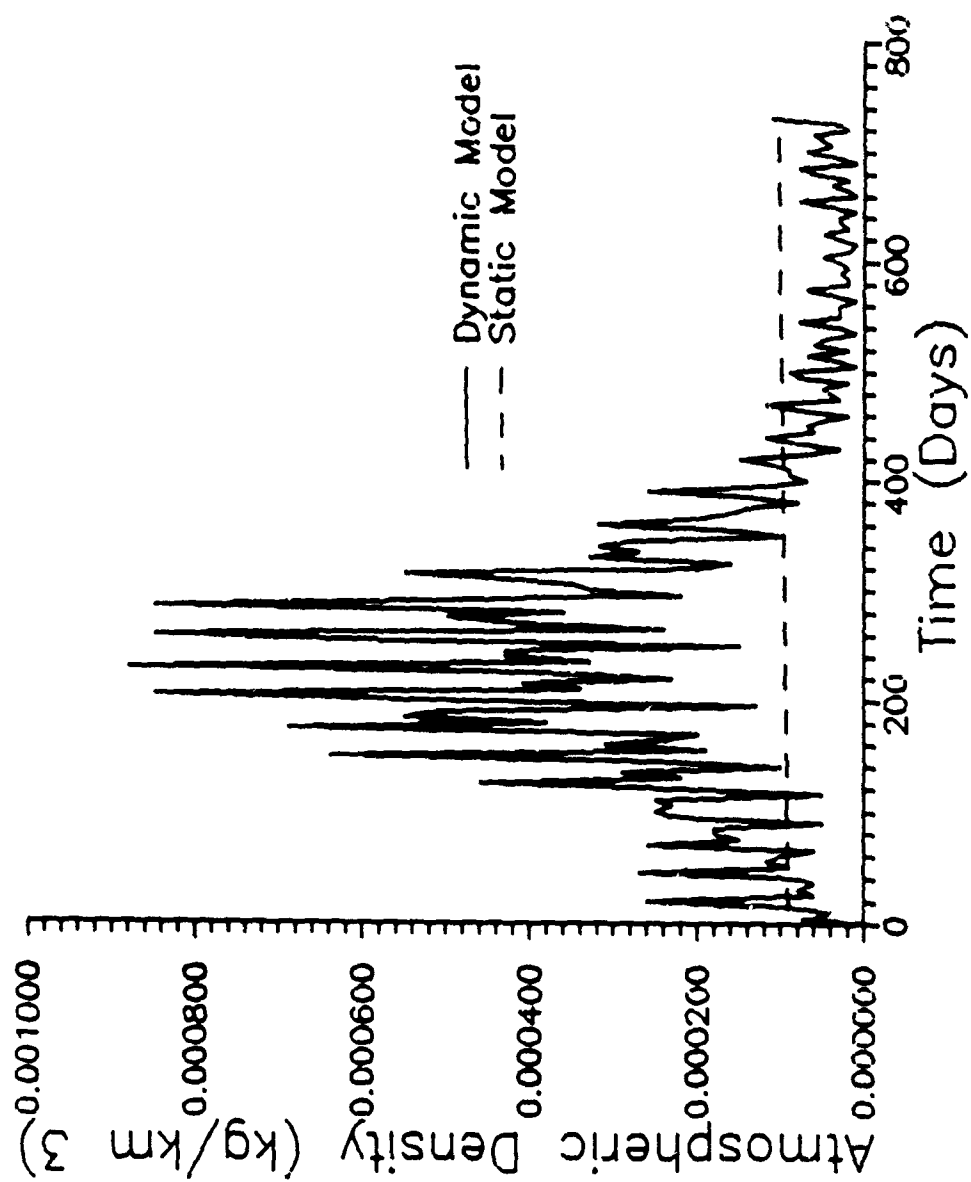152

Fig. B.51 Eccentricity vs. Time (Check Case)

Fig.B.52: Atmospheric Density vs. Time (Check)

Bibliography

1.   Andrews, L. C., *Special Functions for Engineers and Applied Mathematicians*, MacMillan Publishing Company, 1985

2.   Bain, Rodney D., Lecture Material from Advanced Astrodynamics II. School of Engineering, Air Force Institute of Technology (AU). Wright-Patterson AFB, OH, September 1989

3.   Banerdt, W., Saunders, R., Fanale, R., and Salvail, J., "Mars: The Regolith-Atmosphere-Cap System and Climate Change," *Icarus*, Vol. 50, 1982, pp. 381-407

4.   Barth, C., Stewart, A., Hord, C., and Lane, A., "Mariner 9 Ultraviolet Spectrometer Experiment: Mars Airglow Spectroscopy and Variations in Lyman Alpha," *Icarus*, Vol.17, 1972, pp. 457-468

5.   Brandt, J. C., (editor), *The Atmospheres of Mars and Venus*, Gordon and Breach Science Publishers, Inc., 1968

6.   Cain, D.L., Kliore, A.J. Seidel, B.L., Sykes, M.J. and Woiceshyn, P.M., "Approximations to the Mean Surface of Mars and Mars Atmosphere Using Mariner 9 Occultations," *Journal of Geophysical Research*, Vol. 78, 1973, pp. 4352-4354

7.   Conrath, B.J., "Thermal Structure of the Martian Atmosphere during the Dissipation of the Dust Storm of 1971," *Icarus*, Vol. 24, 1975, pp.36-46

8.   Culp, Robert D., Steward, A. Ian, and Chow, Chia-Chuan, "Time Dependent Model of the Martian Atmosphere for Use in Orbit Lifetime and Sustenance Studies," Final Report, JPL Contract 956446, September 30, 1983

9.   ---------, "Long-Lifetime Martian Orbit Selection Using a Time-Dependent Model of the Martian Atmosphere," AIAA/AAS Astrodynamics Conference, August 20-22, 1984

10.   ---------, "Time Dependent Model of the Martian Atmosphere for Use in Orbit Lifetime and Sustenance Studies," *The Journal of the Astronautical Sciences*, Vol. 32, No. 3, July-September 1984

11.   Dudley, Robert L., Jr., Thesis, *Insertion Window Hypersurface For Long Term Orbital Stability Of Artificial*

<u>Satellites About The Planet Venus</u>, School of Engineering,
Air Force Institute of Technology (AU), Wright-Patterson
AFB, OH, 1988

12.   Escobal, P. R., <u>Methods of Orbit Determination</u>, Robert
E. Krieger Publishing Company, 1965

13.   Farmer, C., Davies, D., Holland, A., LaPorte, D., and
Doms, P., "Mars: Water Vapor Observations From the Viking
Orbiters," *Journal of Geophysical Research*, Vol. 82, 1977,
pp. 4225-4248

14.   Fjeldbo, G., Kliore, A.J., and Seidel, B.L., "The
Mariner 1969 Occultation Measurements of the Upper
Atmosphere of Mars," *Radio Science*, Vol.5, 1970, pp. 381-386

15.   Fjeldbo, G., Sweetnam, D., Brenkle, J., Christensen,
E., Farless, D., Mehta, J., Seidel, B., Michael, W., Jr.,
Wallio, A., and Grossi, M., "Viking Radio Occultation
Measurements of the Martian Atmosphere and Topography:
Primary Mission Coverage," *Journal of Geophysical Research*,
Vol. 82, 1977, pp. 4317-4324

16.   Gedeon, G. S., "Tesseral Resonance Effects on Satellite
Orbits," *Celestial Mechanics*, Vol. 1, 1969

17.   Haberle, R., Leovy, C., and Pollack, J., "Some Effects
of Global Dust Storms on the Atmospheric Circulation of
Mars," *Icarus*, Vol. 50, 1982, pp. 322-367

18.   Hanel, R., Conrath, B., Hovis, W., Kunde, V., Lowman,
P., Maguire, W., Pearl, J., Pirraglia, J., Prabhakara, C.,
and Schlachman, B., "Investigation of the Martian
Environment by Infrared Spectroscopy on Mariner 9," *Icarus*,
Vol.17, 1972, pp. 423-442

19.   Hanson, W., Sanatini, S., and Zuccaro, D., "The Martian
Ionosphere as Observed by the Viking Retarding Potential
Analyzers," *Journal of Geophysical Research*, Vol. 82, 1977,
pp. 4351-4362

20.   Kaula, W. M., <u>Theory of Satellite Geodesy</u>, Blaisdell
Publishing Company, 1966

21.   Kellogg, W. W., (editor), <u>The Atmospheres of Mars and
Venus, Publication 944</u>, National Academy of Sciences -
National Research Council, 1961

22.   Kieffer, H., Martin, T., Peterfreund, A., Jakosky, B.,
Miner, E., and Palluconi, F., "Thermal and Albedo Mapping of

Mars During the Viking Primary Mission," *Journal of Geophysical Research*, Vol. 82, 1977, pp. 4249-4290

23.   King-Hele, Desmond, <u>Theory of Satellite Orbits in an Atmosphere</u>, London: Buttersworth, 1964

24.   Kliore, A., (editor), "The Mars Reference Atmosphere," COSPAR, Committee on Space Research, Innsbruck, 1978

25.   ----------, (editor), "The Mars Reference Atmosphere," Advances in Space Research, COSPAR, Vol. 2, No. 2, Pergamon Press, 1982

26.   Kliore, A., Cain, D., Fjeldbo, G., Seidel, B., Sykes, M., and Rasool, S., "The Atmosphere of Mars from Mariner 9 Radio Occultation Measurements, " *Icarus*, Vol.17, 1972, pp. 484-515

27.   Kliore, A.J., Cain, D.L., Levy, G.S., Eshleman, V.R., Fjeldbo, G., and Drake, R.D., "Occultation Experiment: Results of the First Direct Measurement of Mars' Atmosphere and Ionosphere," *Science*, Vol. 149, 1965, pp. 1243-1248

28.   Kwok, J. H., "The Long-Term Orbit Predictor," Jet Propulsion Laboratory, Technical Report No. 86-151, June 1986

29.   Leovy, C., Briggs, G., Young, A., Smith, B., Pollack, J., Shipley, E., and Wildey, R., "The Martian Atmosphere: Mariner 9 Television Experiment Progress Report," *Icarus*, Vol.17, 1972, pp. 373-393

30.   McCuskey, S. W., <u>Introduction to Celestial Mechanics</u>, Addison-Wesley Publishing Company, 1963

31.   McElroy, M., Kong, T., and Yung, Y., "Photochemistry and Evolution of Mars' Atmosphere: A Viking Perspective," *Journal of Geophysical Research*, Vol. 82, 1977, pp.4379-4388

32.   Moroz, V., and Ksanfomaliti, L., "Preliminary Results of Astrophysical Observations of Mars from Mars-3," *Icarus*, Vol.17, 1972, pp. 408-422

33.   Myint-U, Tyn, <u>Partial Differential Equations for Scientists and Engineers</u>, 3rd Ed., Elsevier Science Publishing Co., Inc., 1987

34.   Nier, A., and McElroy, M., "Composition and Structure of Mars' Upper Atmosphere: Results from the Neutral Mass Spectrometer on Viking 1 and 2," *Journal of Geophysical Research*, Vol. 82, 1977, pp. 4341-4350

35.   O'Neil, W., Rudd, R., Farless, R., Hildebrand, C., Mitchell, R., Rourke, K., and Euler, E., *Viking Navigation*, JPL Publication 78-38, November 15, 1979

36.   Owen, T., Biemann, K., Rushneck, D., Biller, J., Howarth, D., and Lafleur, A., "The Composition of the Atmosphere at the Surface of Mars," *Journal of Geophysical Research*, Vol. 82, 1977, pp. 4635-4640

37.   Page, Thornton, (editor), Space Science and Astronomy, MacMillan Publishing Company, Inc., 1976

38.   Pollack, J., and Toon, O., "Quasi-Periodic Climate Changes on Mars: A Rewiew," *Icarus*, Vol. 50, 1982, pp. 259-287

39.   Seiff, A., and Kirk, D., "Structure of the Atmosphere of Mars in Summer at Mid-Latitudes," *Journal of Geophysical Research*, Vol. 82, 1977, pp. 4364-4377

40.   Sheid, F., Numerical Analysis, Schaum's Outline Series, Mcgraw-Hill Book Company, 1988

41.   Snyder, Conway W., "The Missions of the Viking Orbiters," *Journal of Geophysical Research*, Vol. 82, 1977, pp. 3971-3983

42.   Soffen, Gerald A., "The Viking Project," *Journal of Geophysical Research*, Vol. 82, 1977, pp. 3959-3970

43.   Stewart, A., "Mariner 6 and 7 Ultraviolet Spectrometer Experiment: Implications of CO2+, CO, and O Airglow," *Journal of Geophysical Research*, Vol. 77, 1972, pp. 54-68

44.   Stewart, A., Barth, C., Hord, C., and Lane, A., "Mariner 9 Ultraviolet Spectrometer Experiment: Structure of Mars' Upper Atmosphere," *Icarus*, Vol.17, 1972, pp.469-474

45.   Stuart, J.R., "Low-cost, Focused-Science Mars Mission," AIAA Paper No. 83-0519, AIAA 21st Aerospace Sciences Meeting, Reno, Nevada, January, 1983

46.   Uphoff, C. W., "Orbit Selection for a Mars Geoscience/Climatology Orbiter," AIAA Paper No. 84-0318, AIAA 22nd Aerospace Sciences Meeting, Reno, Nevada, 1984

47.   Vinh, N., Busemann, A., and Culp, R., Hypersonic and Planetary Entry Flight Mechanics, University of Michigan Press, Ann Arbor, 1980

48. Wiesel, William E., Lecture Material from Advanced
Astrodynamics. School of Engineering, Air Force Institute
of Techmology (AU). Wright-Patterson AFB, OH, February 1989

49. Zurek, Richard W., "Martian Great Dust Storms," *Icarus*,
Vol. 50, 1982, pp. 288-310

<u>Vita</u>

Captain Zoltan L. Farago

In 1979 he graduated from Lake Shore High School and began attending Oakland University. He graduated Summa Cum Laude from Oakland University in 1983, earning a B.S. degree in Physics. Following graduation, he attended Officer Training School and accepted a commission in the United States Air Force. His first assignment was to attend Parks College of St. Louis University under the Undergraduate Engineering Conversion Degree Program in order to earn a B.S. in Aerospace Engineering. He graduated Summa Cum Laude in 1985. His next assignment was with the 6595th Shuttle Test Group of the Western Space and Missile Center (WSMC) at Vandenberg AFB, California, where he worked to prepare the Shuttle satellite processing facilities for the launch of Shuttle payloads. While at Vandenberg AFB, he was selected to attend Squadron Officer School, from which he graduated in December, 1987. He stayed at WSMC until selected to attend the School of Engineering, Air Force Institute of Technology, starting in June, 1988.

REPORT DOCUMENTATION PAGE

Form Approved
OMB No. 0704-0188

1a. REPORT SECURITY CLASSIFICATION UNCLASSIFIED	1b. RESTRICTIVE MARKINGS
2a. SECURITY CLASSIFICATION AUTHORITY	3. DISTRIBUTION/AVAILABILITY OF REPORT Approved for Public Release distribution unlimited
2b. DECLASSIFICATION/DOWNGRADING SCHEDULE	

4. PERFORMING ORGANIZATION REPORT NUMBER(S) AFIT/GA/ENY/89D-01	5. MONITORING ORGANIZATION REPORT NUMBER(S)

6a. NAME OF PERFORMING ORGANIZATION School of Engineering	6b. OFFICE SYMBOL (If applicable) AFIT/ENY	7a. NAME OF MONITORING ORGANIZATION

6c. ADDRESS (City, State, and ZIP Code) Air Force Institute of Technology (AU) Wright-Patterson AFB, OH 45433-6583	7b. ADDRESS (City, State, and ZIP Code)

8a. NAME OF FUNDING/SPONSORING ORGANIZATION	8b. OFFICE SYMBOL (If applicable)	9. PROCUREMENT INSTRUMENT IDENTIFICATION NUMBER

8c. ADDRESS (City, State, and ZIP Code)	10. SOURCE OF FUNDING NUMBERS

PROGRAM ELEMENT NO.	PROJECT NO.	TASK NO	WORK UNIT ACCESSION NO.

11. TITLE (Include Security Classification)
See Box 19

12. PERSONAL AUTHOR(S)
Zoltan L. Farago, B.S., B.S.A.E., Captain, USAF

13a. TYPE OF REPORT MS Thesis	13b. TIME COVERED FROM _____ TO _____	14. DATE OF REPORT (Year, Month, Day) 1989 December	15. PAGE COUNT 175

16. SUPPLEMENTARY NOTATION

17. COSATI CODES			18. SUBJECT TERMS (Continue on reverse if necessary and identify by block number)
FIELD	GROUP	SUB-GROUP	Dynamic Martian Atmosphere, Orbital Perturbations, Long Term Orbits, Mars
22	03		
04	01		

19. ABSTRACT (Continue on reverse if necessary and identify by block number)

Title: An Investigation of Long Term Orbits
About the Planet Mars Using a Dynamic
Atmosphere Model

Thesis Chairman: Rodney D. Bain, Capt, USAF
Instructor of Astronautical Engineering

20. DISTRIBUTION/AVAILABILITY OF ABSTRACT ☒ UNCLASSIFIED/UNLIMITED ☐ SAME AS RPT. ☐ DTIC USERS	21. ABSTRACT SECURITY CLASSIFICATION Unclassified	
22a. NAME OF RESPONSIBLE INDIVIDUAL Rodney D. Bain, Captian, USAF	22b. TELEPHONE (Include Area Code) (513) 255-3633	22c. OFFICE SYMBOL AFIT/ENY

DD Form 1473, JUN 86 · Previous editions are obsolete. · SECURITY CLASSIFICATION OF THIS PAGE

Unclassified

Abstract

Block 19:

This study examines the effects of atmospheric drag on the long term orbital motion of an artificial satellite about the planet Mars using a dynamic Martian atmosphere model instead of a static atmosphere model.

Present studies of motion through the Martian atmosphere use a non-rotating (static) atmosphere model which has a simple exponential drop-off with altitude. However, Mars, like other planets, is known to have a turbulent, complex atmosphere. As a result, a new dynamic model of the Martian atmosphere uses data from recent space probes of Mars to simulate an atmosphere that is both position dependent, through latitude and longitude effects, and time dependent, through a variety of effects. These include diurnal and seasonal effects, annual motion effects, solar activity effects, and dust storm effects. Nine constituent gases are included in the above model. The model determines atmospheric mass density for the calculation of atmospheric drag. The existing static model is also used to calculate atmospheric drag to provide a comparison in conjunction with other effects.

In addition to atmospheric drag, perturbations due to the attraction of the sun, the aspherical gravity field of Mars, and the effects of the solar wind are also modeled.

The resulting orbital data are then compared to determine the differences between the two models, thus showing the effects on long term motion of using a dynamic model of the Martian atmosphere. *Thesis. (SDW)*